気象庁欧文海洋報告

第19巻 第2号

THE OCEANOGRAPHICAL MAGAZINE

Vol. 19 No. 2

LIBRARY
JUN 12 1968
FISH & WILDLIFE SERVICE

CONTENTS

J. MASUZAWA: An oceanographic section from Japan to New Guinea at 137°E in January 1967 95
T. UENO: Numerical experiments of the wind-driven circulation in the Pacific Ocean 119
H. AKAMATSU and T. SAWARA: Cruise report of CSK survey by JMA in 1966 156
M. MIYAZAKI, S. KURONUMA, T. INOUE and K. MADOKORO: Tidal constant along the coast of Japan (Part II) 163
H. YOSHIMURA: The gross β-radioactivity of fallout collected at the southern weather station located in 29°N and 135°E 169
K. HISHIDA: The Ito marine observation tower 173
M. YASUI, T. YASUOKA, K. TANIOKA and O. SHIOTA: Oceanographic studies of the Japan Sea (1)—Water characteristics— 177
M. YASUI and T. KISHII: Lowering of heat flow probes in the horizontal attitude 193
K. NAGASAKA: Handy charger for oceanographic instrument 197
S. MORIYASU: On the anomaly of the sea surface temperature in the East China Sea (I) 201
M. YASUI, Y. HASHIMOTO and S. UYEDA: Geomagnetic studies of the Japan Sea (1)—Anomaly pattern on the Japan Sea— 221

Published by the Japan Meteorological Agency

December, 1967

The Oceanographical Magazine
Vol. 19, No. 2, December 1967

An Oceanographic Section from Japan to New Guinea at 137°E in January 1967

By

Jotaro MASUZAWA

Japan Meteorological Agency

(Received November 16, 1967)

Abstract: A long meridional oceanographic section was made at 137°E from Japan to New Guinea in January 1967 on board the R/V *Ryofu Maru* for the CSK. The section involved the Kuroshio, its countercurrent, weak currents in the subtropics, the North Equatorial Current, the Equatorial Countercurrent, and the Equatorial Undercurrent. The descriptive features of these currents, such as width, geopotential difference, geostrophic flux and water characteristics are demonstrated. The salinity minimum in and south of the southern part of the North Equatorial Current is different in thermosteric anomaly from the salinity minimum in and north of the northern part of the North Equatorial Current, so that the former minimum may not be a direct southward extension of the latter minimum. Waters of the Equatorial Countercurrent and Undercurrent consist of medium-sized water masses both from the North Equatorial Current and from the South Pacific.

1. *Introduction*

A number of meridional hydrographic sections were made in the western North Pacific Ocean by Japanese Hydrographic Office in 1933 to 1942. After World War II similar sections were taken by various agencies and institutes of Japan for international expeditions such as the Equapac in 1956, the IGY (International Geophysical Year) in 1957 to 1958, and the CSK (Cooperative Study of the Kuroshio) since 1965. Unfortunately, however, it seems difficult to find any satisfactory sections from Japan to New Guinea covering all the major currents of the western North Pacific.

During the IGY, on the other hand, the Russian Vessel *Vityaz* made two long meridional sections from the north of the Kuroshio to the south of the equator; one at 154°E in July 1957 and the other at 142°E in March to April 1958 (BOGOROV *et al.*, 1960).

A long meridional oceanographic section at 137°E was taken in January 1967 on board the R/V *Ryofu Maru*, Japan Meteorological Agency (Fig. 1) as part of the

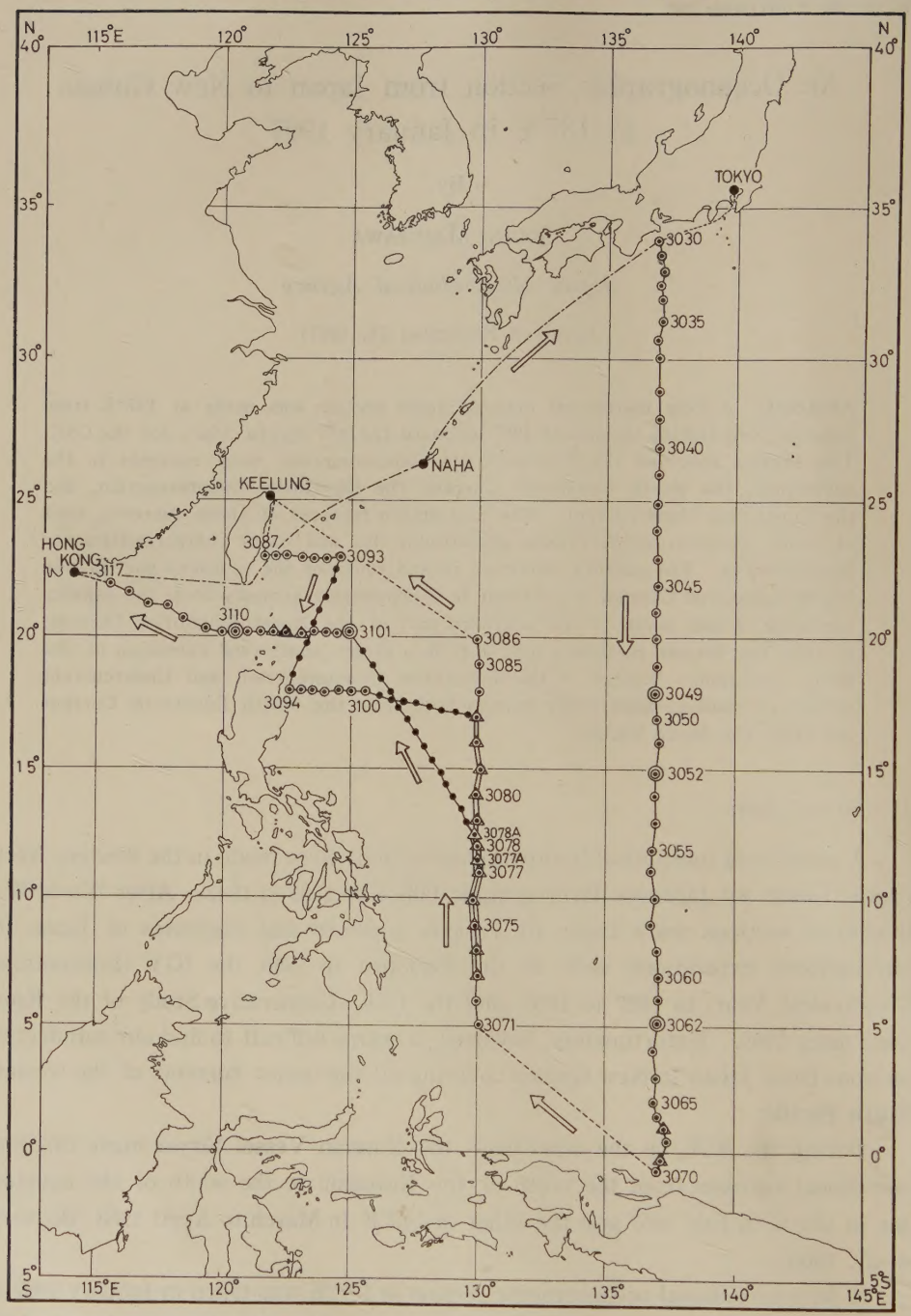

Fig. 1. Track chart of the CSK cruise of the R/V *Ryofu Maru*, JMA in January to March 1967.

CSK (MASUZAWA, 1967). The choice of the meridian at 137°E was made to observe distributions of currents and waters, as undisturbed by islands and submarine mountains as possible, and to include the Kuroshio, the North Equatorial Current, and the Equatorial Countercurrent and Undercurrent in the western Pacific Ocean. The observation on the section at 137°E was started at 34°N (Ry 3030) near the coast of Japan on 12 January, 1967 and terminated at 0°45'S (Ry 3070) just north of New Guinea on 24 January.

The section consists of 41 serial stations, which were spaced 60 miles apart, though 30 miles both north of 32°N and south of 2°N. The sampling depths were chosen every 25 m from the sea surface to 200 m, every 50 m from 200 m to 400 m, every 100 m from 400 m to 1,000 m and every 200 m from 1,000 m to 1,600 m, respectively. Neither the station spacing nor the sampling depth were satisfactorily appropriate, though better than the so-called standard method used commonly in the western Pacific. Besides, neither in-situ salinometers nor salinity-temperature-depth recorders (STD) were available for the cruise.

Direct current measurements were made from the drifting ship at three stations near the equator, Ry 6067, 6069 and 6070, with two Roberts-type currentmeters, one of them being placed at a depth of about 800 m to estimate ship drift. Velocities measured by the other currentmeter in the upper 300 m or 400 m are corrected for the ship drift thus estimated (Fig. 4). The depth of a currentmeter was determined either by the thermometric method or by wire angle.

2. *Procedures*

A temperature-salinity diagram with a group of lines of uniform thermosteric anomaly on it[1] (MONTGOMERY & WOOSTER, 1954) was used to make a stationgraph for each station. Curves of depth, salinity and oxygen content were drawn against temperature as common abscissa (MONTGOMERY, 1954). Isolines of temperature, salinity, oxygen content, and thermosteric anomaly on the vertical section (Fig. 2) were drawn with use of both observed values and depths of isolines read from each station curve.

The hydrostatic or geostrophic computation was done relative to the 1,000 db surface, which has been commonly adopted as a reference surface in the North Pacific. The distribution of zonal geostrophic currents throgh the section is represented by geopotential anomaly on isobaric surfaces (Fig. 3).

1) The thermosteric anomaly is the specific-volume anomaly without the pressure-dependent terms; the symbol used for thermosteric anomaly commonly is δ_T and the unit chosen is centiliters per ton (cl/t).

Another method was tried to represent the distribution of water characteristics in the equatorial current system (Figs. 5, 6 & 7). The isopleths of salinity and oxygen content in the equatorial current system south of 22°N were drawn against thermosteric anomaly in logarithmic scale instead of geometric depth used commonly. These two figures (Figs. 7 a & b), together with a meridional distribution of acceleration potential[2] (MONTGOMERY & SPILHAUS, 1941) on isanosteric surfaces[3] (MONTGOMERY & WOOSTER, 1954) (Fig. 6), may serve well for showing a complicated distribution of water characteristics with respect to thermosteric anomaly in the equatorial current system.

3. Gross hydrographic features

3-1 Temperature (Fig. 2 a)

The main thermocline, centered at 10°C to 12°C north of 15°N, slopes down rapidly from the northern edge (Ry 3031) of the Kuroshio to the southern edge (Ry 3035), where the nearly isothermal surface-mixed layer is the thickest over the section. The thermocline becomes gradually shallow southward from 30°N to 15°N, and in the vicinity of 15°N the center of the thermocline is switched from 11°C to 20°C or so. At the boundary between the North Equatorial Current and the Equatorial Countercurrent, the center is most shallow, and the vertical gradient of temperature in the thermocline is the largest over the section.

In the lowest part of, or below the thermocline, below 7°C, the lateral minimum of temperature on a level surface is not found at the southern limit of the North Equatorial Current, but seems to occur in the region of 25°N to 15°N. The significance of this fact is not clear.

3-2 Salinity (Fig. 2 b)

The North Pacific tropical saline water, with salinity exceeding 35‰ and with thermosteric anomaly as much as 350 to 450 cl/t (Fig. 7 b), lies in the upper part of the thermocline between 10°N and 20°N. The saline water seems to be

2) The numerical computation of acceleration potential is expressed as follows,

$$\int_{\delta_0}^{\delta} p d\delta + p_0\delta_0 \text{, or } -\int_{p_0}^{p} \delta dp + p\delta$$

where p is pressure, δ is specific-volume anomaly, and p_0 and δ_0 are the values at the reference surface. The specifie-volume anomaly is replaced by thermosteric anomaly.

3) The isanosteric surface denotes the surface of uniform specific-volume or thermosteric anomaly.

in contact with the sea surface near 19°N. The other saline water, originating in the South Pacific, extends as far north as 6°N, near the northern limit of the Equatorial Countercurrent.

The North Pacific major salinity minimum, the core of which is approximately on the isanosteric surface of 125 cl/t, can be traced from the coast of Japan as far south as 15°N. Near 15°N, the core of the salinity minimum jumps from 125 cl/t up to 175 cl/t. The minimum extends beyond the southern limit of the North Equatorial Current as far south as 3°N, where the minimum disappears abruptly.

The deep salinity minimum centered at 80 cl/t can be detected as far north as 13°N, the salinity being between 34.50‰ and 34.55‰. Double salinity minima are revealed in the range between 13°N and 3°N at the present section. The deep salinity-minimum water may originate in the South Pacific Intermediate Water (ROCHFORD, 1960; REID, 1965).

The saline structure in the upper 300 m south of 5°N is remarkably complicated.

3-3 Thermosteric anomaly (Fig. 2 c)

The gross features of the thermosteric-anomaly section are similar to those of the temperature section. It my be noteworthy that isanosteres below 100 cl/t are roughly horizontal in the equatorial currents south of 14°N, though there are irregular disturbances. It follows that the vertical shear of geostrophic velocity in lower layers, below 600 m, is nearly zero south of 14°N.

3-4 Oxygen content (Fig. 2 d)

An outstanding oxygen minimum with the minimum content less than 1.5 m*l*/*l* is revealed below the thermocline from the coast of Japan all the way southward to 3°N. The core of the minimum changes in depth at the vicinity of 15°N, and there the value of thermosteric anomaly at the core also changes from 80 cl/t in the north to 125 cl/t in the south. A faint minimum of oxygen content is present in deeper layers between 60 cl/t and 90 cl/t south of 13°N, so that there are double minima of oxygen content in the range between 13°N and 3°N as well as salinity.

4. Current structure

The limits of zonal currents through the section can be easily determined by

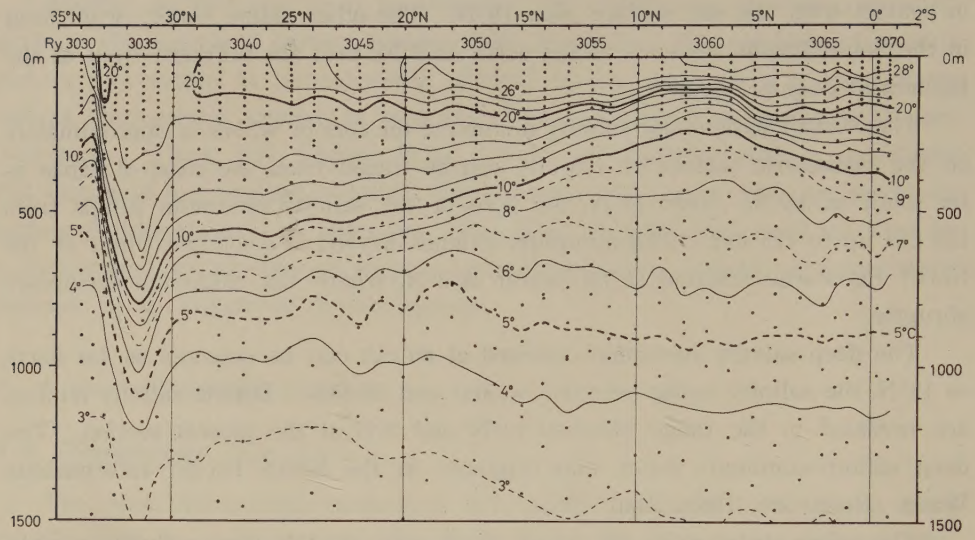

(a)

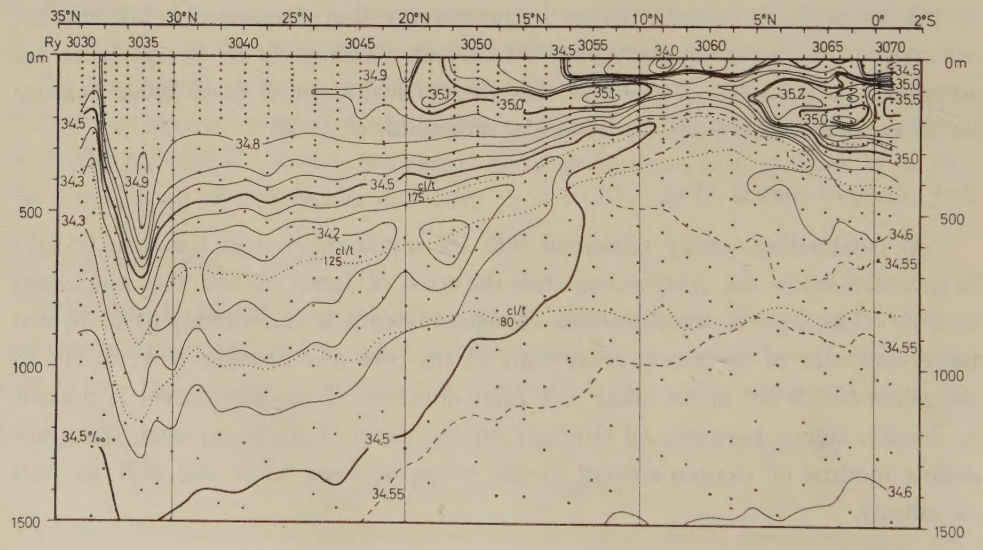

(b)

Fig. 2. Vertical sections of temperature (a), salinity (b), thermosteric anomaly (c) and oxygen content (d) at 137°E in January 1967, vertical exaggeration, 1480.

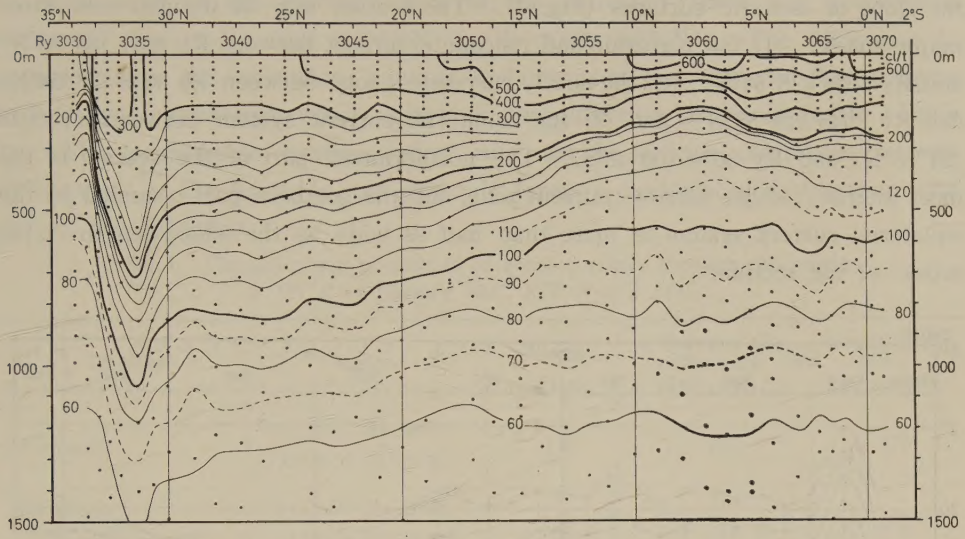
35°N
30°N
25°N
20°N
15°N
10°N
5°N
0°N
2°S
Ry 3030
3035
3040
3045
3050
3055
3060
3065
3070
0m
500
1000
1500
cl/t
600
500
400
300
200
120
110
100
90
80
70
60

(c)

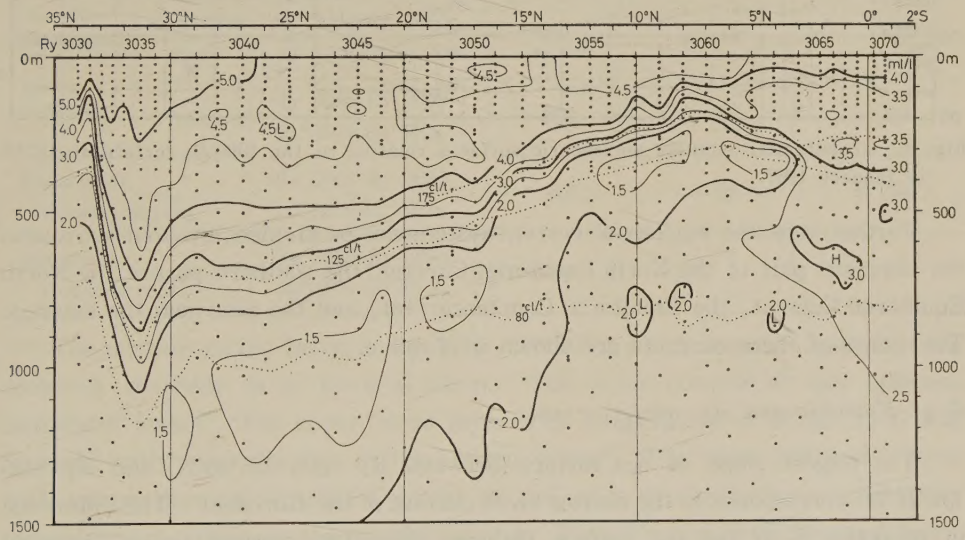
35°N
30°N
25°N
20°N
15°N
10°N
5°N
0°
2°S
Ry 3030
3035
3040
3045
3050
3055
3060
3065
3070
0m
500
1000
1500
ml/l
4.0
3.5
3.0
2.5
2.0
1.5
4.5
5.0
4.5L
cl/t
175
125
80
H
L

(d)

the slope of isobaric surfaces (Fig. 3). The section may be divided into three major zones: (1) the Kuroshio and its countercurrent between Ry 3031 (33°28′N) and Ry 3038 (28°54′N); (2) the nearly currentless zone between Ry 3038 (28°54′N) and Ry 3045 (21°58′N); and (3) the equatorial current system between Ry 3045 (21°58′N) and Ry 3070 (00°43′S). The northernmost part of the section is the most intense, though narrow, current zone, and the southern part occupied by the equatorial current system is more than half as wide as the whole length (2,100 miles) of the section.

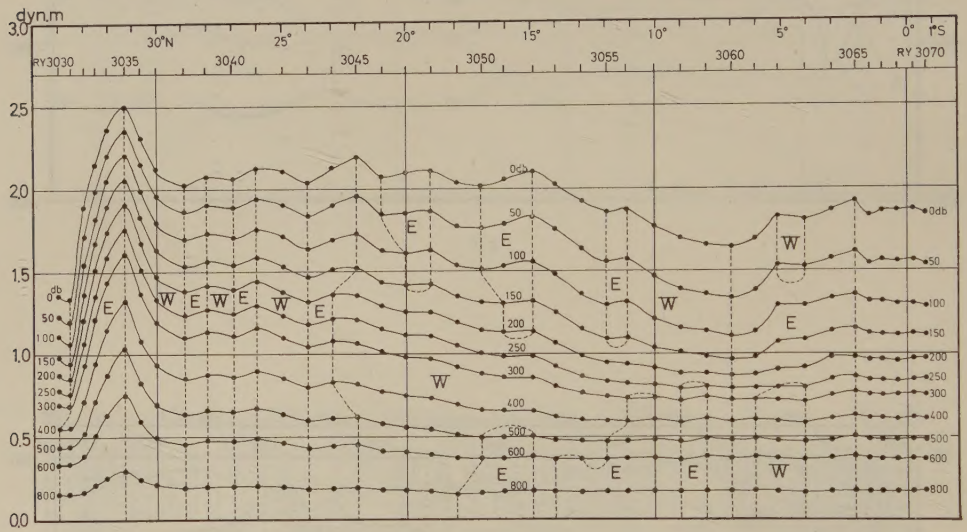

Fig. 3. Geopotential anomaly on isobaric surfaces relative to the 1000 db surface at 137°E in January 1967.

Furthermore, the equatorial current system can be divided into four subzones: the northern part of the North Equatorial Current; the southern part of the North Equatorial Current; the Equatorial Countercurrent; and the zone near the equator. The limits of these currents are shown in Table 1.

4-1 Kuroshio and its countercurrent

The largest slope of sea surface between Ry 3031 (33°28′N) and Ry 3035 (31°18′N) corresponds to the narrow swift current of the Kuroshio. The difference in geopotential at the sea surface between these two stations is 1.17 dynamic meters, which is rather larger than the values estimated usually (e. g., MASUZAWA, 1965).

Just south of the eastward flow of the Kuroshio, there is a well-defined westward flow at Ry 3035 (31°18′N) to Ry 3038 (28°54′N). The difference in geopotential at the sea surface between both limits of the westward flow amounts to 0.47 dynamic meters, which is 40% of the difference in the Kuroshio (Table 1). This remarkable westward flow may not be a long continuous current independent of the Kuroshio, but probably forms a clockwise eddy together with part of the Kuroshio.

Table 1. Characteristic properties of zonal currents through the section at 137°E in January 1967, R/V *Ryofu Maru*.

Current		Range	Width (mile)	Difference of sea surface (dyn. cm)	Geostrophic flux ($km^3 \cdot hr^{-1}$)
Kuroshio		Ry 3031–Ry 3035 33°30′N–31°20′N	130	− 117	+ 273
Kuroshio Countercurrent		Ry 3035–Ry 3038 31°20′N–28°54′N	146	+ 47	− 162
Subtropics		Ry 3038–Ry 3045 28°54′N–21°58′N	416	− 16	+ 0.3
North Equatorial Current	Northern part	Ry 3045–Ry 3052 21°58′N–14°54′N	424	+ 10	− 79
	Southern part	Ry 3052–Ry 3060 14°54′N–06°58′N	476	+ 45	− 145
	Whole	Ry 3045–Ry 3060 21°58′N–06°58′N	900	+ 55	− 224
Equatorial Countercurrent		Ry 3060–Ry 3065 06°58′N–02°04′N	294	− 28	+ 234
Equatorial Undercurrent?		Ry 3065–Ry 3070 02°04′N–00°43′S	167	...	...

The surface mixed layer at Ry 3035 (31°18′N), which may be located at the center of the eddy, is as thick as 550 m. The layer consists of two different isothermal layers. The upper 300 m layer with temperature of 18.5± 0.1°C was formed locally by convection in the present winter. The lower isothermal layer with temperature of 17.9±0.1°C might be the relics of the surface mixed layer formed by convection in the previous winter. However, the surface mixed layer, which is much thicker than usual, may be associated not only with winter convection but also with sinking motion due to horizontal convergence.

4-2 Subtropical currents

To the south of the Kuroshio countercurrent, there is a weak-current or currentless zone between Ry 3038 (28°54′N) and Ry 3045 (21°58′N). The sea surface is roughly flat over the zone, though there are small local or temporary irregularities and weak eastward and westward currents appear alternately (Fig. 3). It can be noted in Fig. 3 that the eastward flow at 22°N to 24°N is the most pronounced current in the upper 100 m. This current may be an eastward current which is frequently observed near the latitudes (Uda, 1955; Yamanaka *et al.*, 1965) and which is designated the "Subtropical Countercurrent" by Yoshida & Kidokoro (1967). The temperature-salinity relations and temperature-oxygen relations, however, are nearly uniform within the zone. Both the salinity minimum and the oxygen minimum in this zone are best-defined over the whole length of the section.

4-3 North Equatorial Current

In contrast to the well-defined southern limit of the North Equatorial Current at Ry 3060 (06°58′N), the northern limit cannot be easily defined geostrophically (Fig. 3). The southward downslope of sea surface, which indicates the westward geostrophic current, is clearly revealed between Ry 3052 (14°54′N) and Ry 3060 (06°58′N). In subsurface depths, however, isobaric surfaces generally slope down southward from Ry 3045 (21°58′N) to Ry 3060 (06°58′N). The North Equatorial Current, therefore, may be divided into two parts: The northern half between Ry 3045 (21°58′N) and Ry 3052 (14°54′N) and the southern half between Ry 3052 (14°54′N) and Ry 3060 (06°58′N).

In the northern half of the North Equatorial Current, the meridional gradient of thermosteric anomaly in the upper 200 m is opposite to that in lower layers below 300 m (Fig. 2 c). Thus, the westward geostrophic velocity is the highest in depths of 200 m to 300 m (Fig. 3). It is noted that geostrophic currents at 17°N to 15°N are eastward both in the upper 200 m and in lower layers below 500 m or so (Fig. 3). The lower eastward currents could be indentical with the eastward flow near the latitudes on the isanosteric surface of 80 cl/t, which was calculated geostrophically referred to the 2,000 db surface by Reid (1965).

In the southern half of the North Equatorial Current, on the other hand, the recognizable westward current is limited to the upper 500 m, and geostrophic currents in lower layers are nearly zero or rather eastward, though unreliable (Fig. 3). A weak eastward current is present in upper layers at 12°N to 11°N.

Similar eastward currents are found on the section at 130°E made on the present cruise (Fig. 1) not only from geostrophic computation but also from direct current measurements.

The core of the North Equatorial Current seems to be in shallower layers in the south and to be in deeper layers in the north.

4-4 Equatorial Countercurrent and Undercurrent

The range of the Equatorial Countercurrent can be easily determined geostrophically between Ry 3060 (06°58′N) and Ry 3065 (02°04′N). The latitudinal location of the Equatorial Countercurrent in the present section is almost the same as summarized statistically in the western equatorial Pacific (Tsuchiya, 1961; Yamanaka *et al.*, 1965). The difference in geopotential at the sea surface between the northern limit and the southern limit of the Countercurrent is 0.28 dynamic meters (Table 1).

The current is separated into two zones by the weaker flow at 4°N to 5°N (Fig. 3). The flow may be just a local or temporary phenomenon, but similar features have been pointed out in the Equatorial Countercurrent of the western Pacific (Yosida *et al.*, 1959; Takahashi, 1959; Yamanaka *et al.*, 1965). Isanosteric surfaces of 110 cl/t to 60 cl/t at 4°N to 2°N noticeably slope down rather steeply southward (Fig. 2 c). Similar conditions have been shown in the central equatorial Pacific by Montgomery & Stroup (1962).

It has been generally accepted that the current field near the equator, including the Equatorial Undercurrent, can be well represented by geostrophic approximation (Montgomery, 1962). Near the equator at 137°E in January 1967, however, the hydrostatic computation relative to the 1,000 db surface (Fig. 3) does not reveal a well-established geostrophic current field. Nevertheless, direct current measurements near the equator show a fairly consistent current pattern (Fig. 4). At 1°N, swift eastward currents were observed in the upper 400 m, when referred to 950 m depth; the maximum speed was as large as 3 knots at depths of 200 m to 300 m. Similar current maxima are shown at the same depths in the western Equatorial Undercurrent both by geostrophic computation (Tsuchiya, 1961) and by direct current measurements on board the *Vityaz* in 1966 (Kort *et al.*, 1966). At the equator, eastward to northeastward currents were observed in the upper 200 m, though the speeds were mostly less than 1 knot. At the southernmost station (Ry 3070) near the coast of New Guinea, the zonal components of velocity were more frequently westward.

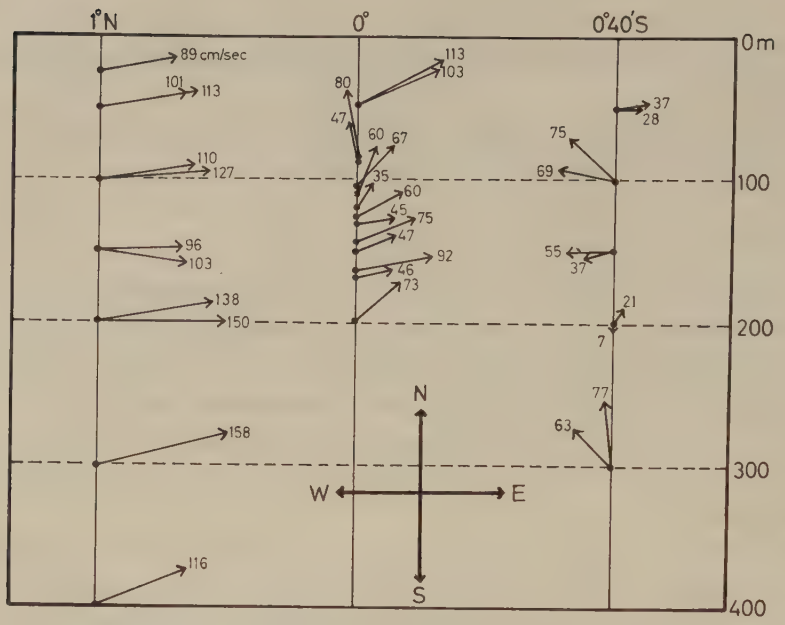

Fig. 4. Vertical distributions of current vectors observed by Roberts-type currentmeters at 1°N, 0°, and 0° 40′S on the meridian of 137°E in January 1967. The current vector is represented relative to the current at the depth of 950 m at 1°N, 700 m at 0°, and 800 m at 0°40′S, respectively.

These currents observed near the equator are not in good geostrophic balance. The terms of enertia and friction might be important in balance of forces, because the coast of New Guinea is close to the equator at the section.

As already reported often in the western Pacific (Yosida *et al.*, 1959; Takahashi *et al.*, 1960; Tsuchiya, 1961; Montgomery, 1962, etc.), the Equatorial Countercurrent centered in the surface layer at 4°N or 5°N is not clearly separated from the Equatorial Undercurrent, the core of which lies in a subsurface depth, 200 m to 300 m, near the equator. These two cores are usually connected by a sloping layer of eastward flow. In the present case, it seems that the strong eastward flow at 1°N is of the character of the Undercurrent, which might be overlaped by the "New Guinea Coastal Current" (Wyrtki, 1961). The latter current has been imagined to be a eastward current close to the coast of New Guinea in winter of the northern hemisphere and to be replaced by westward flows of the South Equatorial Current in other seasons (Wyrtki, 1961; Burkov & Ovchinnikov, 1960). Even though it is true, the Equatorial Undercurrent is not a current isolated from the Equatorial Countercurrent, though the former current

is separated from the latter current in the central or eastern equatorial Pacific.

5. *Water characteristics*

5-1 *Upper waters of the North Equatorial Current*

The North Pacific tropical saline water with the core at about 400 cl/t (CANNON, 1966) does not show the salinity more than 35.15‰ in the present section (Fig. 7 a). The oxygen content in the saline water is rather lower than above and below the saline water (Fig. 7 b).

The weak oxygen maximum with the core at 240 cl/t can be seen at depths of 250 m to 350 m in the northern half of the North Equatorial Current (Figs. 2 d, 7 b). The temperature and salinity at the core are 16°C and 34.7‰, respectively (see Ry 3050 in Fig. 9). The water forming the oxygen maximum seems to come from the colder part of the North Pacific "Subtropical Mode Water" (MASUZAWA, to be published), which is the counterpart of the "18°C water" in the North Atlantic (WORTHINGTON, 1959).

5-2 *Upper waters of the Equatorial Countercurrent and Undercurrent*

The thermocline at the northern limit of the Equatorial Countercurrent, 7°N, is the thinnest, the average vertical gradient of temperature is 0.12° C/m between 28°C (40 m) and 11°C (190 m) (Fig. 8). The thermocline splits in the Equatorial Countercurrent region. At 4°N, for example, isotherms for 26°C to 28°C make ridges and isotherms for 19°C to 22°C make troughs, so that there is a vertical spreading of the upper half of the thermocline. The water in the vertical spreading represents an isolated core of high salinity (the maximum value 35.3‰). That the water comes from the South Pacific tropical saline water appearing at Ry 3070 can be inferred from the T-O_2 curve at Ry 3063 (Fig. 9).

There is another vertical spreading of the thermocline at 200 m between 3°N and the equator. The spreading is characterized by a temperature inversion at 18°C. The magnitude of the inversion is as large as 1.5°C or more at 1.5°N. Similar inversion of temperature have been often observed in the Equatorial Countercurrent and Undercurrent not only in the western Pacific but also in the central Pacific (YOSIDA *et al.*, 1959; YAMANAKA *et al.*, 1965; MONTGOMERY & STROUP, 1962, etc.). The inversion in the present case is associated with lower salinity (Fig. 8) and is hydrostatically stable (see the T-S curve at Ry 3066 in Fig. 9). Similar less saline waters are seen in the Equatorial Countercurrent or Undercurrent on the section at 149°E in February, 1958 (YOSIDA *et al.*, 1959).

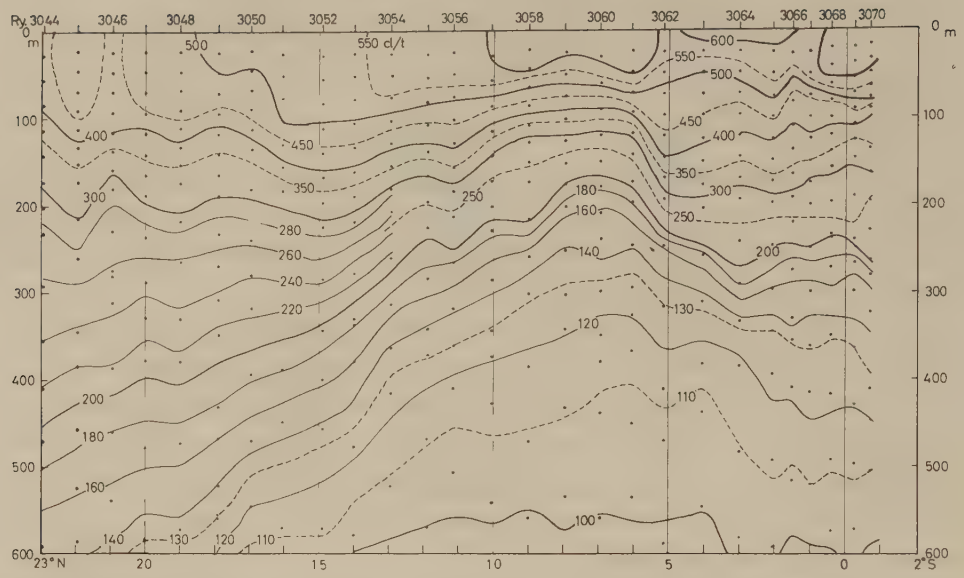

Fig. 5. Vertical section of thermosteric anomaly in the upper 600 m of the equatorial current system at 137°E in January 1967, vertical exaggeration, 2760.

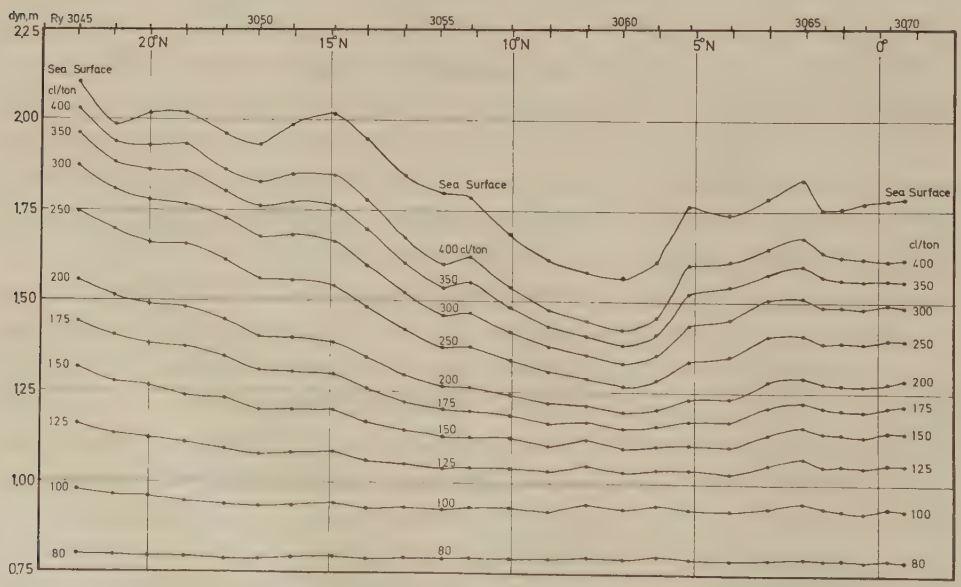

Fig. 6. Acceleration potential on isanosteric surfaces relative to the 1000 db surface in the equatorial current system at 137°E in January 1967.

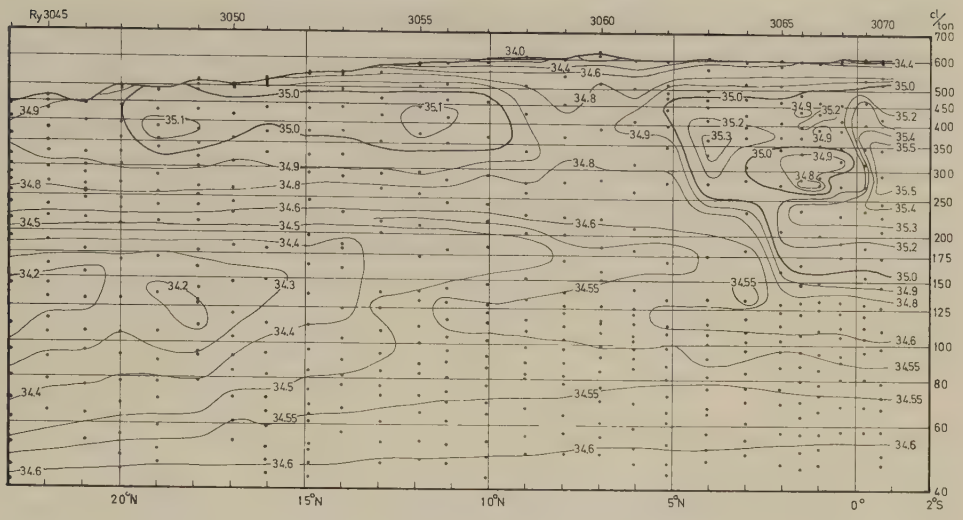

(a)

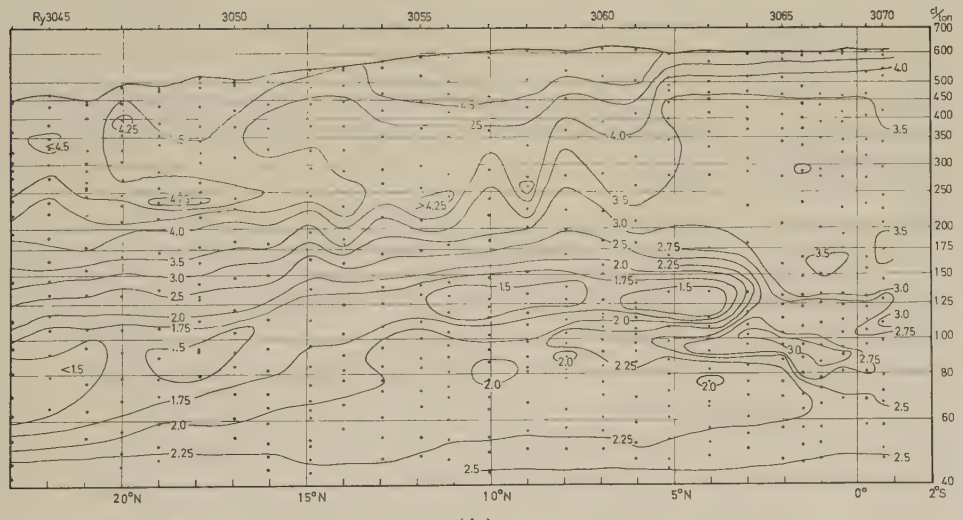

(b)

Fig. 7. Meridional sections of salinity (a) and oxygen content (b) against thermosteric anomaly in logarithmic scale in the equatorial current system at 137°E in January 1967.

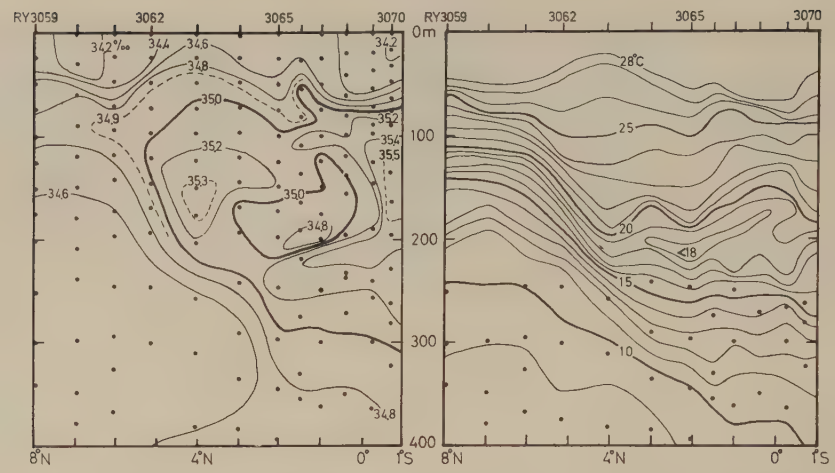

Fig. 8. Vertical sections of temperature and salinity in the upper 400 m layer of the Equatorial Countercurrent and Undercurrent at 137°E in January 1967, vertical exaggeration, 2760.

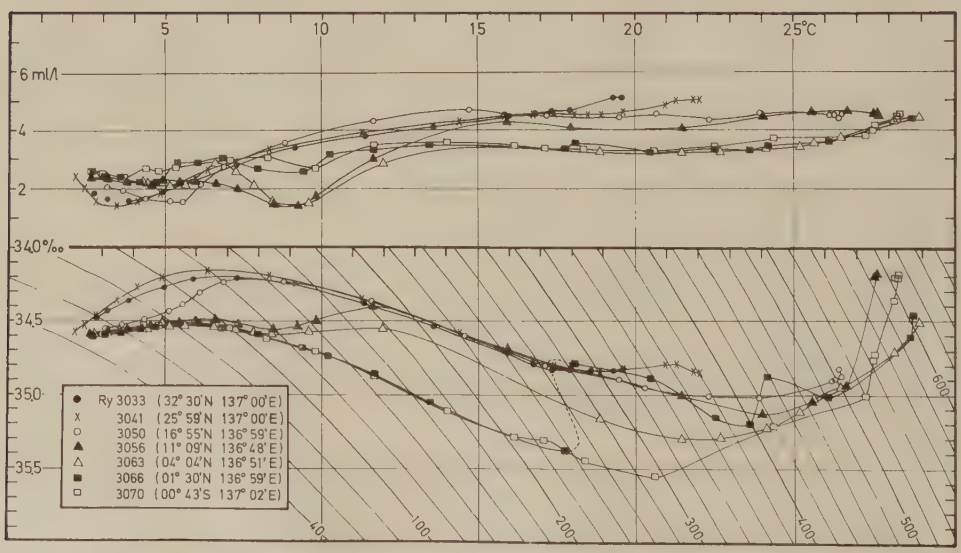

Fig. 9. Temperature-salinity and temperature-oxygen relationships at specified stations of the section at 137°E in January 1967.

The less saline water with temperature of 18 to 20°C, with salinity of 34.8 to 34.9‰ and with thermosteric anomaly of 250 to 300 cl/t may originate in the southern part of the North Equatorial Current. The map of salinity on the isanosteric surface of 300 cl/t made by CANNON (1966) indicates that a tongue of low salinity stretches from the North Equatorial Current region to the Equatorial Countercurrent or Undercurrent west of the Palau Islands.

These two isolated waters stated above are characteristic waters of the Equatorial Countercurrent and Undercurrent, and they are less than 100 m in the vertical extent. The mosaic distribution of these waters suggests a medium-scale motion or mixing, which may be equivalent to the medium-scale structure described by HAMON (1967) in the equatorial Indian Ocean.

The most saline water centered at 300 cl/t at 150 m south of the equator (Fig. 8) is carried to the west by currents close to the coast of New Guinea (Fig. 4). The water comes through the Solomon Sea or the Coral Sea from the tropical South Pacific. It is one of the most important waters of the Equatorial Undercurrent (TSUCHIYA, to be published). Most saline waters might be transported by the south Equatorial Current from the South Pacific to the North Pacific more in spring to fall of the northern hemisphere than in winter.

5-3 Intermediate waters

As described in Section 3-2, a well-defined salinity minimum is present in intermediate depths from Japan all the way to 3°N (Fig. 2 b). The core of the salinity minimum is found on the 125 cl/t surface from Japan to the middle of the North Equatorial Current and on the 175 cl/t surface in the southern part of the North Equatorial Current and in the Equatorial Countercurrent. The salinity minimum at 125 cl/t in the northern half of the section has been known as the major salinity minimum in the subtropical North Pacific Ocean and the minimum is formed by the Intermediate Water originating in the subarctic North Pacific (REID, 1965).

Since the salinity minimum at 175 cl/t in the southern half of the section seems to be a southward extension of the minimum at 125 cl/t in the north, it has been a common understanding that the salinity-minimum water of the North Pacific flows southward in the tropical and equatorial regions with asceding motion (KOENUMA, 1939; UDA, 1955; MAO & YOSHIDA, 1955, etc.). The remarkable difference in thermosteric anomaly between the minimum in the north and the minimum in the south does not seem to support the common idea. The meridional

profile of acceleration potential on the 125 cl/t surface (Fig. 6) shows that the salinity-minimum water at 125 cl/t flows to the west with the northern part of the North Equatorial Current as indicated by Reid (1965).

In contrast to the well-defined salinity minimum at 125 cl/t north of 15°N, there is a slight salinity maximum at 125 cl/t between 13°N and 3°N, and the maximum is associated with a distinct oxygen minimum (Figs. 7 a & 7 b). Fig. 6 suggests that both the salinity-minimum water at 175 cl/t and the oxygen-minimum water at 125 cl/t are transported to the west with the southern part of the North Equatorial Current and flows to the east with the Equatorial Countercurrent.

These two characteristic waters are also found in the southern part of the North Equatorial Current and in the Equatorial Countercurrent at 160°W (Reid, 1965), at 174°W and 172°E (Dobrovolsky *et al.*, 1960). The salinity minimum at 175 cl/t was observed in the section east of Mindanao of the Philippine Islands, which was made on board the *Atlantis II* in August 1965 (Cannon, personal communication). This suggests that the salinity-minimum water flows southward from the southern part of the North Equatorial Current to the original region of the Equatorial Countercurrent southwest of the Palau Islands.

Tsuchiya (to be published) shows that on the 160 cl/t surface a long tongue of low oxygen content stretches westward from Central America along the southern part of the North Equatorial Current, and that a tongue of low salinity stretches eastward from 175°W to 125°W in the zone of 3°N to 8°N. It is clearly demonstrated by Reid (1965) that the oxygen-minimum water at 125 cl/t in the southern part of the North Equatorial Current and in the Equatorial Countercurrent originates west of Central America. These descriptions suggest that the characteristic intermediate waters in the equatorial region flow westward with the North Equatorial Current and eastward with the Equatorial Countercurrent.

The deep oxygen-maximum layer from 80 cl/t to 110 cl/t between the equator and 8°N at 137°E is close to the upper part of the faint salinity minimum centered at 80 cl/t (Figs. 7 a & b). The oxygen-maximum water may come from the South Pacific Ocean as suggested by Reid (1965).

6. *Geostrophic flux*

6-1 *Flux of each current*

The geostrophic flux of each zonal current through the section was computed referred to the 1,000 db surface (Table 1). The flux of the Kuroshio, as much as 273 km^3/hr, is far more than the value computed before: the average value

and the maximum value computed from 32 crossings of the Kuroshio at 136°E in 1952 to 1953 are 174 km³/hr and 223 km³/hr, respectively (MASUZAWA, 1954): the geostrophic computation relative to the 2,000 db surface gives 247 km³/hr at 136.5°E and 260 km³/hr at 144°E (MASUZAWA, 1964 b, 1965).

The flux of the Kuroshio countercurrent is as much as 162 km³/hr and is 59% of the Kuroshio flux. Therefore, the net eastward flux over the depth of 1,000 m south of Japan is 111 km³/hr, but the real net eastward flux could be larger if the flux below 1,000 m would be taken into account.

In the weak-current zone of the subtropics, the net zonal flux is nearly zero, 0.3 km³/hr eastward, in spite of the presence of the eastward "Subtropical Countercurrent" at 17°N to 15°N.

The flux of the North Equatorial Current, amounting to 224 km³/hr, almost equals the average flux (244 km³/hr) calculated from three sections at 130°E, 140°E and 151°E which were made during the Equapac Expedition in summer, 1956 (MASUZAWA, 1964 a). The flux at 137°E consists of 79 km³/hr in the northern part and 145 km³/hr in the southern part.

The flux of the Equatorial Countercurrent, 234 km³/hr, is approximately equal to that of the North Equatorial Current. YOSIDA, *et al.* (1959) calculated the flux of the Equatorial Countercurrent and Undercurrent referred to 800 m from the results obtained by direct current measurements at four sections of 147°E, 149°E, 151°E and 153°E in January to February, 1958. The average of the net eastward fluxes in the equatorial region is as much as 279 km³/hr, but the flux cannot be divided into the Countercurrent and the Undercurrent. The geostrophic flux of the Countercurrent and that of the Undercurrent over the 300 db surface at 150°W are as much as 74 km³/hr and 123 km³/hr, respectively. According to a simplified computation of the Equatorial Countercurrent flux by WYRTKI & KENDALL (1967), there is a big fluctuation with time and space in the geostrophic flux. They show that the flux generally decreases eastward, and is relatively small in March to June, particulaly in the central and eastern Pacific. In the Equatorial Countercurrent west of 150°E, the maximum, minimum and average values of the flux computed by WYRTKI & KENDALL (1967) are as much as 300 km³/hr, 50 km³/hr, and 150 km³/hr, respectively.

Since the current field south of 2°N in the present section does not seem to be in geostrophic balance, the geostrophic flux there was not calculated. However, direct current measurements near the equator give an idea of a big eastward flux by the New Guinea Coastal Current or the Equatorial Undercurrent, or by both.

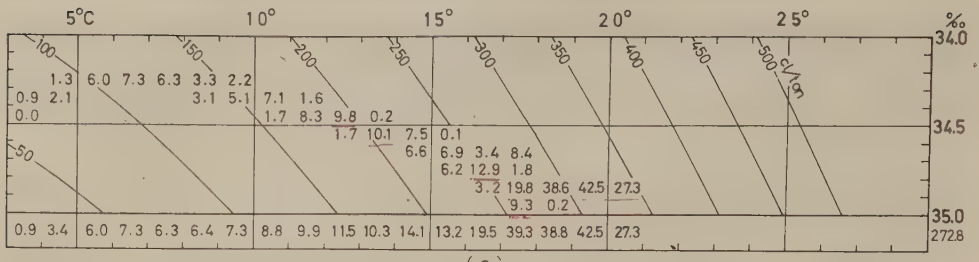
5°C
10°
15°
20°
25°
‰
34.0
34.5
35.0
cl/10m
100
150
200
250
300
350
400
450
500
50
0.9 3.4 | 6.0 7.3 6.3 6.4 7.3 | 8.8 9.9 11.5 10.3 14.1 | 13.2 19.5 39.3 38.8 42.5 | 27.3
272.8

(a)

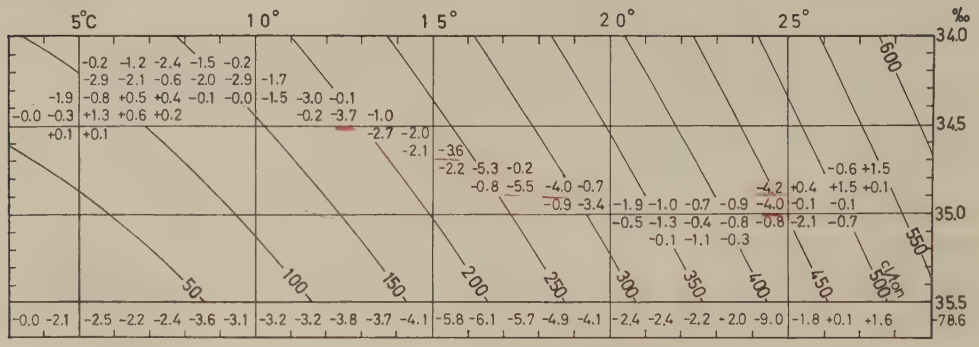
5°C
10°
15°
20°
25°
‰
34.0
34.5
35.0
35.5
cl/10m
50
100
150
200
250
300
350
400
450
500
550
600
-0.0 -2.1 | -2.5 -2.2 -2.4 -3.6 -3.1 | -3.2 -3.2 -3.8 -3.7 -4.1 | -5.8 -6.1 -5.7 -4.9 -4.1 | -2.4 -2.4 -2.2 -2.0 -9.0 | -1.8 +0.1 +1.6
78.6

(b)

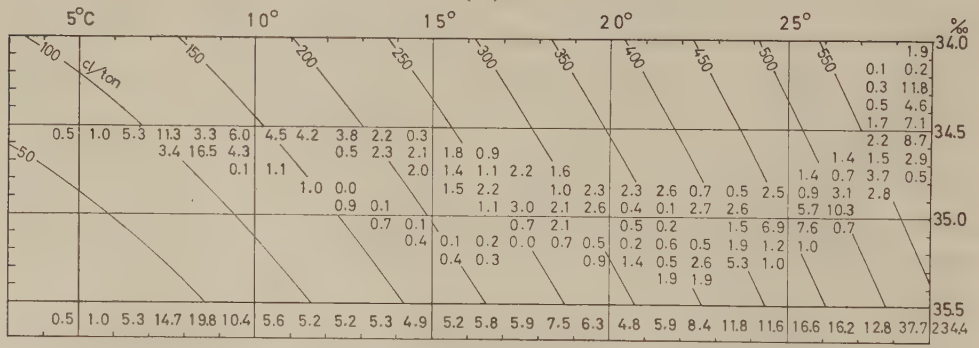
5°C
10°
15°
20°
25°
‰
34.0
34.5
35.0
35.5
cl/10m
50
100
150
200
250
300
350
400
450
500
550
0.5 | 1.0 5.3 14.7 19.8 10.4 | 5.6 5.2 5.2 5.3 4.9 | 5.2 5.8 5.9 7.5 6.3 | 4.8 5.9 8.4 11.8 11.6 | 16.6 16.2 12.8 37.7
234.4

(c)

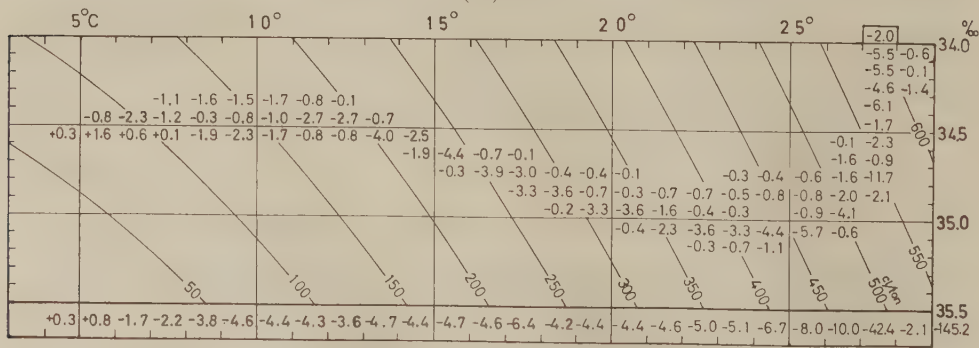
5°C
10°
15°
20°
25°
‰
34.0
34.5
35.0
35.5
cl/10m
50
100
150
200
250
300
350
400
450
500
550
600
+0.3 | +0.8 -1.7 -2.2 -3.8 -4.6 | -4.4 -4.3 -3.6 -4.7 -4.4 | -4.7 -4.6 -6.4 -4.2 -4.4 | -4.4 -4.6 -5.0 -5.1 -6.7 | -8.0 -10.0 -42.4 -2.1
145.2

(d)

Fig. 10. Geostrophic fluxes ($km^3 \cdot hr^{-1}$) relative to the 1000 db surface of the Kuroshio (a), of the northern half of the North Equatorial Current (b), of the southern half (c), and of the Equatorial Countercurrent (d) at 137°E in January 1967. Positive signs mean eastward. As for the limit of each current, refer to Table 1.

The net flux through the section at 137°E, excluding north of 33°30'N and south of 2°N, is eastward at 121 km^3/hr. In addition, there are a large amount of eastward fluxes by the New Guinea Coastal Current, by the Equatorial Undercurrent near the equator. If the water budget in the western North Pacific west of the section at 137°E is stationarily accomplished, the net eastward flux mentioned before, though unreliable, should be canceled with westward fluxes by deep currents below 1,000 m, if present, by drift currents due to the Trade Winds, and by the coastal current close to New Guinea, and also with the fluxes through the East Indian Archipelago from the Indian Ocean.

6-2 Geostrophic fluxes on T-S diagram

The present method for computing geostrophic fluxes on a temperature-salinity diagram (Fig. 10) is the same as used in the computation of the North Equatorial Current (Masuzawa, 1964 a).

As mentioned before, there is a large difference in water characteristics between the northern half and the southern half of the North Equatorical Current (Figs. 10 b & c). The first mode with respect to temperature is centered in the classes of 24 to 25°C in the northern half of the North Equatorial Current and in the classes of 27 to 28°C in the southern half of it. The large flux in the less saline surface layer (less than 34.4‰) is one of the most outstanding features in the southern part of the North Equatorial Current.

The slight mode at 15° to 18°C formed by the "Subtropical Mode Water" is found not only in the northern part of the North Equatorial Current but also in the southern part of it.

The intermediate waters below 200 cl/t carried westward by the northern part of the North Equatorial Current are generally less saline than those by the southern part. In fact, the least saline waters less than 34.3‰ are not present in intermediate depths of the southern part of the North Equatorial Current. Another point is that fluxes of relatively saline waters below 125 cl/t in the northern part and below 110 cl/t in the southern part are eastward.

More than half of the Kuroshio flux is formed by the surface mixed layer which is warmer than 17°C (Fig. 10 a). Though the Kuroshio is thought to be

a continuation of the northern part of the North Equatorial Current, it takes about one month and half to flow from the North Equatorial Current region at 137°E to the Kuroshio region at 137°E, if the average current speed is assumed to be 2 knots. While the Kuroshio flows along Luzon, Taiwan, the Ryukyu Islands, Kyushu and Shikoku, the water characteristics are much changed by vertical and lateral mixing, so that neither the most saline waters higher than 35‰ in the surface layer, nor the least saline waters lower than 34.2‰ in the intermediate layer appear in the Kuroshio at 137°E.

Equatorial Countercurrent water (Fig. 10 d) is formed both by the southern part of the North Equatorial Current and by South Equatorial Current water. Therefore, many temperature-salinity classes are found between 150 cl/t and 450 cl/t. These water characteristics in their classes are original waters not only of the Equatorial Countercurrent to the east but also of Equatorial Undercurrent waters to the east (MONTGOMERY & STROUP, 1962). The intermediate mode at 100 cl/t to 140 cl/t is formed by the salinity-maximum and oxygen-minimum water originating off Central America.

Acknowledgments: The author is grateful to members of the scientific party, officers and crew aboard the *Ryofu Maru*, Japan Meteorological Agency for their cooperation. He wishes to express thanks to Dr. M. TSUCHIYA for his useful suggestions and comments, and he is indebted to Miss Y. NIIZAKI for her assistance in the preparation of this manuscript.

References

BOGDANOV, C. H. & B. G. POPOV (1960): Currents of the surface layer of the western Pacific (in Russian). *Trudy, Inst. Okeanol. Akad. Nauk, SSSR*, **40**, 135–142.

BOGOROV, B. G., A. D. DOBROVOLSKY, B. P. PETELIN & I. V. SERGEEV (1960): First expeditions of the R/V "*Vityaz*" as part of the programme of the International Geophysical Year (Cruise 25, 26 and 27) (in Russian). *Trudy, Inst. Okeanol. Akad. Nauk, SSSR*, **40**, 3–22.

BURKOV, V. A. & I. M. OVCHINNIKOV (1960): Investigations of equatorial currents to the north of New Guinea (in Russian). *Trudy, Inst. Okeanol. Akad. Nauk, SSSR*, **40**, 121–134.

CANNON, G. A. (1966): Tropical waters in the western Pacific Ocean, August-September 1957. *Deep-Sea Res.*, **13**, 1139–1148.

DOBROVOLSKY, A. D., V. V. LEONTYEVA, & V. I. KUKSA (1960): On the characteristics of the stratification and water mass in the western and central part of the Pacific (in Russian). *Trudy, Inst. Okeanol. Akad. Nauk, SSSR*, **40**, 47–57.

FUGLISTER, F. C. (1963): Gulf Stream '60. *Progress in Oceanography*, **1**, 265–373.

HAMON, B. V. (1967): Medium-scale temperature and salinity structure in the upper 1500 m in the Indian Ocean. *Deep-Sea Res.*, **14**, 169-182.

ISTOSHIN, YU. V., & A. A. KALASHNIKOV (1965): The Cromwell Current in the western Pacific (in Russian). *Okeanologiia*, **5**, 954-958.

ISTOSHIN, YU. V. (1966): Particular features of water temperature distribution in the pre-equatorial zone of the Pacific Ocean (in Russian). *Okeanologiia*, **6**, 46-52.

KNAUSS, J. A. (1960): Measurements of the Cromwell Current. *Deep-Sea Res.*, **6**, 265-286.

KOENUMA, K. (1939): On the hydrography of the south-western part of the North Pacific and the Kuroshio. Part III, *Mem. Imp. Mar. Observ., Kobe*, **7**, 41-114.

KORT, V. G., V. A. BURKOV, & K. A. CHEKOTILLO (1966): Recent data on the equatorial currents in the western part of the Pacific (in Russian). *Dokl. Akad. Nauk, SSSR*, **171**, 337-339.

MAO, HAN-LEE & K. YOSHIDA (1955): Physical oceanography in the Marshall Islands Area. *Geological Survey Professional Paper* **260-R**, 645-684.

MASUZAWA, J. (1954): On the Kuroshio south of Shiono-misaki of Japan. *Oceanogr. Mag.*, **6**, 25-33.

MASUZAWA, J. (1955): An outline of the Kuroshio in the eastern sea of Japan. *Oceanogr. Mag.*, **7**, 29-48.

MASUZAWA, J. (1964 a): A typical hydrographic section of the Kuroshio Extension. *Oceanogr. Mag.*, **16**, 21-30.

MASUZAWA, J. (1964 b): Flux and water characteristics of the Pacific North Equatorial Current. *Studies on Oceanography*, 121-128.

MASUZAWA, J. (1965): Water characteristics of the Kuroshio. *Oceanogr. Mag.*, **17**, 37-47.

MASUZAWA, J. (1967): *Ryofu-Maru's* survery for C S K, January to March 1967. *Oceanogr. Mag.*, **19**, 1-5.

MONTGOMERY, R. B. & A. F. SPILHAUS (1941): Examples and outline of certain modifications in upper-air analysis. *J. Aero. Sci.*, **8**, 276-283.

MONTGOMERY, R. B. (1954): Analysis of a *Hugh M. Smith* oceanographic section from Honolulu southward across the equator. *Jour. Mar. Res.*, **13**, 67-75.

MONTGOMERY, R. B. & W. S. WOOSTER (1954): Thermosteric anomaly and the analysis of serial oceanographic data. *Deep-Sea Res.*, **2**, 63-70.

MONTGOMERY, R. B. (1962): Equatorial Undercurrent observations in Review. *Jour. Oceanogr. Soc. Japan*, 20th Anniversary Volume, 487-498.

MONTGOMERY, R. B. & E. D. STROUP (1962): Equatorial waters and currents at 150°W in July-August 1952. *Johns Hopkins Oceanographic studies*, No. **1**, 68 pp.

REID, J. L. Jr. (1965): Intermediate waters of the Pacific Ocean. *Johns Hopkins Oceanographic Studies*, No. **2**, 85 pp.

ROCHFORD, D. J. (1960): The intermediate depth waters of the Tasman and Coral Seas. I. The 27.20 σ_t surface. *Aust. J. Mar. Freshw. Res.*, **11**, 127-147.

ROCHFORD, D. J. (1960): The intermediate depth waters of the Tasman and Coral Seas. II. The 26.80 σ_t surface. *Aust. J. Mar. Freshw. Res.*, **11**, 148-165.

TAKAHASHI, T. (1959): Hydrographical researches in the western equatorial Pacific. *Mem. Fac. Fish., Kagoshima Univ.*, **7**, 141-147.

TAKAHASHI, T., M. CHAEN & S. UEDA (1960): Report of the *Kagoshima-Maru* IGY Cruise, 1958. *Mem. Fac. Fish., Kagoshima Univ.*, **8**, 82-86.

TSUCHIYA, M. (1961): An oceanographical description of the equatorial current system of the western Pacific. *Oceanogr. Mag.*, **13**, 1-30.

TSUCHIYA, M.: Upper waters and circulation of the intertropical Pacific Ocean. to be

published on *Johns Hopkins Oceanographic Studies*.

UDA, M. (1955): On the subtropical convergence and the currents in the northwestern Pacific. *Rec. Oceanogr. Works Japan*, **2**, 145-150.

VOORHIS, A. D. & J. B. HERSEY (1964): Oceanic thermal fronts in the Sargasso Sea. *J. Geophys. Res.*, **69**, 3809-3814.

WORTHINGTON, L. V. (1959): The 18°C water in the Sargasso Sea. *Deep-Sea Res.*, **5**, 297-305.

WYRTKI, K. (1961): Physical oceanography of the Southeast Asian Waters. Scientific results of marine investigations of the South China Sea and the Gulf of Thailand, 1959-1961. *Naga Rep.*, **2**, 195 pp.

WYRTKI, K. & R. KENDALL (1967): Transports of the Pacific equatorial counter-current. *J. Geophys. Res.*, **72**, 2073-2076.

YAMANAKA, H., N. ANRAKU & J. MORITA (1965): Seasonal and long-term variations in oceanographic conditions in the western North Pacific Ocean (in Japanese). *Rept. Nankai Regional Fisheries Res. Laboratory*, **22**, 35-70.

YOSHIDA, K. & T. KIDOKORO (1967): A Subtropical Countercurrent in the North Pacific, An eastward flow near the Subtropical Convergence. *Jour. Oceanogr. Soc. Japan*, **23**, 88-91.

YOSIDA, S., H. NITANI & N. SUZUKI (1959): Report of multiple ship survey in the equatorial region (IGY), Jan.-Feb., 1958 (in Japanese). *Bull. Hydrographic Office*, **59**, 1-30.

The Oceanographical Magazine
Vol. 19, No. 2, December 1967

Numerical Experiments of the Wind-driven Circulation in the Pacific Ocean

By

Takeo Ueno

Kobe Marine Observatory

(Received November 24, 1967)

Abstract: Numerical experiments for the wind-driven general circulation in the ocean were made. The modeled ocean is the Pacific Ocean in January and July represented by the five-degree spherical meshes from 55°N to 85°S in the latitude and from 115°E to 75°W in the longitude, where the sea from the Antarctic to Australia and the Drake Passage between the Antarctic and South America are closed. The depth is given 200 meters uniformly, and the wind stress or the bottom friction is assumed to be proportional to the second power of wind or current velocity and in inverse proportion to the depth, where the frictional coefficient γ^2 is put to be $2.6 \cdot 10^{-3}$. Under the above conditions the equations of motion, with the Coriolis, surface gradient, wind stress, bottom friction, lateral mixing and non-linear terms, are composed and transformed into the mass transport equations together with the continuity equation. Further they are changed into the finite difference forms so that we may succesively integrate them by the "primitive method," where the 600-second time step interval is used in connection with the stability. The finite difference schemes for the equations of motion and the non-linear terms are newly designed and their stability and energy conservation are discussed and tested. After the 2000-hour computations the solutions nearly reach the steady states, that is, the current velocities and sea-level elevations surely converge to the finite values and take the definite distributions on the whole, however, we still have the strong acceleration in the seas around the Antarctic. The wind systems in January and July are taken from the wind stream line charts in МОРСКОЙ АТЛАС ТОМ II (1953). The lateral mixing coefficient A_l is given such the value that the amount of mass transport of the Kuroshio becomes closest possible to the observed one. In the studies A_l is put to be $5 \cdot 10^9$ and the mass transport of the Kuroshio becomes $41.6 \cdot 10^{12}$ in January and $42.5 \cdot 10^{12}$ in July. The computed current charts show the property of main currents, that is, the Kuroshio, the East Australian Current, the North Equatorial Counter Current, the California Current, the Humboldt Current, and so on. The author is also much interested in the computed elevations and some comparisons are made between the computed elevations and the observed ones obtained at the tidal stations in the Pacific Ocean. Above all, the fact that the sea-level, along the coast of Japan being washed by the Kuroshio is making the surface sloping

down from south to north, and its seasonal variations are examined by both computations and observations. Finally the resultant force and angular moment belonging to each term in the equations of motion are reckoned, and the mechanism of both balance of forces and conservation of angular moments are made clear.

1. *Equations of motion and continuity*

We take a spherical co-ordinate system O-xyz fixed relative to the globe, as shown in Figure 1. The origin O is at any point on the undisturbed sea surface of the rotating globe, whose longitude is φ and the co-latitude is θ. The axes x, y and z are taken southward, eastward and vertically upward, respectively. Now we discuss the wind-driven ocean current in the homogeneous sea with a uniform depth h, which is assumed to be 200 m in the computations. If we denote u and v the vertical mean velocity component along the x and y axis respectively, and by ζ the elevation of disturbed sea surface from $z=0$ along the axis z, the equations of motion for the sea water with a unit mass, and of continuity for the vertical water column with a unit section are as follows:

$$\frac{\partial u}{\partial t}=au+cv+p+A_t\Delta_1 u\,, \tag{1}$$

$$\frac{\partial v}{\partial t}=bv+du+q+A_t\Delta_1 v\,, \tag{2}$$

$$\frac{\partial \zeta}{\partial t}=-h\left(\frac{\partial u}{\partial x}+\frac{\partial v}{\partial y}\right), \tag{3}$$

where

$$a=-F-\frac{\partial u}{\partial x}\,,$$

$$b=-F-\frac{\partial v}{\partial y}\,,$$

$$c=f-\frac{\partial u}{\partial y}\,,$$

$$d=-f-\frac{\partial v}{\partial x}\,,$$

$$p=R-g\frac{\partial \zeta}{\partial x}\,,$$

$$q=S-g\frac{\partial \zeta}{\partial y}\,,$$

$$F=\gamma^2\sqrt{u^2+v^2}/h\,,$$

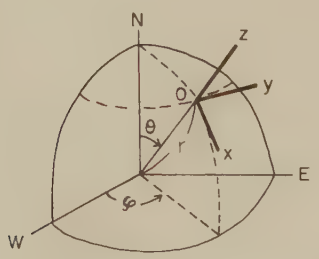

Fig. 1. The spherical co-ordinate system.

$f=2\omega\cos\theta$,

$R=\frac{\rho_a\gamma^2}{h}\sqrt{W_x^2+W_y^2}\ W_x$,

$S=\frac{\rho_a\gamma^2}{h}\sqrt{W_x^2+W_y^2}\ W_y$,

$W_x=x$ component of wind velocity,

$W_y=y$ domponent of wind velocity,

$\Delta_1=\frac{\partial^2}{\partial x^2}+\frac{\partial^2}{\partial y^2}$,

$\frac{\partial}{\partial x}=\frac{\partial}{r\partial\theta}$,

$\frac{\partial}{\partial y}=\frac{\partial}{r\sin\theta\partial\varphi}$,

g=the acceleration due to gravity, 980,

ω=the angular velocity of the earth rotation, $7.292\cdot10^{-5}$,

ρ_a=the density of air, $1.23\cdot10^{-3}$,

γ^2=the frictional coefficient on both sea bottom and surface, $2.6\cdot10^{-3}$,

A_l=the horizontal mixing coefficient, $5\cdot10^9$,

r=the mean radius of the earth, $6.37123\cdot10^8$,

h=the depth, $2\cdot10^4$.

The numerical values are all in C. G. S. unit.

2. *Steady solution*

If we assume a, b, c and d to be constant, the equations (1) and (2) become the simultaneous linear equations with u and v. Then, as written in the last part of Section 3, we can separate the mixing terms $A_l\Delta_1 u$, $A_l\Delta_1 v$ and compute them independently from the original equations. After the current pattern reaches the steady state by the long lasting steady winds, the equations for u, v will take the next forms;

$$\left.\begin{aligned} au+cv+p=0\,,\\ bv+du+q=0\,.\end{aligned}\right\} \qquad (4)$$

If we know the distributions of wind stress R, S and the elevation ζ, we can obtain the following steady solutions of u, v from the above equations:

$$u=-\left[\left(F+\frac{\partial v}{\partial y}\right)\left(p-g\frac{\partial\zeta}{\partial x}\right)+\left(f-\frac{\partial u}{\partial y}\right)\left(q-g\frac{\partial\zeta}{\partial y}\right)\right]\ det\,,$$

$$\left.\begin{aligned} v &= -\left[\left(F+\frac{\partial u}{\partial x}\right)\left(q-g\frac{\partial \zeta}{\partial y}\right)+\left(-f-\frac{\partial v}{\partial x}\right)\left(p-g\frac{\partial \zeta}{\partial x}\right)\right]/det\,, \\ det &\equiv \left(f-\frac{\partial u}{\partial y}\right)\left(-f-\frac{\partial v}{\partial x}\right)-\left(F+\frac{\partial u}{\partial x}\right)\left(F+\frac{\partial v}{\partial y}\right). \end{aligned}\right\} \qquad (5)$$

The unknown factors $\frac{\partial \zeta}{\partial x}$ and $\frac{\partial \zeta}{\partial y}$ in the above equations are decided by the equation (3). The practical procedures in computations for u, v and ζ are as follows: First, compute u and v, putting F, $\frac{\partial \zeta}{\partial x}$, $\frac{\partial u}{\partial x}$, etc. in the formula (5) to be zero. Second, substitute these values of u and v in the continuity equation (the undermentioned finite difference form (12) or (17) deduced from the formula (3)), then we obtain the sea-level elevation ζ corresponding to the above values of u and v and the wind system. Let us call the first and second procedures one step. After the first step we follow the second step, that is, the values of u, v and ζ obtained by the first step are substituted in the right side of equations (5) and we get the new values of u and v, which are substituted in the formula (12) or (17) again and we get the new value of ζ. Repeat the step many times, and u, v and ζ gradually converge to constant values, which give the distributions of currents and elevations equilibrium to the given wind stress system.

According to our numerical experiments, the convergency in the steady-state computations is twice as rapid as in the non-steady case, and the former results are much similar to the latter except near the equator, where the value of *det* in (5) becomes very small and we cannot use this steady method. So, in our numerical experiment for the steady solutions, along the zone from $\theta=80°$ to $\theta=100°$ the non-steady solutions, are used. It is true that our steady solutions are very convenient, but the currents near the equator play the most important role in the general circulations. By this reason we must give up this method in our studies.

3. *Non-steady solution*

In this case our equations of motion take the next forms:

$$\left.\begin{aligned} \frac{\partial u}{\partial t} &= au+cv+p, \\ \frac{\partial v}{\partial t} &= bv+du+q. \end{aligned}\right\} \qquad (6)$$

Effects of mixing terms are computed separately from the above equations as

shown in the last part of this section. Now we consider the above equations at the time $t+1$, and replace $\frac{\partial u}{\partial t}$, $\frac{\partial v}{\partial t}$ by the central difference $\frac{u^{t+2}-u^t}{\Delta t}$, $\frac{v^{t+2}-v^t}{\Delta t}$ and u^{t+1}, v^{t+1} on the right side by $(u^{t+2}+u^t)/2$, $(v^{t+2}+v^t)/2$ respectively. Then the equations (6) become

$$\left.\begin{aligned}\frac{u^{t+2}-u^t}{\Delta t}&=a\frac{u^{t+2}+u^t}{2}+c\frac{v^{t+2}+v^t}{2}+p^{t+1},\\ \frac{v^{t+2}-v^t}{\Delta t}&=b\frac{v^{t+2}+v^t}{2}+d\frac{u^{t+2}+u^t}{2}+q^{t+1},\end{aligned}\right\}\qquad(7)$$

where a, b, c and d are assumed to be constant. Then we have

$$\left.\begin{aligned}u^{t+2}&=\Big[\Big\{\Big(1+\frac{a\Delta t}{2}\Big)\Big(1-\frac{b\Delta t}{2}\Big)+\frac{c\Delta t}{2}\frac{d\Delta t}{2}\Big\}u^t+c\Delta t v^t\\&\quad+\Big(1-\frac{b\Delta t}{2}\Big)p^{t+1}\Delta t+\frac{c\Delta t}{2}q^{t+1}\Delta t\Big]\Big/Det,\\ v^{t+2}&=\Big[\Big\{\Big(1+\frac{b\Delta t}{2}\Big)\Big(1-\frac{a\Delta t}{2}\Big)+\frac{d\Delta t}{2}\frac{c\Delta t}{2}\Big\}v^t+d\Delta t u^t\\&\quad+\Big(1-\frac{a\Delta t}{2}\Big)q^{t+1}\Delta t+\frac{d\Delta t}{2}p^{t+1}\Delta t\Big]\Big/Det,\\ Det&\equiv\Big(1-\frac{a\Delta t}{2}\Big)\Big(1-\frac{b\Delta t}{2}\Big)-\frac{c\Delta t}{2}\frac{d\Delta t}{2}.\end{aligned}\right\}\qquad(8)$$

Let us estimate the values of $\frac{a\Delta t}{2}$, $\frac{b\Delta t}{2}$, $\frac{c\Delta t}{2}$ and $\frac{d\Delta t}{2}$ in the above equations. According to the definitions in Section 1,

$$\frac{a\Delta t}{2}=\Big(-\frac{\gamma^2\sqrt{u^2+v^2}}{h}-\frac{\partial u}{\partial x}\Big)\frac{\Delta t}{2},$$

$$\frac{d\Delta t}{2}=\Big(-\frac{\gamma^2\sqrt{u^2+v^2}}{h}-\frac{\partial v}{\partial y}\Big)\frac{\Delta t}{2},$$

$$\frac{c\Delta t}{2}=\Big(f-\frac{\partial u}{\partial y}\Big)\frac{\Delta t}{2},$$

$$\frac{b\Delta t}{2}=\Big(-f-\frac{\partial v}{\partial x}\Big)\frac{\Delta t}{2}.$$

Our grid points consist of 5-degree meshes. Elevation points (black spots) and current points (black squares) are arranged alternately (Fig. 2). At a co-latitude θ the grid interval Δx and Δy takes the value $r\Delta\pi$ and $r\Delta\pi\sin\theta$ respectively, where $\Delta\pi$ is 0.174533, the value of 10 degrees measured

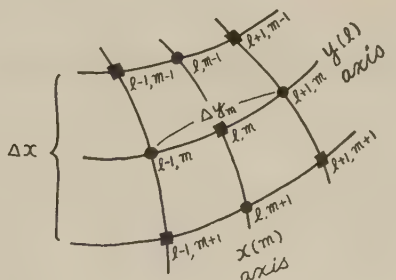

Fig. 2. The arrangement of current (black square) and elevation (black spot) points.

by the radian. So Δx is $11.2 \cdot 10^7$ cm everywhere and the least value of Δy is $0.974 \cdot 10^7$ cm along the southern boundary. On the other hand the maximum current velocity is of the order of 10^2 cm$\cdot$sec^{-1} as observed in the Kuroshio. Then horizontal gradients of the current velocity are estimated at about 10^{-5}. The frictional term $\frac{\gamma^2\sqrt{u^2+v^2}}{h}$ also takes the value 10^{-5}, while Coriolis' parameter f takes the maximum value $14.3 \cdot 10^{-5}$ on the southern boundary. Our time interval Δt is $6 \cdot 10^2$ second in connection with the computational stability (Section 6).

Then, in equations (8), the second power terms of the type $\frac{a\Delta t}{2}$, $\frac{b\Delta t}{2}$ will be the order of 10^{-4}.

Therefore, neglecting these terms, we have

$$\left.\begin{aligned} u^{t+2} &= (1+a\Delta t)\,u^t + c\Delta t v^t + \left(1+\frac{a\Delta t}{2}\right)p^{t+1}\Delta t + \frac{c\Delta t}{2}q^{t+1}\Delta t\,, \\ v^{t+2} &= (1+b\Delta t)\,v^t + d\Delta t u^t + \left(1+\frac{b\Delta t}{2}\right)q^{t+1}\Delta t + \frac{d\Delta t}{2}p^{t+1}\Delta t\,. \end{aligned}\right\} \tag{9}$$

Putting

$$\left.\begin{aligned} A^T &\equiv 1+\frac{a\Delta t}{2} = \left[1-\frac{\gamma^2}{h}\sqrt{u^2+v^2}\,\frac{\Delta t}{2} - \frac{\partial u}{\partial x}\frac{\Delta t}{2}\right]^T, \\ B^T &\equiv 1+\frac{b\Delta t}{2} = \left[1-\frac{\gamma^2}{h}\sqrt{u^2+v^2}\,\frac{\Delta t}{2} - \frac{\partial v}{\partial y}\frac{\Delta t}{2}\right]^T, \\ C^T &\equiv \frac{c\Delta t}{2} = \left[f\frac{\Delta t}{2} - \frac{\partial u}{\partial y}\frac{\Delta t}{2}\right]^T, \\ D^T &\equiv \frac{d\Delta t}{2} = \left[-f\frac{\Delta t}{2} - \frac{\partial v}{\partial x}\frac{\Delta t}{2}\right]^T, \\ P^{t+1} &\equiv p^{t+1}\Delta t = R\Delta t - g\frac{\partial \zeta^{t+1}}{\partial x}\Delta t\,, \\ Q^{t+1} &\equiv q^{t+1}\Delta t = S\Delta t - g\frac{\partial \zeta^{t+1}}{\partial y}\Delta t\,, \end{aligned}\right\} \tag{10}$$

our prediction formulas for u and v become

$$\left.\begin{aligned} u^{t+2} &= (2A^T-1)\,u^t + 2C^T v^t + A^T P^{t+1} + C^T Q^{t+1}\,, \\ v^{t+2} &= (2B^T-1)\,v^t + 2D^T u^t + B^T Q^{t+1} + D^T P^{t+1}\,. \end{aligned}\right\} \tag{11}$$

On the other hand, transforming the continuity equation (3) into the finite difference form at the time $t+2$, we obtain the prediction equation for ζ as follows:

$$\zeta^{t+3} = \zeta^{t+1} - h\,div\,(u, v)^{t+2}\Delta t\,. \tag{12}$$

The procedures of computations for u, v and ζ are much the same as in the

case of steady solutions. At the initial state, u^t, v^t and ζ^{t+1} are zero. According to the definition, $A=B=1$, $C=\frac{f\Delta t}{2}$, $D=\frac{-f\Delta t}{2}$. With these coefficients, we first compute u^{t+2} and v^{t+2} by using the formula (11). Second substitute these u^{t+2} and v^{t+2} in the formula (12) and we obtain ζ^{t+3}, where the initial value ζ^{t+1} is null. The first and second procedure mentioned above is called one step. By one step we obtain u, v and ζ which have the value at the time $t=\Delta t$, and repeating this step n times we get the distributions of u, v and ζ at the time $n\Delta t$. As mentioned above, $\frac{a\Delta t}{2}$ etc. are of the order of 10^{-2} and we neglected their second terms. Leaving A, B, C and D as they are, we repeat our step n times. This means that the time interval for A, B, C and D is $n\cdot\Delta t=\Delta T$. If n is of the order of 10, $\frac{a\Delta T}{2}$ etc. become of the order of 10^{-1} and we cannot neglect their second power terms, and we have to compute A, B, C and D every n steps. In our procedure, n is 6 and Δt 10 minutes. Therefore, A, B, C and D are hourly computed. The sign T at the right shoulder in the formulas (10) and (11) are used in this sense.

Together with A, B, C and D, effects of horizontal mixing having the following forms will be taken into account:

$$\left.\begin{aligned}\frac{\partial u}{\partial t}&=A_l\Delta_1 u=A_l\left(\frac{\partial^2 u}{\partial x^2}+\frac{\partial^2 u}{\partial y^2}\right),\\ \frac{\partial v}{\partial t}&=A_l\Delta_l v=A_l\left(\frac{\partial^2 v}{\partial x^2}+\frac{\partial^2 v}{\partial y^2}\right).\end{aligned}\right\} \tag{13}$$

Their finite difference forms are

$$\left.\begin{aligned}u^{T+1}&=u^T+A_l\Delta T\left(\frac{\partial^2 u}{\partial x^2}+\frac{\partial^2 u}{\partial y^2}\right)^T,\\ v^{T+1}&=v^T+A_l\Delta T\left(\frac{\partial^2 v}{\partial x^2}+\frac{\partial^2 v}{\partial y^2}\right)^T.\end{aligned}\right\} \tag{14}$$

The sign T at the right shoulder means that the procedure is taken every one hour, samely as in the case of A, B, C and D.

4. The difference form of non-linear and mixing terms

In the rectangular meshes (Fig. 3) we consider the difference forms of the horizontal velocity gradients. Since the velocity and elevation point are situated alternately in our grid system, the difference form of $\frac{\partial u}{\partial x}$ at any point (l, m) becomes $\frac{u_{l,m+2}-u_{l,m-2}}{2\Delta x}$, but this scheme is accompanied with a large truncation

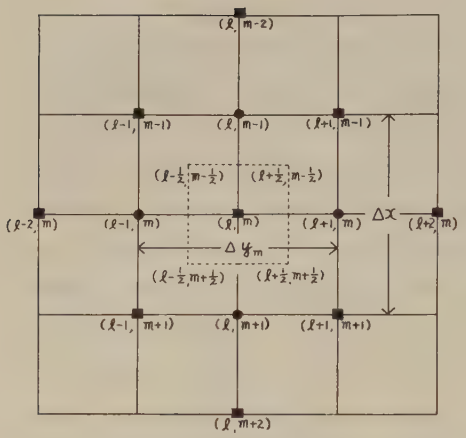

Fig. 3. The meshes relating to the difference scheme at a point (l, m) for non-linear and mixing terms (black square, current point; black spot, elevation point).

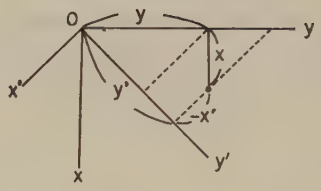

Fig. 4. The co-ordinate O-$x'y'$.

error because of a long interval $2\Delta x$. Now we try to obtain the difference form of the velocity gradients at any point (l, m) by use of the neighboring four points $(l\pm1, m\pm1)$ instead of $(l\pm2, m\pm2)$. For this purpose we take the new axes x' and y' making the angle 45° with the axes x and y (Fig. 4). Let u' and v' be the velocity component relating to the new axes. From the relations

$$-x' = (-x+y)/\sqrt{2}, \qquad y' = (x+y)/\sqrt{2},$$

we have

$$\frac{\partial x'}{\partial y} = -\frac{1}{\sqrt{2}}, \qquad \frac{\partial x'}{\partial x} = \frac{\partial y'}{\partial x} = \frac{\partial y'}{\partial y} = \frac{1}{\sqrt{2}}.$$

The difference form of $\dfrac{\partial u}{\partial x}$ will be then

$$\left[\frac{\partial u}{\partial x}\right]_{l,m} = \left[\frac{\partial u}{\partial x'}\frac{\partial x'}{\partial x} + \frac{\partial u}{\partial y'}\frac{\partial y'}{\partial x}\right]_{l,m}$$

$$= \frac{1}{\sqrt{2}}\left[\frac{u_{l-1,m+1}-u_{l+1,m-1}}{\sqrt{2}\,\Delta x} + \frac{u_{l+1,m+1}-u_{l-1,m-1}}{\sqrt{2}\,\Delta x}\right]$$

$$= \frac{1}{2\Delta x}\left[u_{l+1,m+1}-u_{l+1,m-1}+u_{l-1,m+1}-u_{l-1,m-1}\right].$$

Similarly we can get $\left[\dfrac{\partial u}{\partial y}\right]_{l,n}$, but in this case Δy is a function of m on the spherical surface (Figs. 2 and 5). Let this function be Δy_m, then we have

$$\left.\begin{aligned}\frac{\partial}{\partial x}\left\langle\begin{matrix}u\\v\end{matrix}\right\rangle_{l,m}&=\frac{1}{2\Delta x}\left[\left\langle\begin{matrix}u\\v\end{matrix}\right\rangle_{l+1,m+1}-\left\langle\begin{matrix}u\\v\end{matrix}\right\rangle_{l+1,m-1}+\left\langle\begin{matrix}u\\v\end{matrix}\right\rangle_{l-1,m+1}-\left\langle\begin{matrix}u\\v\end{matrix}\right\rangle_{l-1,m-1}\right],\\ \frac{\partial}{\partial y}\left\langle\begin{matrix}u\\v\end{matrix}\right\rangle_{l,m}&=\frac{1}{2\Delta y_m}\left[\left\langle\begin{matrix}u\\v\end{matrix}\right\rangle_{l+1,m+1}-\left\langle\begin{matrix}u\\v\end{matrix}\right\rangle_{l-1,m+1}+\left\langle\begin{matrix}u\\v\end{matrix}\right\rangle_{l+1,m-1}-\left\langle\begin{matrix}u\\v\end{matrix}\right\rangle_{l-1,m-1}\right].\end{aligned}\right\}\quad(15)$$

Further, using the above difference form we obtain

$$\begin{aligned}\left[\frac{\partial^2 u}{\partial x^2}\right]_{l,m}&=\frac{\partial}{\partial x}\,\frac{1}{2\frac{\Delta x}{2}}\left[u_{l+1/2,m+1/2}-u_{l+1/2,m-1/2}+u_{l-1/2,m+1/2}-u_{l-1/2,m-1/2}\right]\\&=\frac{1}{\Delta x^2}\left[(u_{l+1,m+1}-u_{l-1,m}+u_{l,m+1}-u_{l,m})-(u_{l+1,m}-u_{l-1,m-1}+u_{l,m}-u_{l,m-1})\right.\\&\quad\left.+(u_{l,m+1}-u_{l,m}+u_{l-1,m+1}-u_{l-1,m})-(u_{l,m}-u_{l,m-1}+u_{l-1,m}-u_{l-1,m-1})\right]\\&=\frac{1}{\Delta x^2}\left[(u_{l+1,m+1}+u_{l+1,m-1}+u_{l-1,m+1}+u_{l-1,m-1}-4\,u_{l,m})\right.\\&\quad\left.+2(u_{l,m+1}+u_{l,m-1})-2(u_{l+1,m}+u_{l-1,m})\right].\end{aligned}$$

Similarly

$$\begin{aligned}\left[\frac{\partial^2 u}{\partial y^2}\right]_{l,m}&=\frac{1}{\Delta y_m{}^2}\left[(u_{l+1,m+1}+u_{l+1,m-1}+u_{l-1,m+1}+u_{l-1,u_{m-1}}-4\,u_{l,m})\right.\\&\quad\left.-2(u_{l,m+1}+u_{l,m-1})+2(u_{l+1,m}+u_{l-1,m})\right]\end{aligned}$$

Hence the finite difference expression of $\Delta_1 u_{l,m}$ is

$$\begin{aligned}\Delta_1 u_{l,m}&=\left[\frac{\partial^2 u}{\partial x^2}+\frac{\partial^2 u}{\partial y^2}\right]_{l,m}=\left(\frac{1}{\Delta x^2}+\frac{1}{\Delta y_m{}^2}\right)\\&\quad\times\left[u_{l+1,m+1}+u_{l+1,m-1}+u_{l-1,m+1}+u_{l-1,m-1}-4\,u_{l,m}\right],\end{aligned}$$

and the difference forms of horizontal mixing equations (14) become

$$\begin{aligned}\left\langle\begin{matrix}u\\v\end{matrix}\right\rangle_{l,m}^{T+1}&=\left[1-4A_l\Delta T\left(\frac{1}{\Delta x^2}+\frac{1}{\Delta y_m{}^2}\right)\right]\left\langle\begin{matrix}u\\v\end{matrix}\right\rangle_{l,m}^{T}\\&\quad+A_l\Delta T\left(\frac{1}{\Delta x^2}+\frac{1}{\Delta y_m{}^2}\right)\left[\left\langle\begin{matrix}u\\v\end{matrix}\right\rangle_{l+1,m+1}+\left\langle\begin{matrix}u\\v\end{matrix}\right\rangle_{l+1,m-1}+\left\langle\begin{matrix}u\\v\end{matrix}\right\rangle_{l-1,m+1}\right.\\&\quad\left.+\left\langle\begin{matrix}u\\v\end{matrix}\right\rangle_{l-1,m-1}\right]^{T}.\end{aligned}\quad(16)$$

5. *The practical difference form on the spherical surface*

In the actual computations, the difference equations are given at every grid in the 5-degree meshes on the spherical surface as shown in Fig. 1. The continuity equation (12) at a elevation point (i, j) with the co-latitude θ_j in Figure 5 becomes

$$\begin{aligned}div\,(u, v)_{i,j}&=\left[r\Delta\pi\sin\theta_{j+1}u_{i,j+1}-r\Delta\pi\sin\theta_{j-1}u_{i,j-1}\right.\\&\quad\left.+r\Delta\pi v_{i+1,j}-r\Delta\pi v_{i-1,j}\right]/r\Delta\pi\sin\theta_j\cdot r\Delta\pi\,.\end{aligned}$$

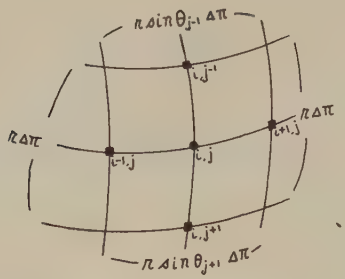

Fig. 5. The meshes relating to the difference scheme at a point (i, j) for the continuity equation (black square, current point; black spot, elevation point).

From the equation (12), we have

$$\zeta_{i,j}^{t+3}=\zeta_{i,j}^{t+1}-\frac{h\Delta t}{r\Delta\pi\sin\theta_j}[\sin\theta_{j+1}u_{i,j+1}-\sin\theta_{j-1}u_{i,j-1}+v_{i+1,j}-v_{i-1,j}]^{t+2}. \quad (17)$$

At *a* grid point (l, m) whose co-latitude is θ_m on the spherical surface, the formulas (15) take the following forms:

$$\frac{\partial}{\partial x}\left\langle\begin{matrix}u\\v\end{matrix}\right\rangle_{l,m}=\frac{1}{2r\Delta\pi}\left\langle\begin{matrix}UX\\VX\end{matrix}\right\rangle_{l,m},$$

$$\frac{\partial}{\partial y}\left\langle\begin{matrix}u\\v\end{matrix}\right\rangle_{l,m}=\frac{1}{2r\Delta\pi\sin\theta_m}\left\langle\begin{matrix}UY\\VY\end{matrix}\right\rangle_{l,m},$$

where,

$$\left\langle\begin{matrix}UX\\VX\end{matrix}\right\rangle_{l,m}=\left[\left\langle\begin{matrix}u\\v\end{matrix}\right\rangle_{l+1,m+1}-\left\langle\begin{matrix}u\\v\end{matrix}\right\rangle_{l+1,m-1}+\left\langle\begin{matrix}u\\v\end{matrix}\right\rangle_{l-1,m+1}-\left\langle\begin{matrix}u\\v\end{matrix}\right\rangle_{l-1,m-1}\right],$$

$$\left\langle\begin{matrix}UY\\VY\end{matrix}\right\rangle_{l,m}=\left[\left\langle\begin{matrix}u\\v\end{matrix}\right\rangle_{l+1,m+1}-\left\langle\begin{matrix}u\\v\end{matrix}\right\rangle_{l-1,m+1}+\left\langle\begin{matrix}u\\v\end{matrix}\right\rangle_{l+1,m-1}-\left\langle\begin{matrix}u\\v\end{matrix}\right\rangle_{l-1,m-1}\right].$$

Similarly

$$\left[\frac{\partial\zeta}{\partial x}\right]_{l,m}=\frac{1}{r\Delta\pi}[\zeta_{l,m+1}-\zeta_{l,m-1}],$$

$$\left[\frac{\partial\zeta}{\partial y}\right]_{l,m}=\frac{1}{r\Delta\pi\sin\theta_m}[\zeta_{l+1,m}-\zeta_{l-1,m}].$$

Substituting the above difference forms in the equations (10), we have

$$A_{l,m}^{T}=\left[1-\frac{\gamma^2\Delta t}{2h}\sqrt{u_{l,m}^2+v_{l,m}^2}-\frac{\Delta t}{4r\Delta\pi}(UX)_{l,m}\right]^{T},$$

$$B_{l,m}^{T}=\left[1-\frac{\gamma^2\Delta t}{2h}\sqrt{u_{l,m}^2+v_{l,m}^2}-\frac{\Delta t}{4r\Delta\pi\sin\theta_m}(VY)_{l,m}\right]^{T},$$

$$\left.\begin{aligned} C^{T}_{l,m} &= \left[\omega\Delta t\cos\theta_m - \frac{\Delta t}{4r\Delta\pi\sin\theta_m}(UY)_{l,m}\right]^{T}, \\ D^{T}_{l,m} &= \left[-\omega\Delta t\cos\theta_m - \frac{\Delta t}{4r\Delta\pi}(VX)_{l,m}\right]^{T}, \\ P^{t+1}_{l,m} &= R_{l,m}\Delta t - \frac{g\Delta t}{r\Delta\pi}(\zeta_{l,m+1}-\zeta_{l,m-1})^{t+1}, \\ Q^{t+1}_{l,m} &= S_{l,m}\Delta t - \frac{g\Delta t}{r\Delta\pi\sin\theta_m}(\zeta_{l+1,m}-\zeta_{l-1,m})^{t+1}. \end{aligned}\right\} \tag{18}$$

Finally, on the spherical surface, instead of the mixing formula (16) we have

$$\begin{aligned} \left\langle \begin{matrix} u \\ v \end{matrix} \right\rangle^{T+1}_{l,m} &= \left[1-\frac{4A_l\Delta T}{r^2\Delta\pi^2\sin^2\theta_m}(1+\sin^2\theta_m)\right]\left\langle \begin{matrix} u \\ v \end{matrix} \right\rangle^{T}_{l,m} \\ &+\frac{A_l\Delta T}{r^2\Delta\pi^2\sin^2\theta_m}(1+\sin^2\theta_m)\left[\left\langle \begin{matrix} u \\ v \end{matrix} \right\rangle_{l+1,m+1}+\left\langle \begin{matrix} u \\ v \end{matrix} \right\rangle_{l+1,m-1}\right. \\ &\left.+\left\langle \begin{matrix} u \\ v \end{matrix} \right\rangle_{l-1,m+1}+\left\langle \begin{matrix} u \\ v \end{matrix} \right\rangle_{l-1,m-1}\right]^{T}. \end{aligned} \tag{19}$$

6. *Stability*

One of the most important problems in the numerical experiments is the computational stability, which guarantees the numerically solved solutions shall coincide with the analytical ones. Now, after G. Fischer's method (Fischer, 1959) we seek for the computational stability conditions of difference scheme (7) corresponding to the differential equations (6). The wind stress terms R and S included in p and q are constant at a point, and we can neglect these non-homogeneous terms in the simultaneous linear equations (7). Then our equations of motion and continuity become the following homogeneous linear equations with constant coefficients:

$$\left.\begin{aligned} \left(\frac{\partial u}{\partial t}\right)^{t+1} &= \frac{a}{2}(u^{t+2}+u^{t})+\frac{c}{2}(v^{t+2}+v^{t})-g\left(\frac{\partial\zeta}{\partial x}\right)^{t+1}, \\ \left(\frac{\partial v}{\partial t}\right)^{t+1} &= \frac{b}{2}(v^{t+2}+v^{t})+\frac{d}{2}(u^{t+2}+u^{t})-g\left(\frac{\partial\zeta}{\partial y}\right)^{t+1}, \\ \frac{1}{h}\left(\frac{\partial\zeta}{\partial t}\right)^{t+2} &= -\left(\frac{\partial u}{\partial x}\right)^{t+2}-\left(\frac{\partial v}{\partial y}\right)^{t+2}. \end{aligned}\right\} \tag{20}$$

If we expand u, v and ζ as

$$\left.\begin{aligned} u^{t} &= \sum_{l,m} u^{t}_{l,m}e^{i(lx+my)}, \\ v^{t} &= \sum_{l,m} v^{t}_{l,m}e^{i(lx+my)}, \\ \zeta^{t} &= -\sqrt{\frac{h}{g}}\sum_{l,m}\phi^{t}_{l,m}e^{(lx+my)}, \end{aligned}\right\} \tag{21}$$

their central difference forms become

$$\left(\frac{\partial u}{\partial t}\right)^{t+1}=\sum_{l,m}\frac{u_{l,m}^{t+2}-u_{l,m}^{t}}{\Delta t}e^{i(lx+my)}$$

$$\left(\frac{\partial u}{\partial x}\right)^{t+2}=\sum_{l,m}u^{t+2}e^{i(lx+my)}\frac{e^{il\Delta x}-e^{-il\Delta x}}{2\Delta x}=\frac{i}{\Delta x}\sum_{l,m}u_{l,m}^{t+2}e^{i(lx+my)}\sin l\Delta x\,,$$

etc.

Further, putting

$$\left.\begin{aligned}&2\Delta x=2\Delta y=\Delta s\,,\\&\alpha=2\sqrt{gh}\,\frac{\Delta t}{\Delta s}\sin\frac{l\Delta s}{2}\,,\\&\beta=2\sqrt{gh}\,\frac{\Delta t}{\Delta s}\sin\frac{m\Delta s}{2}\,,\end{aligned}\right\}\tag{22}$$

we have from the formulas (20)

$$\left.\begin{aligned}&u^{t+2}-u^{t}=\frac{a\Delta t}{2}(u^{t+2}+u^{t})+\frac{c\Delta t}{2}(v^{t+2}+v^{t})+i\alpha\phi^{t+1}\,,\\&v^{t+2}-v^{t}=\frac{d\Delta t}{2}(u^{t+2}+u^{t})+\frac{b\Delta t}{2}(v^{t+2}+v^{t})+i\beta\phi^{t+1}\,,\\&\phi^{t+3}-\phi^{t+1}=i\alpha u^{t+2}+i\beta v^{t+2}\,,\end{aligned}\right\}\tag{23}$$

where the summation sign $\sum_{l,m}$ is omitted.

If we neglect the second order terms, the above equations (23) are rewritten as follows:

$$\left.\begin{aligned}&u^{t+2}=a'u^{t}+c'v^{t}+i\alpha'\phi^{t+1}\,,\\&v^{t+2}=-d'u^{t}+b'v^{t}+i\beta'\phi^{t+1}\,,\\&-i\alpha u^{t+2}-i\beta v^{t+2}+\phi^{t+3}=\phi^{t+1}\,,\end{aligned}\right\}\tag{24}$$

where

$$\left.\begin{aligned}&a'=1+a\Delta t\,,\\&b'=1+b\Delta t\,,\\&c'=c\Delta t\,,\\&d'=-d\Delta t\,,\\&\alpha'=\alpha\left(1+\frac{a\Delta t}{2}\right)+\beta\frac{c\Delta t}{2}\,,\\&\beta'=\beta\left(1+\frac{b\Delta t}{2}\right)+\alpha\frac{d\Delta t}{2}\,.\end{aligned}\right\}\tag{25}$$

Using the vector $\Phi^{t}(u^{t}, v^{t}, \phi^{t+1})$, the equations (24) are rewritten

$$\begin{pmatrix} 1 & 0 & 0 \\ 0 & 1 & 0 \\ -i\alpha & -i\beta & 1 \end{pmatrix} \Phi^{t+2} = \begin{pmatrix} a' & c' & i\alpha' \\ -d' & b' & i\beta' \\ 0 & 0 & 1 \end{pmatrix} \Phi^{t},$$

or

$$\Phi^{t+2} = G\Phi^{t}, \tag{26}$$

with

$$G = \begin{pmatrix} a' & c' & i\alpha' \\ -d' & b' & i\beta' \\ i\alpha a' - i\beta d' & i\alpha c' + i\beta b' & -\alpha\alpha' - \beta\beta' + 1 \end{pmatrix}. \tag{27}$$

The von Neumann condition (RICHTMYER, 1957) or the mathematical condition of convergence for Φ in the equation (26) is

$$|\lambda_i| \leqq 1 + O(\Delta t), \qquad i = 1, 2, 3, \tag{28}$$

where λ_i are the eigenvalues of G. Putting

$$\left.\begin{aligned} &\alpha\alpha' + \beta\beta' = (\alpha^2 + \beta^2)\xi, \\ &\alpha\alpha'(a' - b') + c'\alpha\beta' - d'\alpha'\beta = \eta, \\ &\xi = 1 + \frac{b\Delta t}{2} + \left[\alpha^2\left(\frac{a\Delta t}{2} - \frac{b\Delta t}{2}\right) + \alpha\beta\left(\frac{c\Delta t}{2} + \frac{d\Delta t}{2}\right)\right] \Big/ (\alpha^2 + \beta^2) \leqq 1 + \frac{5}{2}|b|\Delta t, \\ &\eta = \alpha^2(a\Delta t - b\Delta t) + \alpha\beta(c\Delta t + d\Delta t) < 4\alpha^2|b|\Delta t, \end{aligned}\right\} \tag{29}$$

our secular equation to decide the eigenvalue λ is

$$(a' - \lambda)\{(b' - \lambda)(1 - \lambda) + (\alpha^2 + \beta^2)\xi\lambda\} = \eta\lambda. \tag{30}$$

Neglecting the right side which is the smallest in the equation (30), we have the first eigenvalue

$$\lambda_1 = a' = 1 + a\Delta t, \tag{31}$$

which surely satisfies the von Neumann condition (28). The second and third eigenvalues are

$$\lambda_{2,3} = 1 - \frac{1}{2}\chi' \pm \frac{1}{2}\sqrt{\chi'^2 - 4\chi},$$

where

$$\begin{aligned} &\chi = (\alpha^2 + \beta^2)\xi, \\ &\chi' = (\alpha^2 + \beta^2)\xi - b\Delta t. \end{aligned}$$

If

$$\chi'^2 \ll 4\chi \tag{32}$$

we have

$$\lambda_{2,3}=1-\frac{1}{2}\chi'\pm i\sqrt{\chi}\ ,$$

and the absolute value is

$$|\lambda_{2,3}|\leqq\sqrt{1-\chi'+\chi}=\sqrt{1+b\Delta t}\ , \tag{34}$$

which also satisfies the von Neumann condition.

Consequently our necessary condition for the computational stability is the formula (32), or making use of $0<\chi$, it becomes

$$\chi<4\left(1+\frac{b\Delta t}{2}\right),$$

which is, in the n-dimensional plane, equivalent to

$$n\cdot 4gh\left(\frac{\Delta t}{\Delta s}\right)^2\xi<4\left(1+\frac{b\Delta t}{2}\right). \tag{34}$$

According to the definitions mentioned in Section 1, in the case of linear equations we have

$a=b$,
$c=-d$,
$\xi=1+\frac{b\Delta t}{2}$,
$\eta=0$.

Then, in the linear case, from the equation (30) without any approximations the condition (34) becomes

$$\Delta t<\frac{\Delta s}{\sqrt{n\cdot gh}}\ , \tag{35}$$

which quite coincides with that in the linear equations without both frictional and Coriolis' terms. This means, if we use the difference schemes (7) or (20) instead of the differential equations (6), the computational stability is not affected at all by both frictional and Coriolis' terms.

In the non-linear case, substituting ξ of (29) in (34) we have

$$n\cdot gh\left(\frac{\Delta t}{\Delta s}\right)^2<1-3|b|\Delta t\ ,$$

or

$$\Delta t\leqq\Delta\tau-\frac{3}{2}|b|\Delta\tau^2\ , \tag{36}$$

where

$$\Delta\tau=\frac{\Delta s}{\sqrt{ngh}}\ . \tag{37}$$

Therefore due to the frictional and non-linear terms the time interval of the non-linear case, Δt, must be smaller than the corresponding interval $\Delta\tau$ of the linear case. In the present case the least value of Δs is 10^7 as mentioned in Section 3, and $\Delta\tau$ has a value $1.5\cdot10^3$ sec. On the other hand b is estimated at 10^{-5} as stated in Section 3. Therefore, the time interval Δt in (36) is nearly equal to $\Delta\tau$. In the practical computations, to keep enough stability we take $6\cdot10^2$ for Δt, and $3.6\cdot10^3$ for ΔT.

Of course this condition is the necessary one for the mathematical stability. If a and b are always negative as in the case of linear theory, all the eigenvalues λ_i are smaller than the unity, and the computational stability is also satisfied. If $F<-\frac{\partial u}{\partial x}$ or $F<-\frac{\partial v}{\partial y}$ in the non-linear, however, a or b become positive and some eigenvalues become larger than the unity. In this case the von Neumann condition is surely satisfied, still it is not clear either our solutions keep the stability or not after the infinitely repeated computations. In tidal currents running through the narrow straits the field acceleration is sometimes stronger than the frictional resistance. In this case, to keep the balance the surface elevation becomes higher toward the downstream. We can see such phenomena for only a few hours and it was already shown that the above difference scheme is stable in non-steady tidal currents (J. M. A. and Forth Dist. Port Const. Bureau, 1965).

It was also tested for a few days that our scheme is stable in tidal problems on the spherical surface (Ueno, 1964). In this paper the non-linear numerical computations are first tried on the spherical surface for about 70 days, and the stability is still hold.

7. Convergency

In addition to the stability, we have another problem, the convergency. At the beginning of computations we could not foresee whether current velocities and surface elevations tend to finite values or increase infinitely. It will be also difficult to estimate how many hours or days will be necessary to obtain appropriate results. The source of this trouble lies in the difference scheme for equations of motion. If our scheme is not proper to conserve the total energy in our computation system, computed results will gradually reduce to zero or diverge toward infinity. On the other hand, in the case of properly posed scheme, they tend to definite values after some computational execution time, when the second and third law of Newton, the balance of forces and angular moments,

must kept as stated in Section 12.

Now let us examine the passage of computed values with the running time. Behaviors of current velocities and elevations at several selected stations corresponding to the wind system of January are shown in Figure 6. This figure

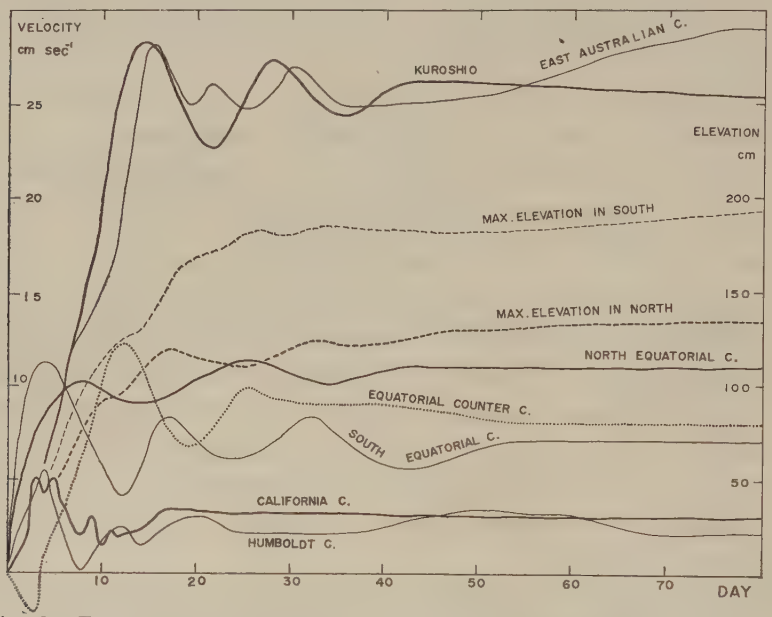

Fig. 6. The behaviors of elevations and current velocities at the selected stations from the initial state until the steady state (January).

shows that the velocity of the Kuroshio, for example, vibrates with the 14-day period at the early stage, and after 42 days the velocity surely tends to a finite value 26 cm·sec^{-1}. In the same way the maximum elevation in the Northern Hemisphere, appearing on the just right side of the Kuroshio tend to 130 cm after 42 days. We can see from Figure 6 that currents and elevations in the Northern Hemisphere converge more rapidly than that in the Southern Hemisphere, because of the difference of area.

8. The wind system

The wind system is the most important factor in this experiment. The wind directions are read at 5-degree grid points from the wind stream-line charts in МОРСКОЙ АТЛАС ТОМ II (1953). The wind speed is assumed to be uniform

along the same latitude. If we use the wind-speed patterns in the charts, computed patterns of currents and elevations become very irregular. The wind stress ($\rho_a\gamma^2|W|W$) charts given by these assumptions for January and July are shown in Figures 7 and 8.

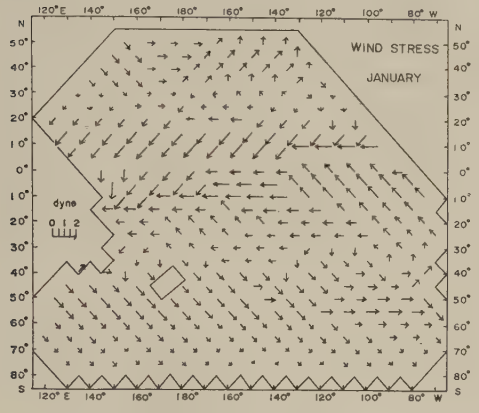

Fig. 7. The designed wind stress ($\rho_a\gamma^2|W|W$) chart (January).

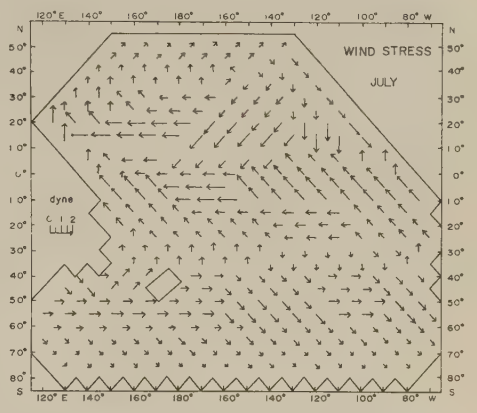

Fig. 8. The designed wind stress ($\rho_a\gamma^2|W|W$) chart (July).

According to the chart for January the wind system on the Northern Hemisphere is under the influence of two atmospheric high pressures, the North Pacific high centered at 30°N and 130°W and the Siberian high. On the other hand, in July the Northern Hemisphere is entirely covered by the North Pacific high centered at 40°N and 150°W. In January the Southern Pacific high centered at 35°S and 100°W covers the Southern Hemisphere. In July the Southern Pacific high has its center at 30°S and 100°W, and the Australian high covers some area of the Hemisphere.

The Equatorial Calm Belt lies along the 5°N zone in January and along the 10°N zone in July. Such a wind system near the equator, however, is not suitable for the actual case, especially for the western part of the equator. The Northeast Trades blow into the Southern Hemisphere through the calm belt, which should lies between the Northeast and the Southeast Trades. For convenience the author defines the Northern Hemisphere to be the area north of the calm belt and the Southern Hemisphere to be the area south of it. Under this definition sums of forces and angular moments on each Hemisphere are computed in January and July as stated in the last section. For this purpose the calm belt offers much convenience to us, however, trade winds blowing through the

calm belt are not proper for the actual wind system.

9. *Mixing coefficient*

The value of mixing coefficient A_l is given from the mass transport of the Kuroshio. Current velocity components u and v at any point (i, j) with a co-latitude θ_j represent the mean values over the section $r\Delta\pi \sin\theta_j$ along the parallel and the section $r\Delta\pi$ along the meridian, respectively (Fig. 5). The mass transport then becomes $h\sqrt{(ur\Delta\pi \sin\theta_j)^2+(vr\Delta\pi)^2}$. In this way the mass transport of the Kuroshio in January can be given as a function of A_l. Table 1 shows mass transport values at the point in 25°N, 130°E, where the speed of the Kuroshio becomes strongest, and from these results the author takes A_l to be $5\cdot10^9$ in our computations.

Table 1. The mass transport of the Kuroshio in January corresponding to various values of A_l.

A_l	Mass transport
0	$92 \cdot 10^{12}$
10^9	$92 \cdot 10^{12}$
$5 \cdot 10^9$	$41.6 \cdot 12^{12}$
$5 \cdot 10^9$	$42.5 \cdot 10^{12}$ (July)
$3 \cdot 10^{11}$	$26 \cdot 10^{12}$

10. *Patterns of computed currents and elevations*

The current and elevation charts obtained after about 2000 hours run are shown in Figures 9–12. Their patterns along the center axis are shown in Figures 16 and 17.

In the Northern Hemisphere, currents and elevations rapidly converge to finite values. They take definite patterns after about 40 days as mentioned in Section 7. The patterns in July are almost the same as those of January moved to north by the 5 degrees. In January the Equatorial Counter Current runs along the parallel of 5°N, and its velocity is stronger in the eastern area. In July it runs along the parallel of 10°N, its velocity is stronger than that in January, and in the western area we can sea a stronge source of the counter current. In both January and July the zone of the Equatorial Counter Current

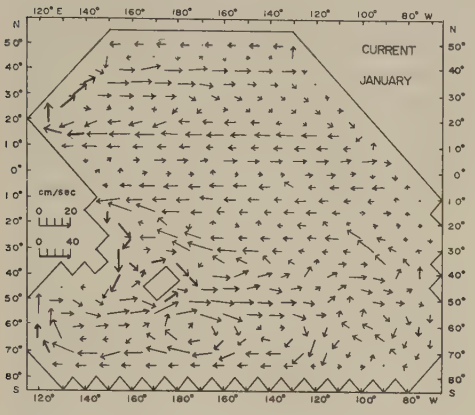

Fig. 9. The pattern of the computed current velocity. All the velocities under 45°S should be read after twice their vectors in length (January).

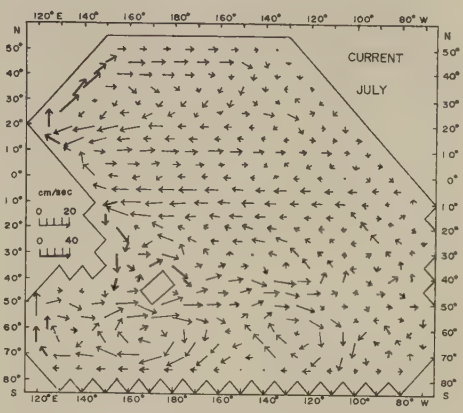

Fig. 10. The pattern of the computed current velocity. All the velocities under 45°S should be read after twice their vectors in length (July).

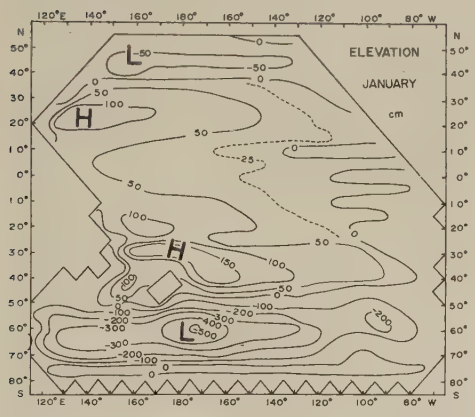

Fig. 11. The pattern of the computed surface elevation (January).

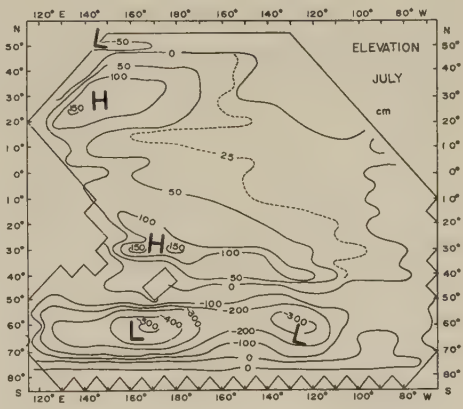

Fig. 12. The pattern of the computed surface elevation (July).

coincides with the Equatorial Calm Belt. The North Equatorial Current in January is stronger in velocity and narrower in width than those in July. On the other hand the Kuroshio does not change its speed through the two seasons. In January the Alaska Current runs along the northern boundary to meet the Kuroshio.

As to the Southern Hemisphere, because of its large area, the patterns of currents and elevations do not tend so rapidly to definite forms as in the case of

Northern Hemisphere. Especially, at the early stage of computations, two vortexes are present in the east and west area of the Antarctic Ocean. Gradually approaching to each other, they grow into a great whirl at the southern part off New Zealand. The current speeds to the South of 45°S are very strong and halves of them are shown in Figures 9 and 10. As shown in Figure 6, or from the reckoning for the acceleration term at each grid point, the velocities or elevations around this eddy still fluctuate after about 2000 hours run. Now we have very interesting and important questions. Why do such the vortexes appear only in the Southern Hemisphere? What progress does this whirl pass if we further continue the computation? How do closed east and west boundaries affect the currents in the Southern Hemisphere? Our computer, however, cannot afford to solve these problems. We have to do with these unsatisfactory results in the Southern Hemisphere. For example, the East Australian Current is too strong and the Humboldt Current is too weak which runs far off South America. In areas except above-mentioned parts, currents and elevations surely reach the steady states, and we have reasonable results on the whole as shown in Section 12.

Turning our attention to the elevation patterns, high elevation parts (about 1.5 m) in the western area of both Hemispheres, are noticeable. On the west of these high elevation parts strong currents, the Kuroshio and the East Australian Current, are running. In both Hemispheres the current systems generally form circulations around high elevation parts. The surface is sloping down from the highest part to the east side in both Hemispheres. We also see a trough running along the low latitude between these high elevation parts in both Hemispheres. Speaking more exactly, as shown in Figures 16 and 17, the bottom of trough runs along the parallel of 10°N in January and 15°N in July, making a surface sloping down from west to east. The belt between this bottom and the equator coincides with the Equatorial Calm Belt, where the Equatorial Counter Current are running like a river from a high sea-level part to a low sea-level part. This belt, from the equator to the sea-level trough, also makes a surface sloping down from south to north, and in connection with the velocity of counter current, the gradient in July is stronger than that in January.

11. Comparisons between the computed and observed elevations

Comparing the computed current charts with the observed surface current ones we can verify our computed current patterns to some extent. As to the elevations, corresponding to the observed current charts, we have tidal observa-

Table 2. List of tidal station, the name of month when the maximum or the minimum value of the observed monthly mean sea-level appears, and the amplitude in cm (the difference between the maximum and the minimum value). The minus amplitude means that the maximum value appears in Jan.-Mar. (JMA. IUGG and Hydrographer of Navy). The station numbers are corresponding to those of Figure 14.

	Station	Lat.	Long.	Amp.	Maximum	Minimum
		the east side				
1	Sitka	57°03′ N	135°20′ W	−40	Jan. Feb.	June July
2	Ketchikan	55 20 N	131 38 W	−42	〃 〃	〃 〃
3	Queen Charlotte	53 15 N	132 04 W	−27	〃 〃	May June July
4	Alert Bay	50 35 N	126 56 W	−33	〃 〃	〃 〃 〃
5	Tofino	49 09 N	125 55 W	−37	〃 〃	May June
6	Neah Bay	48 22 N	124 37 W			
7	Seattle	47 36 N	122 20 W		semi-annual type	
8	Crescent	41 45 N	124 12 W			
9	San Francisco	37 48 N	122 28 W			
10	Avila	35 10 N	120 44 W	15	Aug. Sept.	Mar. Apr.
11	Los Angeles	33 43 N	118 16 W	16	Sept. Oct.	Apr. May
12	La Jolla	32 52 N	117 15 W	17	Aug. Sept. Oct.	〃 〃
13	San Diego	32 43 N	117 10 W	17	Sept. Oct.	〃 〃
14	Ensenada	31 51 N	116 38 W	17	〃 〃	〃 〃
15	Mazatlan	23 12 N	106 25 W	28	Aug. Sept.	Mar. Apr.
16	Manzanillo	19 03 N	104 20 W	13	〃 〃	〃 〃
17	Acapulco	16 50 N	99 55 W	15	〃 〃	〃 〃
18	Salina Cruz	16 10 N	95 12 W	15	〃 〃	〃 〃
19	La Union	13 20 N	87 49 W	0		
20	Puntarenas	9 58 N	84 50 W		semi-annual type	
21	Buenaventura	3 54 N	77 06 W			
22	Talara	4 37 S	81 17 W	−15	Dec. Jan.	Aug. Sept. Oct.
23	Chimbote	9 05 S	78 38 W	−15	Jan. Feb.	〃 〃 〃
24	Callao	12 03 S	77 09 W	−18	〃 〃	〃 〃 〃
25	San Juan	15 22 S	75 12 W	−15	〃 〃	〃 〃 〃
26	Matarani	17 00 S	72 07 W	−15	〃 〃	Aug. Sept.
27	Antofagasta	23 39 S	70 25 W	−10	〃 〃	〃 〃
28	Caldera	27 04 S	70 50 W	−15	〃 〃	〃 〃
29	Valparaiso	33 02 S	71 38 W		semi-annual type	
30	Talcahuano	36 41 S	73 06 W			
31	Puerto Montt	41 29 S	72 58 W	0		
		the center axis				
32	Attu	52 50 N	173 12 W			
33	Adak	51 52 N	176 39 W			
34	Midway	28 13 N	177 22 W			
35	Honolulu	21 18 N	157 52 W			
36	Johnston	16 45 N	169 31 W			
37	Wake	19 17 N	166 37 W			

	Station	Lat.	Long.	Amp.	Maximum	Minimum
38	Apra	13°26′ N	144°39′ E			
39	Moen	7 27 N	151 51 E			
40	Eniwetok	11 22 N	162 21 E	semi-annual		
41	Kwajalein	8 44 N	167 44 E	irregular	mixed type	
42	Palmyra	5 52 N	162 06 W	negligible		
43	Fanning	3 54 N	159 24 W			
44	Christmas	1 57 N	157 28 W			
45	Jarvis	0 21 S	160 01 W			
46	Ocean	0 53 S	169 35 E			
47	Arorae	2 37 S	176 50 E			
48	Canton	2 48 S	171 43 W			
49	Takaroa	14 25 S	145 00 W			
50	Matavai	17 31 S	149 31 W			
51	Rurutu	22 27 S	151 20 W	−17	Jan. Feb.	Oct. Nov.
52	Easter	27 09 S	109 29 W	−9	Mar. Apr.	Sept, Oct.

the west side

53	Petropavlovsk	53°01′ N	158°29′ E	−22	Jan. Feb.	Aug. Sept.
54	Hanasaki	43 17 N	145 35 E	semi-annual type		
55	Kushiro	42 58 N	144 22 E			
56	Hachinohe	40 32 N	141 31 E	26	Aug. Sept.	Mar. Apr.
57	Miyako	39 38 N	141 58 E	25	〃 〃	〃 〃
58	Ayukawa	38 18 N	141 31 E	23	〃 〃	〃 〃
59	Onahama	36 56 N	140 55 E	23	〃 〃	〃 〃
60	Choshi	35 44 N	140 50 E	23	Sept. Oct.	〃 〃
61	Mera	34 55 N	139 50 E	19	〃 〃	〃 〃
62	Kushimoto	33 28 N	135 46 E	24	Aug. Sept.	〃 〃
63	Tosashimizu	32 47 N	132 58 E	26	〃 〃	Feb. Mar.
64	Aburatsu	31 35 N	131 25 E	26	〃 〃	〃 〃
65	Naze	28 23 N	129 30 E	32	Sept. Oct.	〃 〃
66	Legaspi	13 09 N	123 45 E	12	July Aug.	Dec. Jan.
67	Tacloban	11 15 N	125 00 E	15	June July	〃 〃
68	Davao	7 05 N	125 38 E	15	〃 〃	〃 〃
69	Bicholi	0 35 N	128 34 E	0		
70	Demta Baai	2 21 S	140 14 E	0		
71	Dreger	6 39 S	147 53 E	0		
72	Cairns	16 55 S	145 43 E	−24	Mar. Apr.	July Aug. Sept.
73	Townsville	19 20 S	146 50 E	−30	〃 〃	Sept. Oct.
74	Gladstone	23 53 S	151 12 E	−22	〃 〃	〃 〃
75	Coff's Harbour	30 20 S	153 00 E	−22	Mar. Apr. May	Oct. Nov.
76	Lord Howe	31 31 S	159 07 E			
77	Camp Cove	33 53 S	151 15 E			
78	Port Kembla	34 28 S	150 55 E			
79	Eden	37 05 S	149 59 E	semi-annual type		
80	Williamstown	37 52 S	144 58 E			
81	Hobart	42 50 S	147 19 E			
82	Maatsuyker	43 38 S	146 22 E			
83	Cape Sorrell	42 13 S	145 13 E			

tions along coasts or at solitary islands, where there are two important factors; one is the pattern of seasonal variation at any tidal station, another is the distribution of many years' mean sea-level measured by the leveling. The author has a few data for the latter, and discussions will be given along the coast of Japan and the United States by using these data. Referring to the former, there are four main patterns; annual, semi-annual, constant and irregular one. Our numerical experiments are made for January and July, and the annual amplitudes are estimated from these results. The amplitude distributions obtained from the computed elevation charts in July and January (Figs. 11 and 12) are shown in Figure 13. The difference between

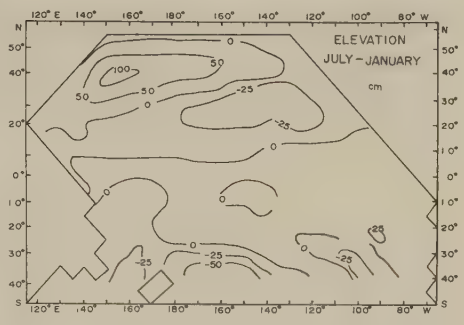

Fig. 13. The computed annual amplitude, or the difference between the computed elevation in July and January.

Fig. 14. The tidal station and the type of seasonal variation of mean sea-level. See the explanation for Table 2.

the maximum and minimum value of the observed monthly mean sea-level at the main tidal stations in the Pacific Ocean are shown in Figure 14 or Table 2, in which the data along the coast of Japan are for five years from 1960 to 1964 (JMA, 1965) and the others are for the year 1957 or 1958 (IUGG, 1959, 1963).

Let us examine the east side as shown in Figure 15. According to AVERS (1928) (the author has a few levelling data in U. S. A. which are rewritten from the work of OGURA (1934), the mean sea-level along the Pacific coast of the United States makes a surface sloping rising up from south to north. Heights of the mean sea-level at San Francisco and Seattle are 4 cm and 26 cm higher than that of San Diego. On the contrary, computed surfaces are sloping down to the north from 20°N. Observed seasonal variation of the sea-level has the following tendencies. Along the coasts of the United States and Mexico the maximum monthly mean sea-level appears in August and September, and the minimum in March and April. On the other hand, along the Bay of Alaska and the coast from the equator to 30°S, the maximum appears in January and the minimum in July and August. Among these areas we have the transitive zones in which the seasonal variations are of the semi-annual, constant or irregular type. It is very interesting that these transitive zones surely coincide with the limits of currents, and that as mentioned below the same phenomena are seen along the west side of the Pacific Ocean. Observed seasonal variations of sea-level contain the effects of the atmospheric pressure. Therefore, if we want to examine more correctly the relations between the seasonal variation of the sea-level and the general circulation, we should subtract the effects of the atmospheric pressure on the sea-level elevation from the above seasonal variations. As shown in Figure 15, the computed

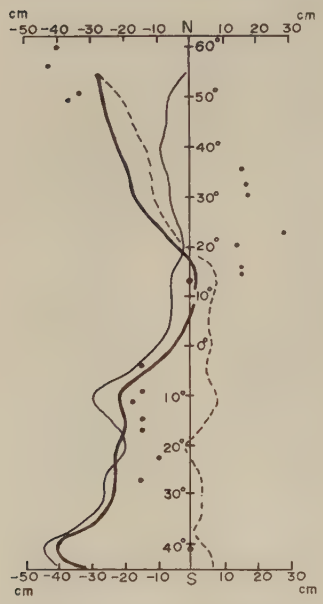

Fig. 15. Latitudinal profile of sea-level elevation along the east side of the Pacific Ocean.
broad line; computed value for July
slim line; computed value for January
dashed line; value of (July-January)
spots; observed amplitude of seasonal variation (see Table 2)

seasonal variations are also much different from the observed ones. Computed results are chiefly decided by the designed wind system. If we choose the pattern or location of the North Pacific high pressure more exactly, the results will more close to the observations.

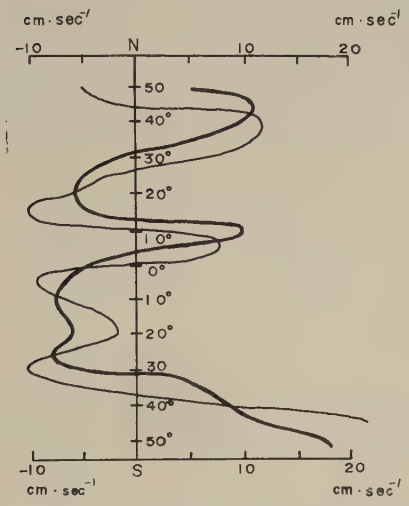

Fig. 16. Latitudinal profile of computed current velocity along the center axis of the Pacific Ocean. See explanation for Fig. 15.

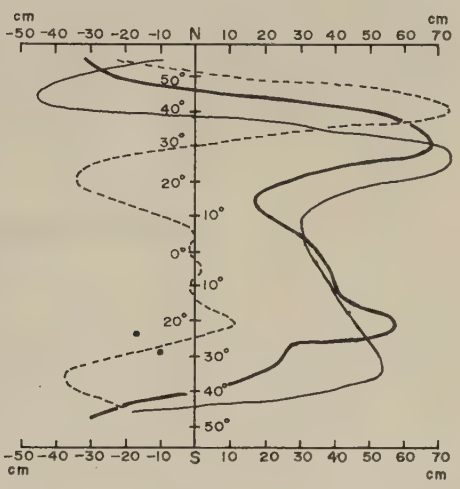

Fig. 17. Latitudinal profile of computed sea-level elevation along the center axis of the Pacific Ocean. See explanation for Fig. 15.

Figures 16 and 17 show the latitudinal dependence of the computed currents and elevations along the center axis starting from Adak of the Aleutian Islands, passing through Midway, Christmas, and Tahiti, finally ending at the Easter Islands. As mentioned before, the computed Equatorial Counter Current runs along the calm belt; 10°N in July and 5°N in January. This belt makes the surface sloping down to north, and the gradient is stronger in July due to its strong current. The elevation becomes lower in July and higher in January near the latitude 15°N along which the trough of the sea-level runs in July. The seasonal variations of the sea-level are small in the belt from the latitude 10°N to the equator (cf. Fig. 17). On the other hand we have several tidal stations at isolated islands. The observation shows that the seasonal variations are small or irregular on the whole and that the definite type is hardly given. If there are enough tidal data to analyse the seasonal variations at these islands, we may have very interesting results in connection with the Equatorial

Counter Current.

As to the patterns in the west side, we have very similar results to that of the east side as mentioned before. According to the tidal observations along the coasts of Japan and the Philippines the monthly mean sea-level is high in September and low in March and reverse along the northern part of Australian coast or at the Kamchatka Peninsula. Among these areas there are zones showing semi-annual, constant or irregular types. The computed results in Figure 18 also show the above facts. Further, Figure 18 shows that the computed surface on the west side of the Kuroshio is sloping down from 25°N to 40°N in both

Fig. 18. Latitudinal profile of computed sea-level elevation along the west side of the Pacific Ocean. See explanation for Fig. 15.

July and January. These facts surely coincide with the observations. Table 3 shows the height of mean sea-level along the coast of Japan in September and March for the five years from 1960 to 1964 (JMA, 1965). These data are measured by the leveling from T. P. (the standard mean sea-level of Tokyo Bay). On the whole we have better computed results in the west side than in the east, which is chiefly because the current and elevation patterns in the west side are less

Table 3. Mean sea-level along the coast of Japan above T.P. (the standard mean sea-level of Tokyo Bay) (the mean value from 1960 to 1964, JMA, 1965)

Station	Lat. N	Long. E	September (cm)	March (cm)
Hanasaki	43°17′	145°35′	18.9	8.8
Kushiro	42 58	144 22	16.0	4.3
Hachinohe	40 32	141 31	34.8	9.8
Miyako	39 38	141 58	30.9	5.8
Ayukawa	38 18	141 31	24.9	3.3
Onahama	36 56	140 55	20.6	−1.5
Choshi	35 44	140 50	4.8	−17.8
Mera	34 55	139 50	5.5	−11.5
Kushimoto	33 28	135 46	−4.0	−28.3
Tosashimizu	32 47	132 58	0.0	−25.8
Aburatsu	31 35	131 25	20.0	−5.6

affected by the wind stress as compared with the case of the east side. The above feature is shown by Table 4, in which the ratio of wind stress term to others in the Kuroshio is compared with that in the California Current.

12. *Balance of forces and angular moments*

Provided that solutions of u, v and ζ reach the steady states at each velocity point (l, m), they must satisfy the following equations (see equation (1) and (2)):

$$\left.\begin{aligned} fv-g\frac{\partial\zeta}{\partial x}+R-Fu-\left(u\frac{\partial u}{\partial x}+v\frac{\partial u}{\partial y}\right)+A_l\Delta_1 u=0\,,\\ -fu-g\frac{\partial\zeta}{\partial y}+S-Fv-\left(u\frac{\partial v}{\partial x}+v\frac{\partial v}{\partial y}\right)+A_l\Delta_1 v=0\,,\end{aligned}\right\} \tag{38}$$

in which the first and second equation corresponds to x and y component of the force acting on a unit mass of sea water at each grid point. Further, each component consists of several terms as shown in the formulas (38); Coriolis', surface gradient, wind stress, bottom friction, non-linear and mixing terms. To simplify the discussions, the sign $X^k_{l,m}$ and $Y^k_{l,m}$ are used for the x and y component of k-th term acting on the grid point (l, m). Then, the formulas (38) take the next forms.

$$\left.\begin{aligned} \sum_k X^k_{l,m}=0\,,\\ \sum_k Y^k_{l,m}=0.\end{aligned}\right\} \tag{39}$$

On the other hand, as illustrated in Figure 5, a grid point (l, m) represents a square area $(r\Delta\pi)^2 \sin\theta_m$. All the current and elevation points are alternately arranged as shown in Figure 3, so the effective mass $E_{l,m}$ represented by a mesh point (l,m) takes the following value:

$$E_{l,m}=\frac{1}{2}\rho_w h(r\Delta\pi)^2 \sin\theta_m\,, \tag{40}$$

where ρ_w is the density of sea water.

Then the components of resultant force of k-th term acting on the whole computed area will become

$$\left.\begin{aligned} X^k &= \sum_{l,m} X^k_{l,m} E_{l,m}\,, \\ Y^k &= \sum_{l,m} Y^k_{l,m} E_{l,m}\,. \end{aligned}\right\} \tag{41}$$

Under these definitions we have the following equations:

$$\left.\begin{aligned} \sum_k X^k &= 0\,, \\ \sum_k Y^k &= 0\,. \end{aligned}\right\} \tag{42}$$

This corresponds to the second law of Newton from which we know the mechanism of balance among the resultant forces of all the terms at the center of geometrical gravity G for our computed area.

To examine the Newtonian third law, the conservation of angular moment, we define the center of geometrical gravity G for our computed area as follows:

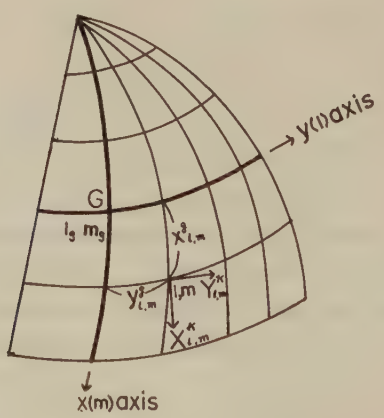

Fig. 19. The center of geometrical gravity G and the angular moment of k-th term $(X^k_{l,m}, Y^k_{l,m})$ at a point (l, m) referring to G.

In Figure 19, let l_g and m_g be the location of the center of gravity G along y and x axis respectively. Further, let $y^g_{l,m}$ and $x^g_{l,m}$ be the distance from any grid point (l, m) to the parallel and the meridian respectively, both passing through the grid point (l_g, m_g). The values for $x^g_{l,m}$ and $y^g_{l,m}$ are

$$\left.\begin{aligned} x^g_{l,m} &= r\frac{\Delta\pi}{2}(m-m_g), \\ y^g_{l,m} &= r\frac{\Delta\pi}{2}(l-l_g)\sin\theta_m . \end{aligned}\right\} \tag{43}$$

Then, the location of $G\,(l_g, m_g)$ will be given by the next relations.

$$\left.\begin{aligned} \sum_{l,m} E_{l,m}x^g_{l,m} &= 0 , \\ \sum_{l,m} E_{l,m}y^g_{l,m} &= 0 , \end{aligned}\right\} \tag{44}$$

and the angular moment of k-th term referred to G will be given as follows:

$$M_g{}^k = \sum_{l,m}[Y^k_{l,m}x^g_{l,m} - X^k_{l,m}y^g_{l,m}]\,E_{l,m} , \tag{45}$$

where the counter clockwise direction is taken to be positive. Then the conservation of angular moment is written in the next form,

$$\sum_k M_g{}^k = 0 . \tag{46}$$

From this formula we know the mechanism of balance among the angular moments referred to the center of gravity G.

Instead of G, we consider the center of k-th term $G_0{}^k$, whose location is $(l_0{}^k, m_0{}^k)$. In Figure 19, we put $G_0{}^k$ in place of G, and let $x^k_{l,m}$ and $y^k_{l,m}$ be the component of the distance from any grid point (l, m) to $G_0{}^k$.
Then they are

$$\left.\begin{aligned} x^k_{l,m} &= r\frac{\Delta\pi}{2}(m-m_0{}^k), \\ y^k_{l,m} &= r\frac{\Delta\pi}{2}(l-l_0{}^k)\sin\theta_m , \end{aligned}\right\} \tag{47}$$

$G_0{}^k$ is the point around which the total angular moment $M_0{}^k$ of k-th term becomes null or the system of forces belong to k-term makes a couple of forces. So we can define $l_0{}^k$ and $m_0{}^k$ by the next relations:

$$\left.\begin{aligned} \Big|\sum_{m_0<m}\sum_l E^k_{l,m}Y^k_{l,m}x^k_{l,m}\Big| &= \Big|\sum_{m<m_0}\sum_l E^k_{l,m}Y^k_{l,m}x^k_{l,m}\Big| , \\ \Big|\sum_{l_0<l}\sum_m E^k_{l,m}X^k_{l,m}y^k_{l,m}\Big| &= \Big|\sum_{l<l_0}\sum_m E^k_{l,m}X^k_{l,m}y^k_{l,m}\Big| , \end{aligned}\right\} \tag{48}$$

and the amount of the couple becomes

$$M_0^k=\sum_{l,m}[Y_{l,m}^k x_{l,m}^k-X_{l,m}^k y_{l,m}^k]\,E_{l,m}\,. \tag{49}$$

Then we may say that the total effect of k-th term on the general circulation consists of the force $(X^k,\ Y^k)$ acting at G_0^k and of the angular moment M_0^k about G_0^k. Thus we can regard M_0^k as the proper moment to the k-th term.

Under the above definitions, first we examine the value of components for each term $(X_{l,m}^k,\ Y_{l,m}^k)$ in main currents, where the formula (39) must be satisfied. Table 4 shows these values reckoned from the computed distributions of u, v and ζ obtained after 2,000 hours run from the epoch, in which the definitions for each term are stated in the left side of relations (38). Figure 20, based on Table 4, shows the diagrams illustrating the dynamical structure of main currents. These facts denote that sums $\sum_k X_{l,m}^k$, $\sum_k Y_{l,m}^k$, or the accelerations, are still not zero, but they are less than 10% of $\sum_k|X_{l,m}^k|$ or $\sum_k|Y_{l,m}^k|$. Therefore, it may be said that our numerical solutions for u, v and ζ nearly reach the steady state and

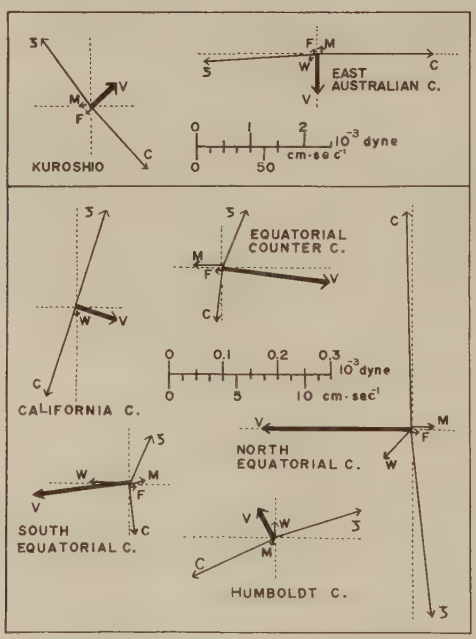

Fig. 20. The dynamical structure of main currents in January (see Table 4).
C, Coriolis ; ζ, surface gradient
W, wind stress; F, bottom friction
M, mixing ; V, current velocity

Table 4 (a). The x (south) and y (east) component of each term (k) acting on a unit mass of sea water in the main current in January (C. G. S. unit, multiplied by 10^6 except velocity). Velocity components are also shown.

Current	Kuroshio		East Australian		North Equatorial		Equatorial Counter		South Equatorial		California		Humboldt	
Location	25° N 130° E		30° S 155° E		15° N 160° W		5° N 150° W		5° S 140° W		25° N 110° W		30° S 75° W	
Component / Term (k)	$X^k_{l,m}$	$Y^k_{l,m}$	$X^k_{l,m}$	$Y^k_{l,m}$	$X^k_{l,m}$	$Y^k_{l,m}$	$X^k_{l,m}$	$Y^k_{l,m}$	$X^k_{l,m}$	$Y^k_{l,m}$	$X^k_{l,m}$	$Y^k_{l,m}$	$X^k_{l,m}$	$Y^k_{l,m}$
Coriolis	1192	1056	−1	2138	−408	−13	103	−9	94	11	168	−57	75	−162
Surface gradient	−1279	−944	134	−2132	353	38	−103	47	−90	43	−184	−58	−49	165
Wind stress	9	−9	20	−20	57	−57	0	0	0	−80	13	0	−29	0
Bottom friction	58	−65	−112	0	0	15	−1	−9	−1	9	0	−1	1	0
Mixing	65	−127	−177	2	2	40	−1	−59	−8	37	3	−6	12	−2
Non-linear	−1	−3	0	−2	0	0	0	0	0	0	0	0	0	0
Sum ($\sum_k$)	1324 −1280	1056 −1148	154 −290	2140 −2154	412 −408	30 −70	103 −105	47 −77	94 −99	100 −80	184 −184	58 −64	88 −78	165 −164
Velocity	−17	19	29	0	0	−11	1	8	1	−7	1	3	−2	−1

Table 4 (b). The x (south) and y (east) component of each term (k) acting on a unit mass of sea water in the main current in July (C. G. S. unit, multiplied by 10^6 except velocity). Velocity components are also shown.

Current	Kuroshio		East Australian		North Equatorial		Equatorial Counter		South Equatorial		California		Humboldt	
Location	25° N 130° E		30° S 155° E		20° N 175° W		10° N 165° W		10° S 145° W		30° N 115° W		30° S 75° W	
Component / Term (k)	$X^k_{l,m}$	$Y^k_{l,m}$	$X^k_{l,m}$	$Y^k_{l,m}$	$X^k_{l,m}$	$Y^k_{l,m}$	$X^k_{l,m}$	$Y^k_{l,m}$	$X^k_{l,m}$	$Y^k_{l,m}$	$X^k_{l,m}$	$Y^k_{l,m}$	$X^k_{l,m}$	$Y^k_{l,m}$
Coriolis	1170	1231	0	1799	−323	−52	243	18	197	−17	−99	−107	106	−320
Surface gradient	−1228	−1125	142	−1814	323	123	−248	24	−140	66	79	72	−84	323
Wind stress	−39	0	−29	0	0	−80	0	0	−57	−57	28	28	−29	0
Bottom friction	72	−68	−79	0	1	6	1	−12	1	8	0	0	3	1
Mixing	78	−125	−149	8	1	18	7	−64	−3	6	−16	20	23	1
Non-linear	0	−3	1	−2	0	0	0	0	0	0	0	0	0	0
Sum ($\sum_k$)	1320 −1268	1231 −1321	143 −257	1807 −1816	325 −323	147 −132	251 −248	42 −76	198 −200	80 −74	107 −115	120 −107	132 −113	325 −320
Velocity	−20	−19	25	0	1	−6	−1	10	−1	−8	1	−1	−4	−1

Table 5. The component of resultant force (X^k, Y^k) acting on all water masses on the North or the South Pacific with the uniform depth of 200 m, the angular moment $M_g{}^k$ about the center of gravity G with the location (Lat^g, $Loug^g$) and the angular moment $M_0{}^k$ about the center of each term $G_0{}^k$ with the location ($Lat_0{}^k$, $Long_0{}^k$). Non-linear terms are all negligibly small.
(dyne, the radius of earth is put to be the unity.)

January Lat^g=23.3°N, $Long^g$=165.6°W						North Pacific
X^k	Y^k	$M_g{}^k$	$M_0{}^k$	$Lat_0{}^k$	$Long_0{}^k$	
2.092	0.015	0.528	0	23.3° N	174.5° E	Coriolis
−2.591	0.369	−0.502	0	23.3° N	180.0°	Surface gradient
0.449	−0.440	−0.065	0	23.3° N	157.5° W	Wind stress
0.040	−0.010	0.071	0.035	25.5° N	136.8° E	Bottom friction
0.038	−0.022	−0.011	0	23.3° N	150.0° W	Mixing
2.619 −2.591	0.384 −0.472	0.599 −0.578				Sum ($\sum_k$)

January Lat^g=31.8°S, $Long^g$=144.7°W						South Pacific
X^k	Y^k	$M_g{}^k$	$M_0{}^k$	$Lat_0{}^k$	$Long_0{}^k$	
−6.673	−0.149	−2.329	0	31.8° S	169.9° W	Coriolis
6.567	0.674	1.325	0	31.8° S	163.3° W	Surface gradient
0.198	−0.605	1.131	0.988	22.9° S	149.5° W	Wind stress
0.006	−0.190	−0.087	0	55.0° S	144.7° W	Bottom friction
0.026	0.046	0.097	0	31.8 · S	115.0° W	Mixing
6.797 −6.673	0.720 −0.944	2.553 −2.416				Sum ($\sum_k$)

July Lat^g=26.2°N, $Long^g$=167.5°W						North Pacific
X^k	Y^k	$M_g{}^k$	$M_0{}^k$	$Lat_0{}^k$	$Long_0{}^k$	
2.831	0.002	0.223	0	26.2° N	174.4° W	Coriolis
−3.024	0.415	0.183	0	26.2° N	162.6° W	Surface gradient
0.119	−0.424	−0.458	−0.376	16.8° N	162.0° W	Wind stress
0.061	−0.049	0.087	0.029	37.5° N	143.3° E	Bottom friction
0.061	−0.122	0.063	0	26.2° N	121.3° E	Mixing
3.072 −3.024	0.417 −0.595	0.556 −0.458				Sum ($\sum_k$)

July Lat^g=28.9°S, $Long^g$=145.6°W						South Pacific
X^k	Y^k	$M_g{}^k$	$M_0{}^k$	$Lat_0{}^k$	$Long_0{}^k$	
−5.945	−0.086	−2.360	0	28.9° S	173.0° W	Coriolis
6.408	0.575	1.966	0	28.9° S	166.3° W	Surface gradient
−0.550	−0.574	0.618	0	28.9° S	92.5° W	Wind stress
0.001	−0.114	−0.045	−0.029	28.9° S	155.0° E	Bottom friction
0.059	0.167	0.204	0.106	60.0° S	125.0° W	Mixing
6.468 −6.495	0.742 −0.774	2.788 −2.405				Sum ($\sum_k$)

satisfy the equations of motion. This table also shows that $\sum_k X^k_{l,m}$ of the East Australian Current and $\sum_k Y^k_{l,m}$ of the Equatorial Counter Current are markedly negative. Then speeds of both currents should decrease when computations are continued. Further, from Table 4 we can reckon the ratio $|X^k_{l,m}|$ to $\sum_k |X^k_{l,m}|$, or $|Y^k_{l,m}|$ to $\sum_k |Y^k_{l,m}|$ every term. The ratio of the surface gradient and Coriolis terms become 40 to 50% respectively, except the equatorial zone. In the equatorial current system the ratio of the wind stress becomes 20 to 30%, especially on the equator it reaches as much as 40%. As to the others friction, non-linear and mixing terms, are less than 3% on the whole, but the ratio of the mixing term reaches 10 to 20% in the Equatorial Counter Current.

Second let us notice the equations (42). The resultant forces and angular moments are given in Table 5, in which the upper part is in the North Pacific and the lower part is in the South Pacific; values in the left side of them are those of January and in the right side are those of July. We have four cases in the study of resultant forces and angular moments. The boundary of the North and the South Pacific coincides with the Equatorial Calm Belt. Then the North Pacific in January is to the north of the paralled of 5°N, and that in July to the north of the latitude 10°N. In this way the Equatorial Counter Current is divided into the North and the South Pacific. Through these four cases, Table 5 shows that the amount of each term acting over the South Pacific is twice as much as that of the North Pacific that the balance of the south components of resultant force X^k is mainly kept by the Coriolis' and surface gradient term, and that the balance of east component Y^k is mainly kept by the surface gradient and wind stress term. These are illustrated in Figure 21. Now, the resultant force of any term can be regarded as a force acting at the center of gravity G, because we can replace the movement of any system of particles by that of the center of gravity G of the system, in which the resultant force acts at the point G. So Figure 21 explains the mechanism of balance among the main terms about G. The North Pacific in January and the South Pacific in July, or the North Pacific in July and the South Pacific in January are making the symmetric figures with each other to the equator. Further, from Table 5 we know that the equations (42) are satisfied on the whole. Especially, as to the first equation, the balance of south component, the residues calculated from the ratio $|\sum_k X^k|$ to $\sum_k |X^k|$, is less than 2 percent, but the second equation, the balance of east component,

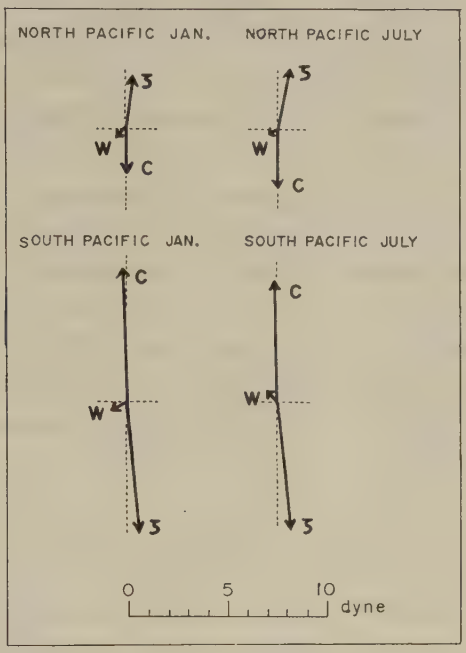

Fig. 21. The balance of forces among the big three terms (see Table 5). *C*, Coriolis ;ζ, surface gradient; *W*, wind stress

has the residues of 20 percent calculated from the ratio $\sum_k Y^k|$ to $\sum_k|Y^k|$. As the balance of east component is mainly kept by the surface gradient and wind stress, elevations may more or less change their distributions if we further continue the computations.

Third we consider the angular moment of each term about the center of gravity G and examine either the equation (46) is satisfied or not. In Table 5, the angular moments about G are given in the column M_g^k, and the locations of G in the four cases are given by Lat^g and $Long^g$. From these results we see that in winter of both Hemispheres the balance of angular moment is mainly kept by the Coriolis and surface gradient term, and that in summer of both Hemispheres the wind stress term plays the important role in the balance of angular moment. This is because the seasonal cold winds in winter, caused by the Siberia or Australian high pressure, have the effects to diminish the total angular moment of wind stress. The equation (46) is well satisfied on the whole, and the ratio of $|\sum_k M_g^k|$ to $\sum_k|M_g^k|$ is less than 10 percent. It is unexpected,

however, that the angular moment of surface gradient has the comparable amount with that of the Coriolis term and that the moments of frictional and mixing term are one order smaller than those of three large terms, the Coriolis, surface gradient and the wind stress. On the Northern Hemisphere, the balance of the angular moments around the center of gravity is kept by the Coriolis and surface gradient term in January, while the moment of wind stress is so great in July that the sum of Coriolis and surface gradient terms is balanced with the wind term. As to the Southern Hemisphere, the sum of the moment of surface gradient and wind stress terms is balanced with that of the Coriolis term both in January and July. Such a large moment of Coriolis term has its chief source in the great whirl located to at the southern part of New Zealand as mentioned in Section 10. We still have strong acceleratious in this whirl and the manner of moment balance may be somewhat modified by variations of whirl pattern when computations are continued further.

Fourth and finally the author computed the location of center of each term, G_0^k, and each proper angular moment about G_0^k, all of which are defined by formulas (47), (48) and (49) (see Table 5). Lat_0^k and $Long_0^k$ are the latitude and longitude of G_0^k respectively, and each proper angular moment is given in the column M_0^k. Although the Coriolis and surface gradient terms are main factors of angular moments about the center of gravity G, yet each of them has the point G_0^k, about which its proper angular moment M_0^k vanishes. From this fact we can say that the elevation and current patterns are symmetric on the whole about the center of each term G_0^k respectively, because in such patterns all forces belonging to surface gradient or Coriolis term pass through the point G_0^k respectively and their angular moments M_0^k about G_0^k become null. The wind stress term also makes its angular moment to be zero in winter of both Hemispheres, but in summer only the wind term has effective proper angular moment showing the great value. This surely agrees with the description about the angular moment of wind stress around the center of gravity in the previous paragraph. According to the dynamics of particles, a system of forces can be replaced by a resultant force passing through a point in the system and a couple of forces around the point. Then the balance of angular moments will be explained more clearly. As mentioned in the third paragraph of this section, the system of forces of the k-th term $(X_{l,m}^k,\ Y_{l,m}^k)$ can be replaced by the resultant force $(X^k,\ Y^k)$ passing through the point G_0^k, and the couple about G_0^k with the moment M_0^k. If the moment M_0^k is zero, G_0^k is not necessarily a point. In this case we can

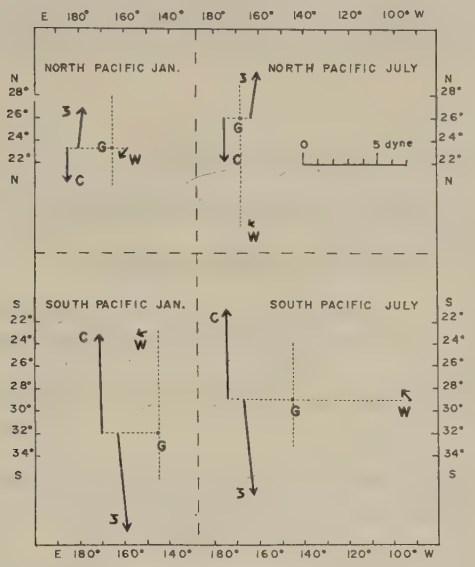

Fig. 22. The balance of angular moment among the big three terms (see Table 5).
C, Coriolis; ζ, surface gradient; *W*, wind stress

find a line along which the total angular moment of the term becomes always null.

In Table 5, the location of G_0^k is chosen at the point whose latitude or longitude takes the value closest possible to that of the center of gravity *G*. In Figure 22, the above-mentioned relations are demonstrated.

Acknowledgements: This numerical experiments were made by use of IBM 704 in 1965 when the author was at Oceanographic Section headed by Dr. J. Sugiura, of J. M. A., receiving from Dr. Y. Masuda many of ideas for the numerical computations of general circulation, from Dr. M. Miyazaki and Dr. J. Masuzawa the useful advices relating to the general aspects of ocean currents. The writer is very grateful to Prof. K. Yoshida of Tokyo University, Prof. K. Hidaka and Dr. K. Takano of Ocean Research Institute of Tokyo University for many helpful discussions at the spring session of the Oceanographic Society of Japan in 1966, when a part of the computed results were lectured. This manuscript has been prepared since the author moved in January, 1966 to the Kobe Marine Observatory, directed by Dr. M. Nakano at that time and by Mr. Y. Fujii

present. The writer also wishes to express his hearty thanks to Dr. K. WATANABE, Chief of Oceanographic Section, for his constant encouragement throughout this work.

References

FISCHER, G. (1959) : Ein Numerisches Verfahren Zur Errechnung von Windstau und Gezeiten in Randmeeren. *Tellus*, **11**, 60-76.

RICHTMYER, R. D. (1957) : Difference methods for initial value problems. *Intersience Publishers, INC*, 59-71.

Japan Meteorological Agency and the Forth District Port Construction Bureau, JMT (1965) : Numerical investigations of storm surges near the Kammon Straits. *Tech. Rep. of J. M. A.*, **40**, 79-80.

UENO, T. (1964) : Theoretical studies on tidal waves travelling over the rotating globe (I). *Oceanogr. Mag.*, **15**, 99-111.

—— (1964) : *ibid.*, **16**, 47-52.

Japan Meteorological Agency (1965) : Tide Tables for the year 1966.

International Union of Geodesy and Geophysics (1959) : Monthly and annual mean heights of sea-level 1957 to 1958. *Publication Scientifique* NO. **20**.

—— (1963) : *ibid.* NO. **24**.

OGURA, S. (1934) : Choseki (The Tides, in Japanese). Iwanami, 231-232.

The Hydrographer of the Navy (1964) : Admiralty tide tables, Volume III, 1965.

The Oceanographical Magazine
Vol. 19, No. 2, December 1967

Cruise Report of CSK Survey by JMA in 1966

By

Hideo Akamatsu and Tsutomu Sawara

Japan Meteorological Agency

(Received December 8, 1967)

Synoptic survey in the adjacent waters of Japan

The semi-synoptic surveys in the adjacent waters of Japan from the eastern sea of Taiwan to the Okhotsk Sea were done by the Japan Meteorological Agency (JMA) in winter and summer of 1966.

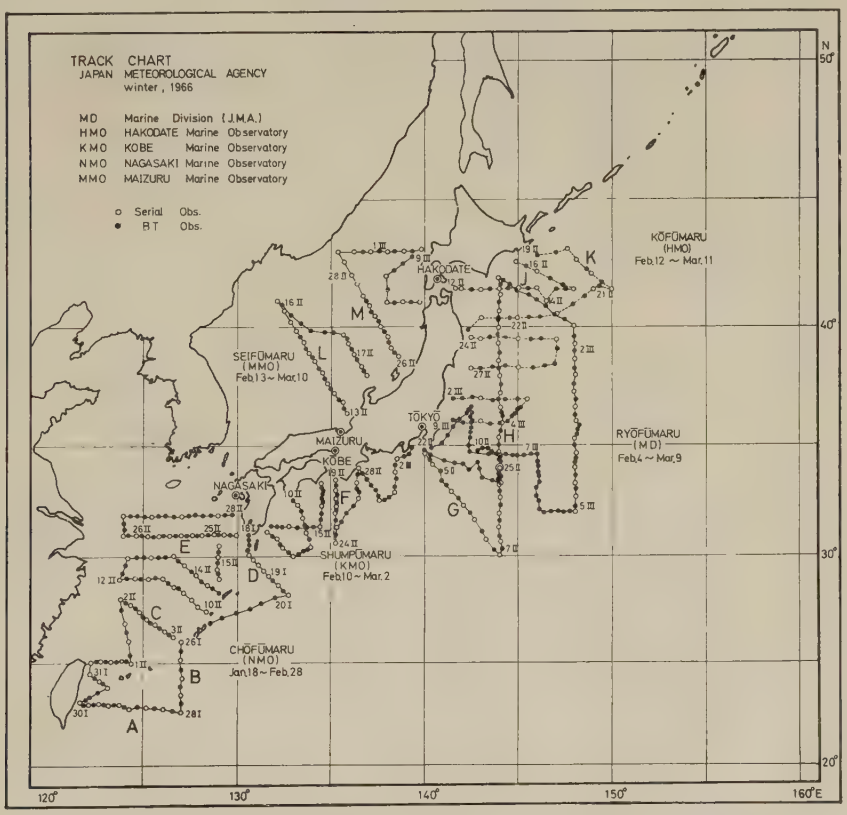

Fig. 1. Track chart, Japan Meteorological Agency, winter 1966.

These surveys are one of the routine oceanographic observations by the JMA, which includes sections declared for the international program "Cooperative

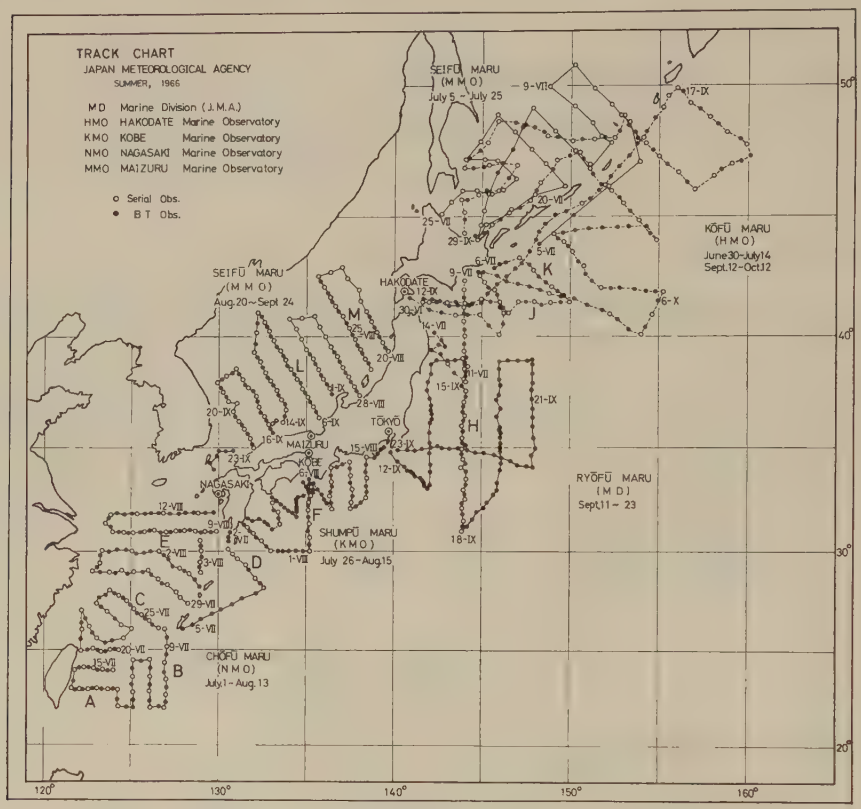

Fig. 2. Track chart, Japan Meteorological Agency, summer, 1966.

Table 1.

Vessel	Agency	Chief scientist		Declared sections	
		Winter	Summer	Winter	Summer
Ryofu Maru	Marine Division	T. SAWARA	H. AKAMATSU	G, H	H
Kofu Maru	Hakodote Marine Observatory	K. KAROHJI	K. HATA	J, K	J, K
Shumpu Maru	Kobe Marine Observatory	S. KONAGA	I. OKUBO	F	F
Chofu Maru	Nagasaki Marine Observatory	T. YAMAGATA	T. YAMAGATA	A,B,C,D,E	A,B,C,D,E
Seifu Maru	Maizuru Marine Observatory	M. YASUI	M. YASUI	L, M	L, M

Study of the Adjacent Regions (CSK)" (Fig. 1 and Fig. 2). Research vessels participated in these surveys are shown in Table 1.

Items of observations

1) Between oceanographic stations while underway
   Observations of maritime meteorology
   Echo-sounding
   Observations of BT and GEK
   Sea surface water sampling for microplankton
2) At oceanographic stations
   The measurement of sea water temperature, salinity, dissolved oxygen, phosphate-P was made at each station, at selected stations was made analysis

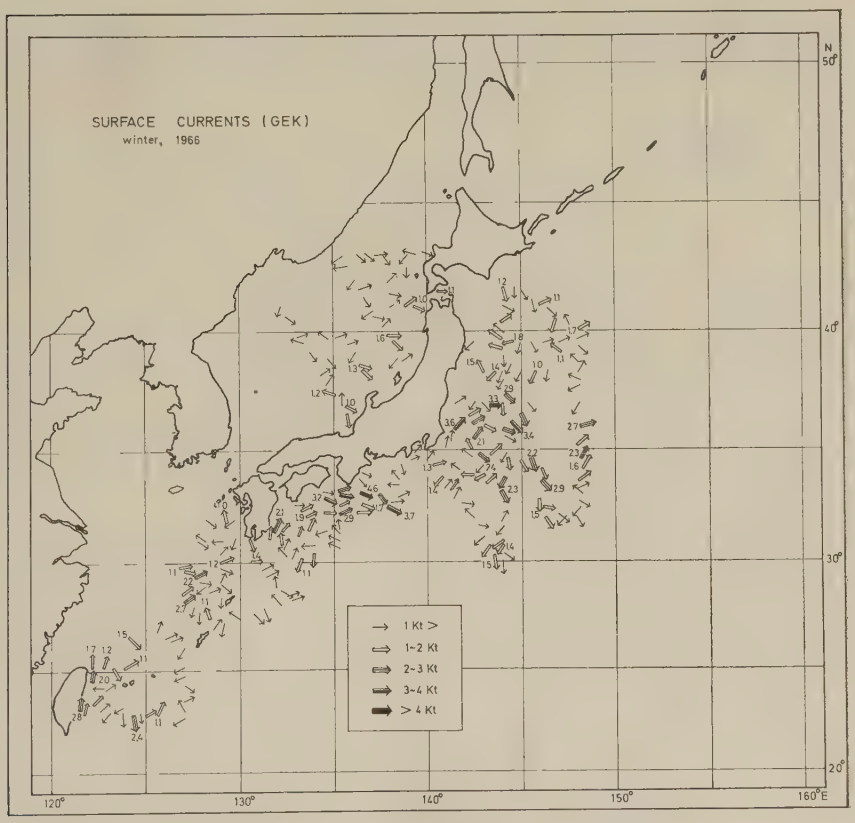

Fig. 3. Surface currents measured with GEK, winter, 1966

of silicate-S, nitrate-N, ammonia-N, total P, pH and alkalinity.

Sampling depths are 0, 10, 20, 30, 50, 75, 100, 125, 150, 200, 250, 300, 400, 500, 600, 700, 800, 1000, 1200, 1500, 2000, 2500, 3000, 3500, 3750, 4000, 4250, 5000 m and so on.

The maximum depth of sampling is usually 1500 m and at some deep hydrographic stations are to bottom.

Zooplankton sampling was made by the vertical hauling of a Norpac net (GG 54, 0.33 mm mesh) from the estimated depth of 150 m to the sea surface at each station.

At some specified stations, zooplankton sampling was done by vertical hauls of an automatic opening-and-closing multiple net from four layers; 0-250 m, 250-500 m, 500-750 m and 750-1000 m.

At selected stations, sea water sampling for microplankton was taken from

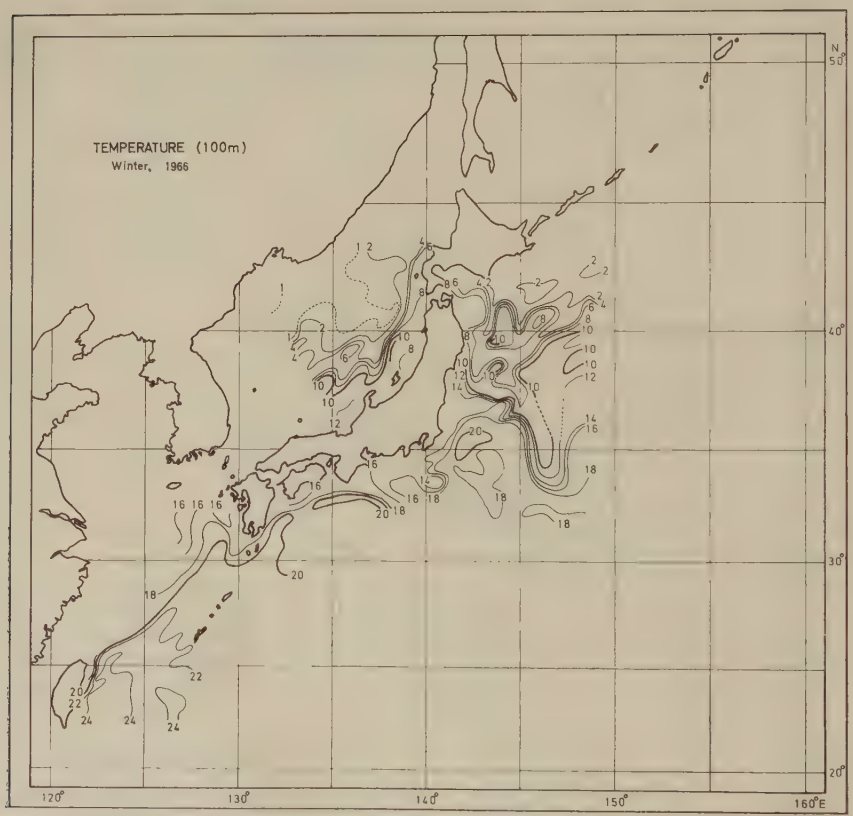

Fig. 4. Water temperature at 100 m, winter, 1966.

each standard depth between sea surface and 400 m by Nansen bottles.

Table 2.

Date	Vessel	Agency	Chief scientist
Jan. 18–19	Chofu Maru	Nagasaki M. O.	T. YAMAGATA
Mar. 16–18	Chofu Maru	Nagasaki M. O.	O. ASAOKA
Apr. 19–20	Chofu Maru	Nagasaki M. O.	T. YAMAGATA
June 5–6	Shumpu Maru	Kobe M. O.	S. KONAGA
July 2–3	Chofu Maru	Nagasaki M. O.	T. YAMAGATA
Aug. 27–30	Chofu Maru	Nagasaki M. O.	T. YAMAGATA
Oct. 27–Nov. 1	Shumpu Maru	Kobe M. O.	S. KONAGA
Dec. 7–8	Chofu Maru	Nagasaki M. O.	O. ASAOKA

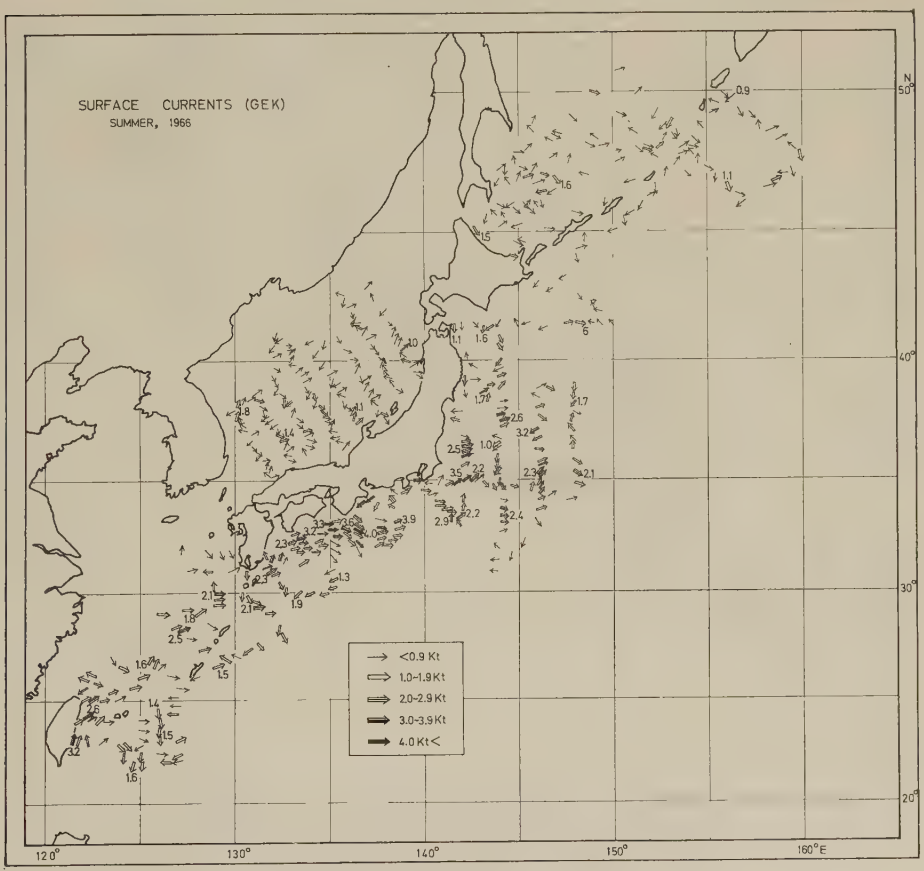

Fig. 5. Surface currents measured with GEK, summer, 1966.

Seasonal observation of the Kuroshio at the south of Kyushu

A regular observation was done on the southeast section of Yaku-shima, south of Kyushu, in order to see the fluctuation of the Kuroshio. The observations are shown in Table 2.

Data report

Fig. 3～Fig. 6 show the surface current and the temperature at 100 m depth. The final data reports of these surveys will be seen in the volumes "The Results of Marine Meteorological and Oceanographical Observations, No. 39 and No. 40" to be published by the JMA.

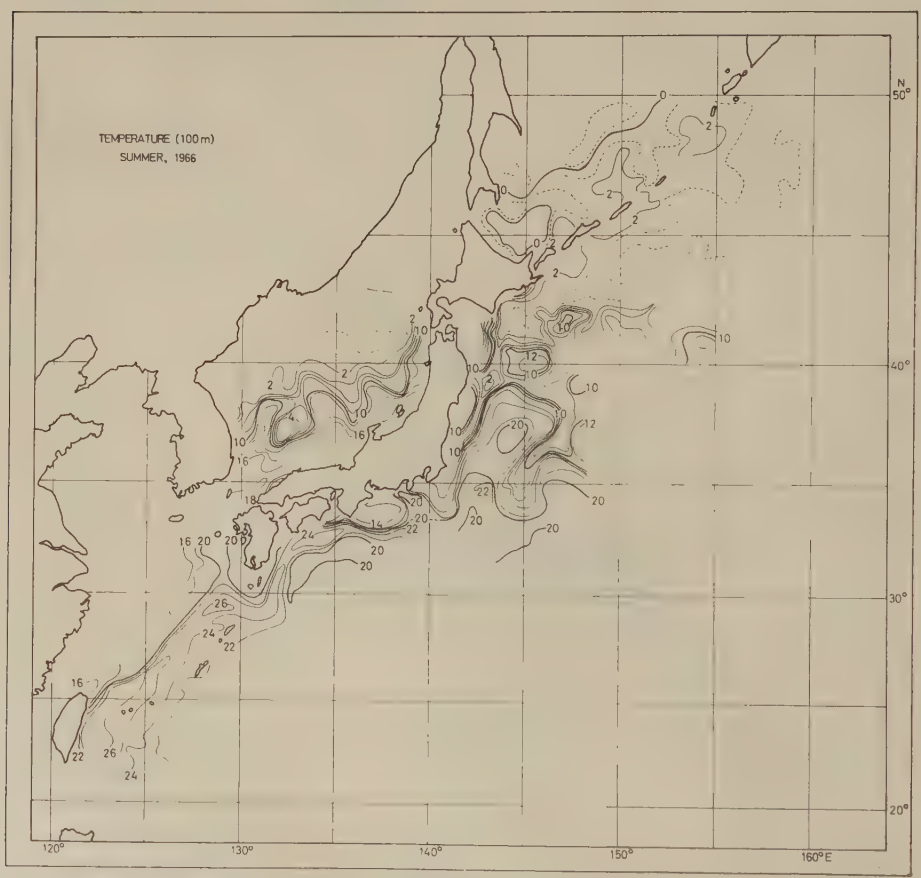

Fig. 6. Water temperature at 100 m, summer, 1966.

The Oceanographical Magazine
Vol. 19, No. 2, December 1967

Tidal Constants along the Coast of Japan (Part II)

By

Masamori MIYAZAKI, Shin-ichi KURONUMA, Tamio INOUE

Japan Meteorological Agency

and

Keiichiro MADOKORO

Geographic Survey Institute

(Received December 7, 1967)

In 1967, we published the tidal constants of 93 ports along the Japanese coast (MIYAZAKI, KURONUMA and INOUE, 1967). As a continuation of the above report, results of tidal analysis at 12 ports will be shown in the following three tables.

Table 1 contains the constants at Oshoro, Aburatsubo, Onisaki, Hosojima, Wajima and Kashiwazaki. All of these stations belong to the Geographic Survey Institute. They read the hourly sea level of one year (January~December, 1966) by using a special type of the automatic reader. These data are automatically punched out, and then analysed by the electronic computer of the Japan Meteorological Agency by Miyazaki's method of harmonic analysis.

Table 2 contains the new constants at three stations; Tomakomai, Nishinomiya and Naha. Among them, Tomakomai and Naha are new stations built by the Hokkaido Development Agency and the Meteorological Agency of Ryukyu, respectively.

In Table 3, some old constants missed in the previous report are shown. These constants were computed by the Geodetic Committee of Japan (HIRAYAMA, 1911) and NAKANO (1941), and are now used in the Tide Tables of the Japan Meteorological Agency.

References

HIRAYAMA, S. (1911); Results of the harmonic analysis of tidal observations made at various ports of Japan. *Journ. Col. Sci. Tokyo* **28**(7), 1-68.

MIYAZAKI, M., S. KURONUMA and T. INOUE (1967); Tidal constants along the coast of Japan. *Oceanogr. Mag.* **19**(1), 13-55.

NAKANO, M. (1941); Tide Tables for the Year 1942. Cent. Met. Obs. of Japan.

Table 1. Tidal constants at the stations belonging to the Geographic Survey Institute.

Station	Oshoro		Aburatsubo		Onisaki		Hosojima(2)		Wajima(2)		Kashiwazaki	
Lat. (N)	43°12′		35°09′		34°54′		32°26′		37°24′		37°21′	
Long. (E)	140 52		139 37		136 50		131 40		136 54		138 31	
H and κ	H	κ	H	κ	H	κ	H	κ	H	κ	H	κ
Sa	7.52	171.92	6.74	176.70	12.42	142.54	14.42	145.34	12.33	171.31	10.16	189.34
Ssa	2.11	290.78	4.22	337.44	5.19	2.75	8.97	359.08	4.83	286.48	5.73	286.57
Mm	1.48	90.11	2.27	255.77	2.20	357.61	1.43	54.80	1.00	117.73	1.02	94.07
Msf	2.34	357.50	0.12	124.16	1.51	265.83	1.43	303.21	3.73	336.90	4.20	343.54
Mf	2.38	228.76	1.52	165.87	1.06	172.61	1.51	162.56	1.79	215.42	2.20	211.98
$2Q_1$	0.31	256.59	0.61	164.73	0.54	151.27	0.44	154.50	0.10	297.71	0.06	346.96
σ_1	0.15	283.91	0.41	131.10	0.68	170.72	0.68	149.70	0.19	325.58	0.10	3.82
Q_1	1.17	307.55	4.04	147.49	3.72	155.82	3.36	157.81	1.22	304.57	1.33	299.12
ρ_1	0.18	336.31	0.68	147.41	0.44	122.49	0.52	156.05	0.28	357.56	0.15	331.61
O_1	5.23	325.53	18.01	157.44	17.69	168.74	16.04	168.68	5.35	320.80	5.49	320.51
$MP_1(\tau_1)$	0.08	238.16	0.66	195.38	1.11	196.40	0.62	171.45	0.21	237.13	0.33	280.15
M_1	0.24	316.70	0.78	153.24	0.81	171.59	0.67	168.68	0.22	314.00	0.19	321.00
π_1	0.08	76.62	0.71	199.37	0.53	349.08	0.43	194.53	0.10	19.94	0.10	348.07
P_1	1.85	351.89	7.70	174.42	7.37	191.08	6.86	187.99	2.13	345.37	1.94	344.92
S_1	0.29	352.68	0.21	56.73	0.85	108.44	0.61	35.17	0.17	96.31	0.23	112.84
K_1	5.38	349.63	23.04	177.67	23.86	189.58	20.80	188.73	5.49	347.62	5.64	347.06
ψ_1	0.24	21.68	0.25	250.76	0.92	207.89	0.04	320.07	0.23	21.17	0.46	62.02
ϕ_1	0.11	56.57	0.16	159.35	0.58	123.60	0.31	157.55	0.14	12.54	0.16	251.33
J_1	0.19	4.98	1.38	200.20	1.31	206.89	1.04	199.70	0.13	3.80	0.12	25.08
SO_1	0.12	130.81	0.10	121.27	0.33	355.81	0.20	240.52	0.04	258.57	0.06	161.43
OO_1	0.15	55.74	0.59	189.99	0.71	236.58	0.70	226.96	0.28	40.86	0.22	24.40
$\varepsilon_2(MNS_2)$	0.10	294.91	0.49	0.47	0.59	119.98	0.41	89.26	0.04	296.48	0.05	239.69
$2N_2$	0.22	44.90	0.96	169.28	1.59	177.47	1.30	160.37	0.29	5.57	0.29	14.31
μ_2	0.32	62.54	0.55	157.15	1.97	199.76	1.61	169.75	0.33	23.95	0.45	28.45
N_2	1.13	98.27	6.37	142.19	11.53	177.65	9.96	166.91	1.55	66.75	1.56	66.21
ν_2	0.11	100.21	1.02	162.61	1.35	144.59	1.75	167.78	0.31	93.64	0.22	54.06

Table 1. (Continued)

Station	Oshoro		Aburatsubo		Onisaki		Hosojima(2)		Wajima(2)		Kashiwazaki	
Lat. (N)	43°12′		35°09′		34°54′		32°26′		37°24′		37°21′	
Long. (E)	140 52		139 37		136 50		131 40		136 54		138 31	
H and κ	H	κ	H	κ	H	κ	H	κ	H	κ	H	κ
OP_2	0.12	357.97	0.37	234.17	2.22	355.75	0.68	335.13	0.08	31.83	0.16	322.99
δ_2	0.10	243.25	0.58	9.60	4.36	187.72	0.84	100.17	0.33	203.72	0.38	222.17
M_2	5.04	117.65	36.29	146.71	60.66	180.59	51.61	175.19	5.99	83.04	6.04	84.74
MKS_2												
λ_2	0.06	14.74	0.50	137.42	0.49	86.57	0.26	211.56	0.04	108.84	0.05	162.05
L_2	0.17	91.83	1.77	181.71	3.09	191.00	1.71	183.44	0.07	56.86	0.12	56.86
T_2	0.19	153.44	1.01	185.15	0.81	162.27	1.50	194.09	0.15	87.94	0.23	116.18
S_2	2.32	149.84	16.86	176.10	28.96	207.48	22.30	199.18	2.10	110.12	2.25	114.22
R_2	0.07	27.60	0.37	285.94	1.86	48.45	0.35	251.60	0.01	142.70	0.08	359.97
K_2	0.62	144.15	4.74	172.38	7.36	197.04	6.29	193.75	0.66	107.13	0.60	108.41
$\eta_2(KJ_2)$	0.05	147.32	0.44	169.58	0.51	211.90	0.45	220.80	0.03	19.21	0.07	94.65
$2SM_2$	0.04	133.82	0.47	15.67	0.29	351.33	0.07	35.37	0.09	249.84	0.06	208.17
MO_3	0.08	336.67	0.20	340.77	0.15	311.06	0.10	122.24	0.06	247.85	0.06	308.31
M_3	0.18	206.82	0.18	153.10	1.47	209.03	0.61	178.01	0.03	187.93	0.03	228.51
SO_3	0.06	236.17	0.09	296.45	0.53	255.93	0.17	172.90	0.05	190.48	0.02	213.18
MK_3	0.07	331.49	0.99	237.09	0.65	348.80	0.12	305.23	0.07	271.67	0.07	277.93
M_4	0.13	217.00	0.47	93.71	0.71	101.03	0.10	344.30	0.14	52.95	0.16	60.06
MS_4	0.06	185.38	0.38	223.74	0.79	131.52	0.26	33.73	0.12	79.06	0.16	88.27
$2MN_6$												
M_6	0.03	22.67	0.53	293.21	0.22	335.36	0.11	234.19	0.01	145.72	0.02	64.78
$2MS_6$	0.04	304.07	0.51	318.84	0.27	257.53	0.12	185.51	0.01	15.29	0.02	330.21
$2MK_6$												
Period of Analysis	1966, Jan.~Dec.		1966, Jan.~Dec.		1966, Jan.~Dec.		1966, Jan.~Dec.		1966, Jan.~Dec.		1966, Jan.~Dec.	
Method	Miyazaki		Miyazaki		Miyazaki		Miyazaki		Miyazaki		Miyazaki	
References	Newly analysed		Newly analysed		Newly analysed		Newly analysed		Newly analysed		Newly analysed	

Table 2. Tidal constants newly analysed by the Japan Meteorological Agency.

Station	Tomakomai		Nishinomiya		Naha(2)	
Lat. (N)	42°38′		34°43′		26°12′	
Long. (E)	141 38		135 20		127 40	
H and κ	H	κ	H	κ	H	κ
Sa	8.49	164.75	15.12	165.95	13.68	139.51
Ssa	6.91	253.49	5.08	239.77	5.05	124.86
Mm	0.83	337.44	1.43	293.84	0.37	335.41
Msf	1.40	174.18	0.39	358.91	1.01	347.15
Mf	0.84	190.59	1.35	235.28	0.42	66.84
$2Q_1$	0.56	141.76	0.40	191.79	0.52	777.33
σ_1	0.51	136.50	0.37	234.36	0.74	175.25
Q_1	4.04	141.71	3.56	172.27	3.26	182.05
ρ_1	0.84	146.86	0.88	179.73	0.68	183.19
O_1	18.59	150.58	17.80	184.64	15.53	190.77
$MP_1(\tau_1)$	0.30	108.28	0.18	295.93	0.40	193.48
M_1	0.92	133.43	0.84	220.58	0.70	181.60
π_1	0.48	157.28	0.18	195.94	0.42	202.85
P_1	7.62	165.62	7.19	205.01	7.16	210.54
S_1	1.07	343.24	0.38	67.99	0.23	356.96
K_1	23.36	168.41	24.20	206.93	20.41	211.29
ψ_1	0.51	102.76	0.29	266.81	0.40	313.07
ϕ_1	0.43	171.55	0.43	98.81	0.47	236.76
J_1	1.06	181.23	1.00	232.62	1.11	227.90
SO_1	0.23	172.57	0.95	16.38	0.27	286.62
OO_1	0.56	211.47	0.62	254.86	0.68	252.53
$\varepsilon_2(MNS_2)$	0.18	134.26	0.85	194.82	0.48	167.41
$2N_2$	0.47	116.75	1.48	233.67	1.33	184.28
μ_2	0.54	149.08	4.14	167.79	1.60	191.53
N_2	4.16	92.69	5.47	211.77	11.27	189.70

Table 3. Tidal constants computed by the Geodetic Committee of Japan and by NAKANO.

Station	Hanasaki(2)		Ito(2)		Kushimoto(2)	
Lat. (N)	43°17′		34°58′		33°28′	
Long. (E)	145 35		139 07		135 46	
H and κ	H	κ	H	κ	H	κ
Sa	4.1	233.0	9.2	175.0	14.6	165.7
Ssa	2.9	224.2	2.1	207.0	3.8	341.8
Mm	1.4	73.5			1.6	182.6
Msf	1.2	69.5			1.1	52.0
Mf	1.9	171.7			1.2	201.5
$2Q_1$						
σ_1						
Q_1	4.9	152.6	3.7	151.1	3.6	159.7
ρ_1						
O_1	21.9	165.3	18.9	158.1	16.7	166.7
$MP_1(\tau_1)$						
M_1	1.1	198.4			1.0	154.0
π_1						
P_1	7.0	177.1	7.9	169.1	7.5	182.8
S_1	1.2	17.5			0.6	9.8
K_1	20.9	177.3	23.5	169.1	21.9	187.9
ψ_1						
ϕ_1						
J_1	1.3	169.0			1.2	206.6
SO_1						
OO_1						
$\varepsilon_2(MNS_2)$						
$2N_2$						
μ_2	0.5	133.0	0.9	141.2	1.3	171.1
N_2	3.5	91.1	6.1	147.2	8.4	172.6

Table 2. (Continued)

Station	Tomakomai		Nishinomiya		Naha[2]	
Lat. (N)	42°38′		34°43′		26°12′	
Long. (E)	141 38		135 20		127 40	
H and κ	H	κ	H	κ	H	κ
ν_2	0.73	88.10	0.49	265.56	2.33	191.41
OP_2	0.21	148.01	1.27	81.41	1.23	186.76
δ_2	0.79	144.99	0.50	147.54	1.27	96.33
M_2	31.77	109.59	27.42	216.52	57.53	199.10
MKS_2						
λ_2	0.37	90.86	0.45	61.86	0.69	209.68
L_2	1.65	120.10	1.34	336.61	2.46	209.34
T_2	0.66	144.85	0.71	253.46	1.88	237.75
S_2	14.43	148.33	15.55	231.86	23.67	223.34
R_2	0.11	29.09	0.27	165.93	0.75	216.09
K_2	4.23	141.99	3.97	226.53	6.97	221.36
$\eta_2(KJ_2)$	0.29	133.95	0.47	222.14	0.34	232.40
$2SM_2$	0.18	8.09	0.75	286.98	0.39	97.76
MO_3	0.19	319.71	1.74	330.71	0.19	106.99
M_3	0.61	102.89	0.53	243.91	0.76	211.74
SO_3	0.07	277.78	1.21	5.88	0.13	28.18
MK_3	0.03	132.37	1.15	344.17	0.06	43.45
M_4	0.31	91.64	1.42	47.32	0.37	268.92
MS_4	0.12	352.61	1.27	90.29	0.23	292.51
$2MN_6$						
M_6	0.64	234.11	1.46	103.43	0.04	333.06
$2MS_6$	0.59	272.06	1.47	264.54	0.21	241.94
$2MK_6$						
Period of Analysis	1967, Jan.~Dec.		1963, April ~1964, March		1966, Aug. ~1967, July	
Method	Miyazaki		Miyazaki		Miyazaki	
References	Newly analysed		Newly analysed		Newly analysed	

Table 3. (Continued)

Station	Hanasaki[2]		Ito[2]		Kushimoto[2]	
Lat. (N)	43°17′		34°58′		33°28′	
Long. (E)	145 35		139 07		135 46	
H and κ	H	κ	H	κ	H	κ
ν_2	0.9	87.1	1.5	112.2	1.9	161.2
OP_2						
δ_2						
M_2	27.4	117.0	38.1	151.2	45.7	175.3
MKS_2						
λ_2						
L_2	1.2	130.5	1.8	174.2	1.6	174.6
T_2	1.3	161.9			1.6	194.1
S_2	12.2	159.6	17.4	177.2	20.5	198.4
R_2	0.9	75.1			0.6	123.0
K_2	3.5	151.6	4.9	175.2	5.7	194.9
$\eta_2(KJ_2)$						
$2SM_2$	0.5	71.4			0.8	343.6
MO_3						
M_3	0.5	132.7			0.5	202.2
SO_3						
MK_3						
M_4	0.3	131.1	0.2	115.4	0.1	200.4
MS_4	0.8	132.0			1.4	159.3
$2MN_6$						
M_6	0.1	158.4			0.1	107.4
$2MS_6$						
$2MK_6$						
Period of Analysis	1897, 1899~1902		—		1897~1899, 1904~1905	
Method	Darwin		Darwin		Darwin	
References	HIRAYAMA (1911)		NAKANO (1941)		HIRAYAMA (1911)	

The Oceanographical Magazine
Vol. 19, No. 2, December 1967

The Gross β-radioactivity of Fallout collected at the Southern Weather Station located in 29°N and 135°E

By

Hirozo YOSHIMURA

Japan Meteorological Agency

(Received December 14, 1967)

1. *Introduction*

In order to strengthen the β-radioactivity survey of fallout, collection of fallout sample has been done aboard the observation ship staying around the marine weather station "Tango" (29° N, 135° E) in every summer season since 1957. To collect fallout samples, a sheet of gummed paper is spread on an even plate installed on a bridge of the ship.

The exposure of gummed paper is started from 9 o'clock in every morning and lasts for 24 hours. Collection of fallout samples is continued from the end of May to the beginning of November. Samples are brought to the laboratory on land for the measurement of gross β-activity.

2. *Measuring procedure*

In the laboratory, each sheet of gummed paper on which the fallout sample has been collected is ignited at 600°C in a porcelain crucible. Ash left after ignition in the crucible is transferred to a planchet and the gross β-activity is measured by a Geiger counter with a mica window with thickness of about 1.5 mg/cm^2. The planchet is set at a distance of 1.0 cm from the mica window in the Geiger counter.

Time from several days to twenty days or more has elapsed before mesurement since sample collection. Time duration of measurement reaching the present counts, *i.e.* 1,200 counts and 1,600 counts respectively for sample and background, is automatically recorded. In this case, time is recorded in turn every 400 counts respectively for sample and for background.

The counting efficiency has been decided to be about 16% under the above-mentioned geometrical condition by using the U_3O_8 standard (500 dps).

The collection efficiency of a gummed paper is controversial. According to "The Reports of Scientific Committee on Effect of Atomic Radiation", it is 20 to 60% of that by the water basin method depending on dry or wet weather. It is 60% in the case of no rain. But actually, the collection efficiency is not taken into account on the gross β-activity shown in Table 1 because of the difficulty in choice of an appropriate efficiency value depending on the weather condition.

3. Results and discussion

Frequency distribution of the daily activity level is shown in Table 1. Table 2 shows the monthly summarized gross β-activity level, which means the simple addition of daily activity levels. From Tables 1 and 2, we can see the remarkable prominence of radioactivity in 1958 and in 1961 to 1963 in spite of the inevitable ambiguity pertaining to the significance of the gross β-activity at the time of measurement expressed in terms of cpm or mCi converted from cpm by means of the U_3O_8 standard. It is noteworthy that two, remarkable prominences of gross β-activity previously pointed out coincide well with two peaks in number of nuclear explosions.

Table 3 shows the monthly accumulated Cs-137 and Sr-90 activities. The comparison of Table 2 and 3 clarifies the following points: The large discrepancy between the gross β-activity and the summarized activities of Cs-137 and Sr-90 suggests the short lapse of time after nuclear explosion. On the order

Table 1. Frequency distribution of the daily activity level.

Year	Days of observation	Range of activity level (mCi/km²)						Number of nuclear explosion in atmosphere
		0~0.01	0.01~0.1	0.1~1	1~10	10~100	100~1000	
1957	139	36	86	17				46
1958	143	2	32	79	22	5	3	82
1959	136	30	84	22				0
1960	127	53	72	2				3
1961	122	38	59	16	8	1		32
1962	150	4	42	91	12	1		74
1963	143	4	45	89	3	2		0
1964	161	25	104	30	2			1
1965	162	77	82	3				2
1966	161	73	73	15	1			3

Table 2. The monthly summarized gross β-radioactivity level.

Year	Summarized activity level during June to Oct. mCi/km²	Monthly summarized activity level mCi/km²				
		June	July	Aug.	Sept.	Oct.
1957	11.4	1.28	0.89	2.06	1.80	5.39
1958	715.5	20.58	658.80	13.82	3.88	18.20
1959	7.4	2.91	1.11	0.91	1.24	1.20
1960	2.6	0.49	0.22	0.37	0.70	0.90
1961	45.8	1.04	1.00	1.33	10.16	32.30
1962	78.2	22.63	18.21	4.18	7.58	25.61
1963	66.7	7.94	4.86	28.93	4.84	20.12
1964	21.8	3.10	1.49	0.97	0.71	15.63
1965	3.1	0.61	0.47	0.42	0.78	0.86
1966	4.9	3.09	0.56	0.53	0.44	0.24

Table 3. The monthly accumulated Cs-137 and Sr-90 activities in Tokyo.

Year	Summarized activity level during June to Oct. mCi/km²		Monthly accumulated Cs-137 and Sr-90 activities mCi/km²									
			June		July		Aug.		Sept.		Oct.	
	Cs-137	Sr-90	Cs-137	Sr-90	Cs-137	Sr-90	Cs-137	Sr-90	Cs-137	Sr-90	Cs-137	Sr-90
1957	7.93	1.74	4.01	0.64	1.03	0.37	0.52	0.16	1.94	0.42	0.43	0.15
1958	5.86	2.89	1.26	0.41	1.45	1.21	0.85	0.36	0.99	0.19	1.31	0.72
1959	7.15	2.52	3.54	1.67	1.24	0.31	0.77	0.19	0.72	0.20	0.88	0.15
1960	1.63	0.79	0.64	0.20	0.41	0.13	0.24	0.24	0.20	0.14	0.14	0.08
1961	4.28	1.03	0.57	0.31	0.11	0.05	0.08	0.02	0.30	0.05	3.22	0.60
1962	8.52	2.98	4.18	1.21	1.60	0.80	0.70	0.29	0.31	0.10	1.73	0.58
1963	36.60	11.85	14.8	4.59	5.10	2.24	7.09	1.89	5.33	1.66	4.28	1.47
1964	5.12	3.13	2.58	1.24	0.81	0.53	0.53	0.28	0.57	0.45	0.63	0.63
1965	4.08	1.55	1.82	0.59	0.49	0.18	0.97	0.34	0.48	0.33	0.32	0.11
1966	1.78	0.62	1.10	0.36	0.27	0.10	0.19	0.06	0.13	0.06	0.09	0.04

These results are given by the Meteorological Research Institute.

hand, the small discrepancy means the long lapse of time after explosion or lower collection efficiency of fallout due to the wash-out effect of fallout by rainfall.

For example, the quite large difference in 1958 suggests the more frequent and large-scale explosion done in that year. Approximate coincidence at the lower level of two sorts of data in 1959 and that at the higher level in 1963 indicate no explosion in those years and the more evident effect due to fallout from the stratosphere in 1963 than in 1959. In several examples of monthly summarized gross β-activity in September, which is one of the most rainy months

in a year, the lower gross β-activity as compared with the summation of Cs-137 and Sr-90 activities can be seen, which suggests the lower collection efficiency of fallout by the gummed paper method due to the wash-out effect by rain.

4. Conclusion

The measurement of the gross β-activity should be done as possible after the decay of short-lived daughter products of natural radioactive materials. But, in this study the measurement had to be done rather capriciously, *i.e.* sometimes in a long time or shorter time after collection and correction for decay had to be left disregarded because of difficulty in treatment. In addition, there is some ambiguity in estimation of the collection efficiency of fallout by gummed paper. Despite of those uncertainties, the data on the gross β-activity collected at the southern weather station may be an indicator of fallout.

The comparison of the gross β-activity data with the long-lived nuclides (Cs-137, Sr-90) data revealed the following points:

1) Whether the lapse of time after explosion is large or small.
2) Whether there is a remarkable stratospherical radioactive fallout or not.
3) Whether there is a remarkable effect reducing the collection efficiency of fallout due to rainfall or not, especially in a long time after explosion.

Acknowledgements: The present author wishes to express his sincere appreciation to Dr. Yoshio SUGIURA, Meteorological Research Institute, who read the manuscript and gave him many useful discussions. Thanks are also due to Mr. Y. KATSURAGI, Meteorological Research Institute, for his kind permission to cite Cs-137 and Sr-90 data in Tokyo, Mr. T. AKIYAMA given the convenience at my work, Messrs. T. MATSUMOTO and H. ITAKURA for their cooperation in sampling and Mr. Y. NAKAZAWA, Ibaraki Prefectural Hygienic Laboratory, for his cooperation in measurement.

References

Japan Meteorological Agency (1958): Bulletin of the atmospheric radioactivity. No. 14 and No. 15.

Scientific Committee on the Effects of Atomic Radiation, United Nations (1962): Production and transport of nuclear weapons debris.

KATSURAGI, Y. (1965): Deposition of Sr-90 and Cs-137 in Japan (I) (II). *Tenki*, **12**](10), 5~14 (In Japanese).

The Oceanographical Magazine
Vol. 19, No. 2, December 1967

The Ito Marine Observation Tower

By

Kozo Hishida

Meteorological Research Institute

(Received December 15, 1967)

A marine observation tower was erected by the Meteorological Research Institute on 29 December 1963, near Ito City, Shizuoka Prefecture (lat. 34°58.6′ N, long. 139°6.1′ E) at a point 600 m distant from the seashore and 20 m deep from the datum level (Fig. 1). This tower was constructed for the purpose of acquiring more knowledge of water temperature prediction, and if possible, for the various oceanic and meteorological environments. Observations have been carried out automatically since the beginning of 1964.

The tower consists of a platform containing an instrument house of hexagon

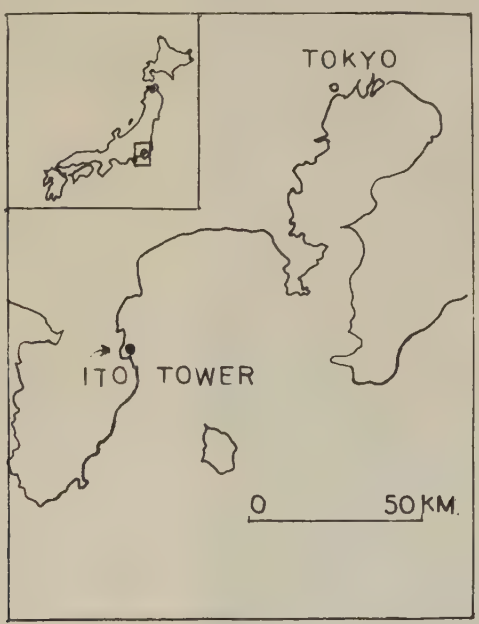

Fig. 1.

shape, supported by a long hollow steel pipe of 90 cm in diameter. The pipe is sustained vertically by six oblique hollow columns, the ends of which are fastened to three steel boxes of rectangular shape, 20 meters long (Fig. 2). This structure

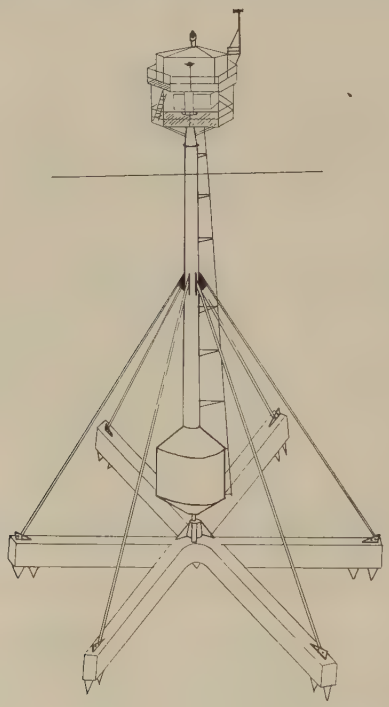

Fig. 2.

was made at Yokosuka and navigated by tug-boat to Ito where it was set in the sea by placing concrete blocks in the three steel boxes. This new idea of construction was adopted for the sake of saving the expense of erection, utilizing that the soil ground of the bottom was sands in this place.

It is intended not only to survey sea water temperature, but also to find the various oceanographic and meteorological factors which control and cause changes of water temperature. Owing to the shortage of manpower it was decided that the observations should be made automatically. And therefore, the unmanned type of structures with an electronic measuring system was adopted. The electric power driving instruments came from a 12 V, 700 A battery charged through a diesel generator and a 12 V, 60 A battery charged through a solar cell for reserve, but since August 1966, a submarine cable was buried from the seashore and it became possible to receive the A.C. power of 100 V at the tower.

The following instruments are installed:

Aerovane	at 10 m height
Pyranometer or Albedometer	at 10 m height
Net Radiometer	at 10 m height
Thermometer	at six layers in the water and at two heights in the air
Hygrometer	at 10 m height
Salinometer	at two layers in the water
Electric current meter	at 3 m depth
Wave recorders	
Pressure-type tide gauge	
Turbidimeter	at 3 m depth

The results of observation at this marine tower will be reported in other papers, but it may be said that it promises to be an invaluable tool for extending our knowledge of sea surface water temperature prediction, oceanic environments and meteorological conditions immediately above the sea (Fig. 3).

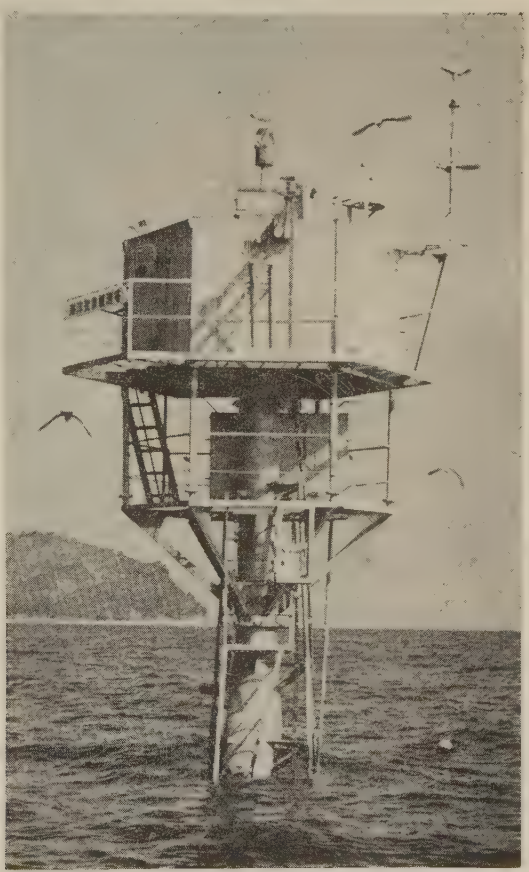

Fig. 3. Ito Marine Observation Tower.

The Oceanographical Magazine
Vol. 19, No. 2, December 1967

Oceanographic Studies of the Japan Sea (1)
—Water Characteristics—

By

Masashi YASUI, Takeo YASUOKA, Katsumi TANIOKA and Osami SHIOTA

Maizuru Marine Observatory

(Received December 18, 1967)

Abstract: The data of more than 3,000 hydrographic stations, which were carried out for the last 44 years, were compiled in terms of the frequency of potential temperature and chlorinity relationships to analyse water masses in the Japan Sea. About 84% of the entire volme of the sea has characteristics between 0° and 1°C and between 18.80‰ and 18.90‰ Cl. The temporal variation can be recognized only in upper 200 m layers. Examples of seasonal mean temperature and chlorinity charts which were derived as by-products in the procedure were also shown.

1. Introduction

Although the Japan Sea is a rather small marginal sea enclosed by the Japan Archipelago, the Korean Peninsula and the Siberian Continent, it is so peculiar from the point of view of the descriptive oceanography that many authors (e.g. SUDA *et al.*, 1930 & 1932; FUKUOKA, 1962 & 1965) presented many kinds of reports. One of characteristic features mentioned by them was the homogeneity of the water mass. However, this was not results of statistics, but was inferred mainly from data in a certain epoch.

The aim of this paper is to summarize the results of compiling data, which could be obtained, in terms of the frequency of potential temperature and chlorinity relationships by means of the method exploited by COCHRANE (1958), MONTGOMERY (1958) and so on.

2. Method

In the present work, the authors defined the Japan Sea as a sea south of the 45°N circle and north of the Tsushima Straits. In this area, data of more than 4,000 hydrographic stations have been reported for the last 44 years, including the famous data measured aboard Old Japanese Navy Research Ship "Yamato" in 1924. Among those data, those which seem to be obviously unreliable were

excluded from the data of this work. The data source and numbers which were adopted are listed in Table 1 & 2.

Based on these data volumes of watermasses whose potential temperature and chlorinity fall within certain divisions of T-Cl diagrams were computed. As the class intervals, 1.0°C for potential temperature 0.1 per mil for chlorinity were adopted for the coarser class for the entire Japan Sea and 0.05°C and 0.02 per mil for the finer class for water colder than 1.0°C. In converting measured temperature to potential temperature, the table prepared by HELLAND HANSEN (SVERDRUP *et al.*, 1942) was used.

The number of data was so large that the grid average of one degree square in the latitude and longitude was calculated. This procedure seems to be effective for eliminating influences of unevenness in the distribution and reliability of

Table 1. List of selected data.

Source	Year (Serial No.)	Institute of Publication
Semiannual Report of Oceanographical Investigation	1924 (No. 26) 1931 (No. 48, 49) 1932 (No. 50, 51) 1933 (No. 52, 53) 1934 (No. 54, 55)	Imperial Fisheries Experi. Stat.
Journal of Oceanography	1928 (Vol. 2, No. 1) 1929 (Vol. 3, No. 2)	Imperial Marine Observatory
Hydrographic Bulletin	1952, '53 (No. 51) 1954, '55 (No. 58) 1956 (No. 62) 1957 (No. 64) 1958 (No. 66) 1959 (No. 68) 1960 (No. 75) 1961 (No. 77)	Maritime Safety Agency
Bulletin of Japan Sea Regional Fisheries Research Laboratory	1955, 1956	Japan Sea Regional Fisher. Res. Lab.
Oceanographical Prompt Report	1959 (No. 90) 1960 (No. 100, 104) 1961 (No. 109, 114) 1962 (No. 121, 126, 129) 1963 (No. 133, 135) 1964 (No. 150, 152, 155) 1965 (No. 158, 162, 164, 166) 1966 (No. 170, 173, 178) 1967 (No. 182, 187)	Maizuru Marine Observatory
Results of Fisheries Oceanographic Observation	1963	Fisheries Agency
Technical Report	1962, 1963, 1964	R.O.K. Navy. Hydrogra. Office (Republic of Korea)
Annual Report of Oceanographic Observation	1963	Fisher. Res. and Develop. Agency (Republic of Korea)

Table 2. Number of data at selected depths in each season.

Season	Winter		Spring		Summer		Autumn		Total	
Depth(m)	Temp.	Cl	Temp.	Cl	Temp.	Cl	Temp.	Cl	Temp.	Cl
0	706	711	1106	968	563	548	844	679	3219	2906
50	701	703	1084	956	539	539	852	677	3176	2875
100	677	656	985	845	501	506	764	617	2927	2624
200	557	556	787	713	420	436	588	498	2352	2203
400	456	456	402	404	285	298	286	265	1429	1423
600	378	379	265	253	189	184	151	151	983	967
1000	285	285	163	158	68	68	25	25	541	538
2000	78	78	66	35	28	26	23	23	195	162
Total	3838	3826	4858	4332	2593	2605	3537	2935	14822	13698

data. After making grid average in a layer of a certain depth, isothermal and isohaline lines were contoured and the area which was occupied by a certain water mass was measured. To get volume of a certain water mass, the area occupied by the certain water mass were integrated numerically in the vertical direction.

In the procedure, mean temperature- and chlorinity- distributions were charted in depths of 0, 50, 100, 200, 400, 600, 1,000 and 2,000 m for every season. Meaning of these depth is: 50 m is the bottom of the first thermocline, 100 m is the useful depth to signify the feature of the Tsushima Warm Current, 200 m is the depth of the second thermocline, 400 m is the depth of the minimum chlorinity, 600 m is the depth of the minimum contents of dissolved oxygen, 1,000 m is the depth of the minimum temperature *in situ*. Though the interval of the depths deeper than 1,000 m seems to be too large, potential temperature and chlorinity in water deeper than 1,000 m were so homogeneous that characteristics in deep water can be represented by the distribution in 2,000 m depth. In the work, the chart of the Albers' equal area projection was used. As the chart of bottom topography, the bathymetric chart presented by ZENKEWITCH (1961) with the Mercator's projection was converted to the chart projected by the same manner mentioned above. The volume of the Japan Sea numerically calculated from this chart was 1,720,000 km^3.

The intervals between contouring lines are 1.0°C and 0.1‰ Cl in general. Moreover, isothermal and isohaline lines are contoured with intervals of 0.05°C and 0.02‰ Cl for the water mass colder than 1.0°C.

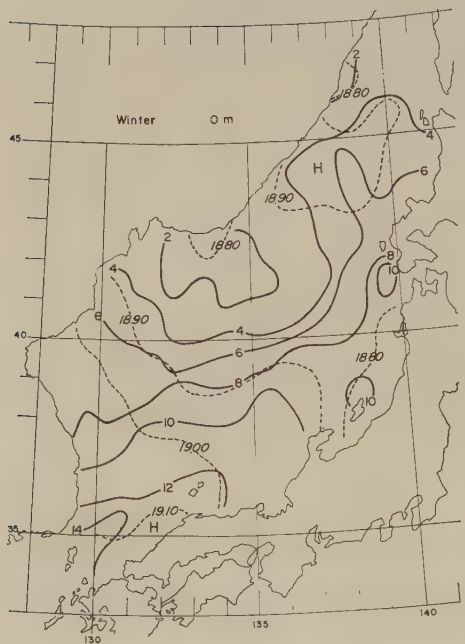
Winter 0 m
H
1880
1890
1900
1910
45
40
35
130
135
140

(a)

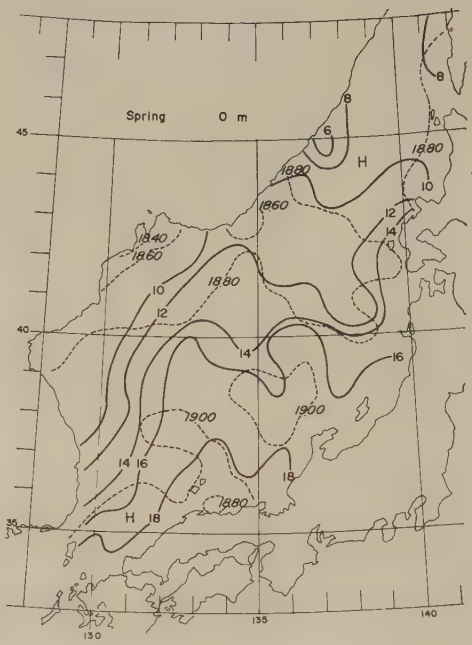
Spring 0 m
H
1860
1880
1900
45
40
35
130
135
140

(b)

Fig. 1.

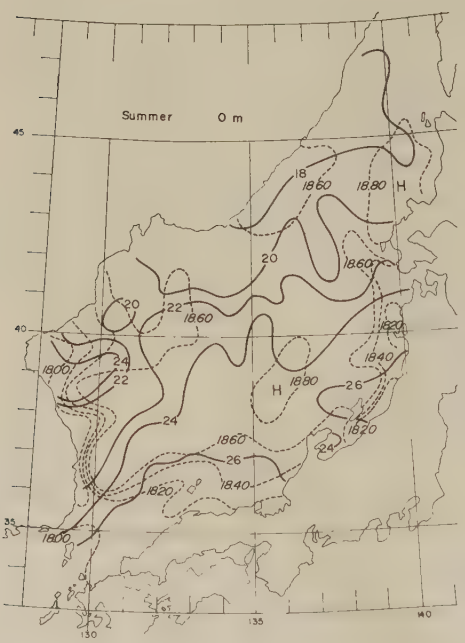
Summer 0 m
H
1860
1880
1890
1900
45
40
35
130
135
140

(c)

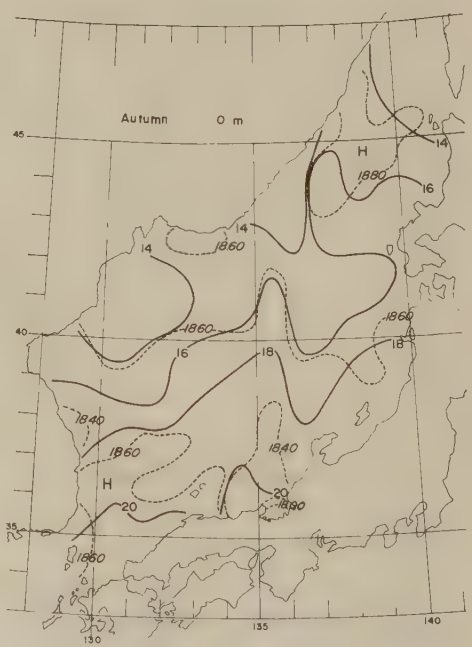
Autumn 0 m
H
1860
1880
1890
45
40
35
130
135
140

(d)

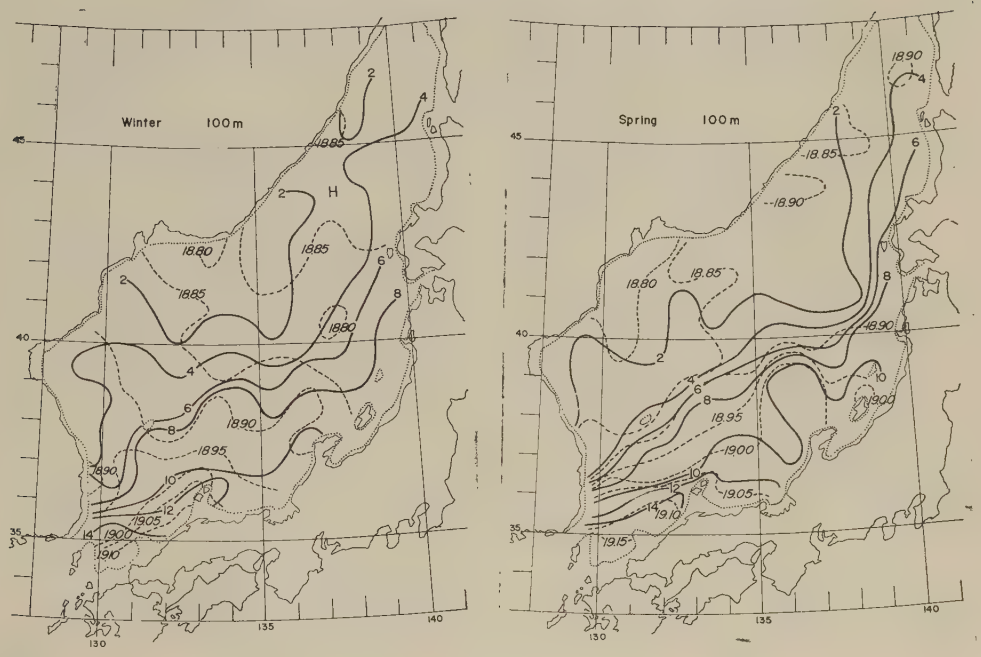
Winter 100m
Spring 100m
Summer 100m
Autumn 100m
45
40
35
130
135
140

Fig. 2. (a) (b) (c) (d)

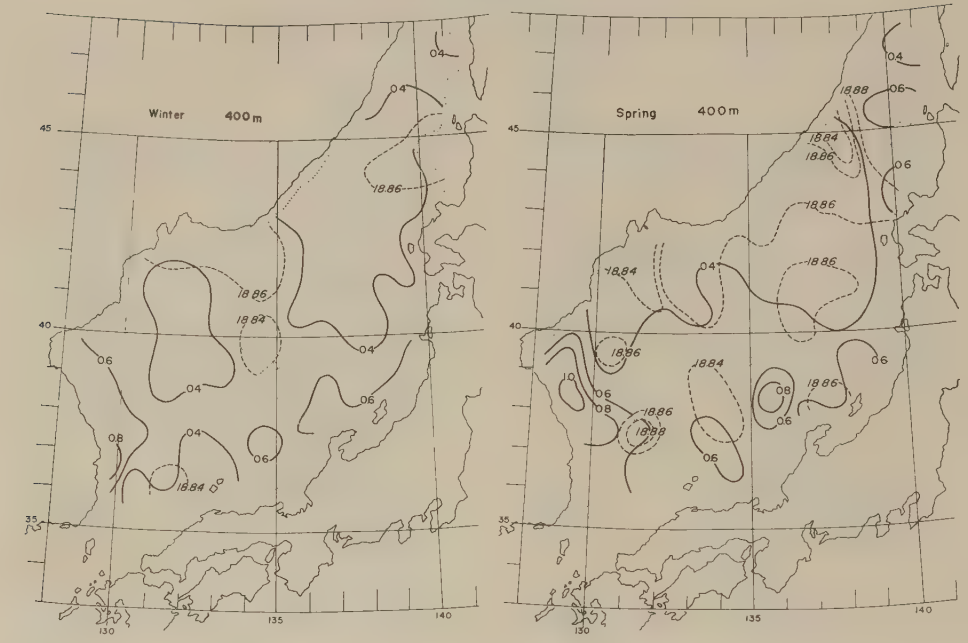
Winter 400m
Spring 400m
45
40
35
130
135
140

Fig. 3. (a) (b)

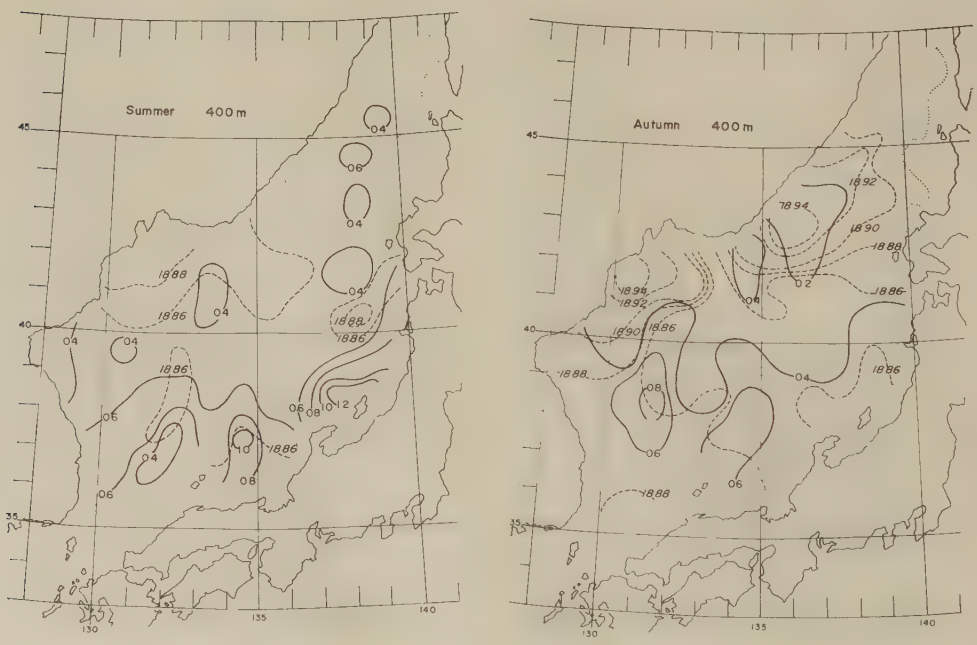
Summer 400m
Autumn 400m
45
40
35
130
135
140

(c) (d)

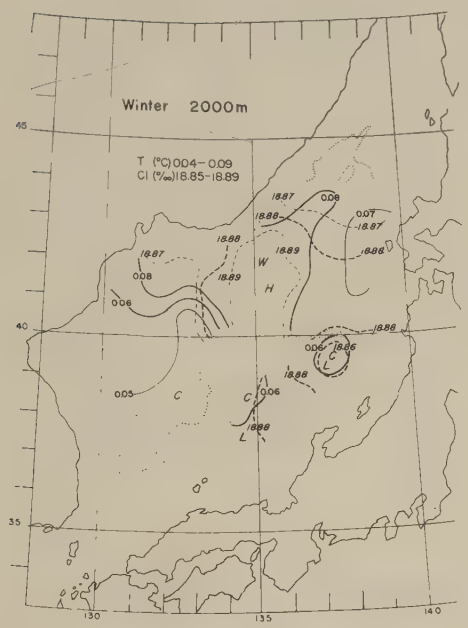
Winter 2000m
T (°C) 0.04–0.09
Cl (‰) 18.85–18.89

(a)

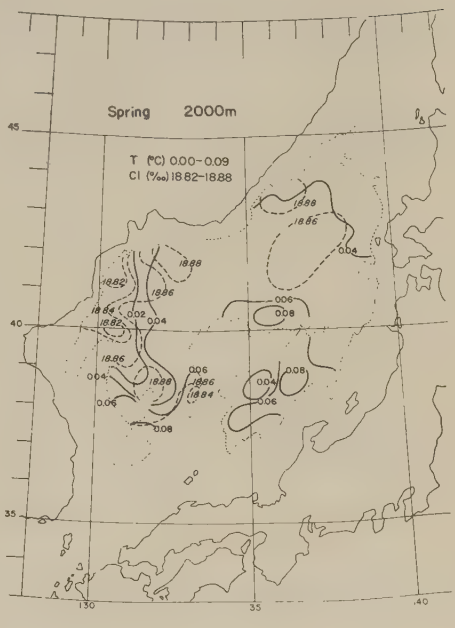
Spring 2000m
T (°C) 0.00–0.09
Cl (‰) 18.82–18.88

(b)

Fig. 4.

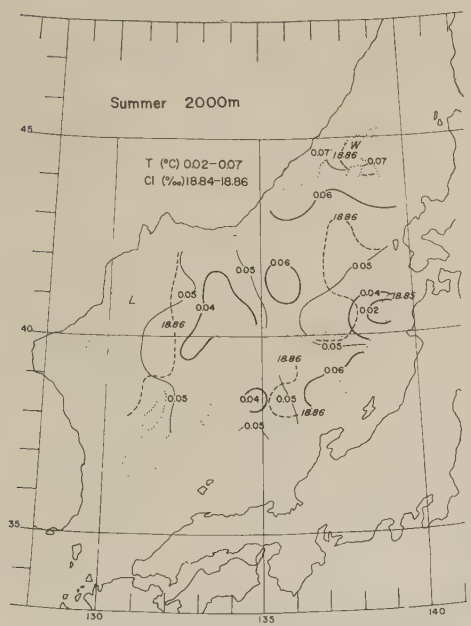
Summer 2000m
T (°C) 0.02–0.07
Cl (‰) 18.84–18.86

(c)

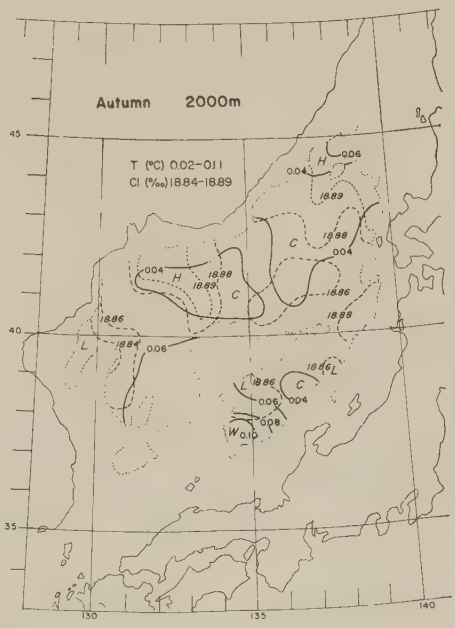
Autumn 2000m
T (°C) 0.02–0.11
Cl (‰) 18.84–18.89

(d)

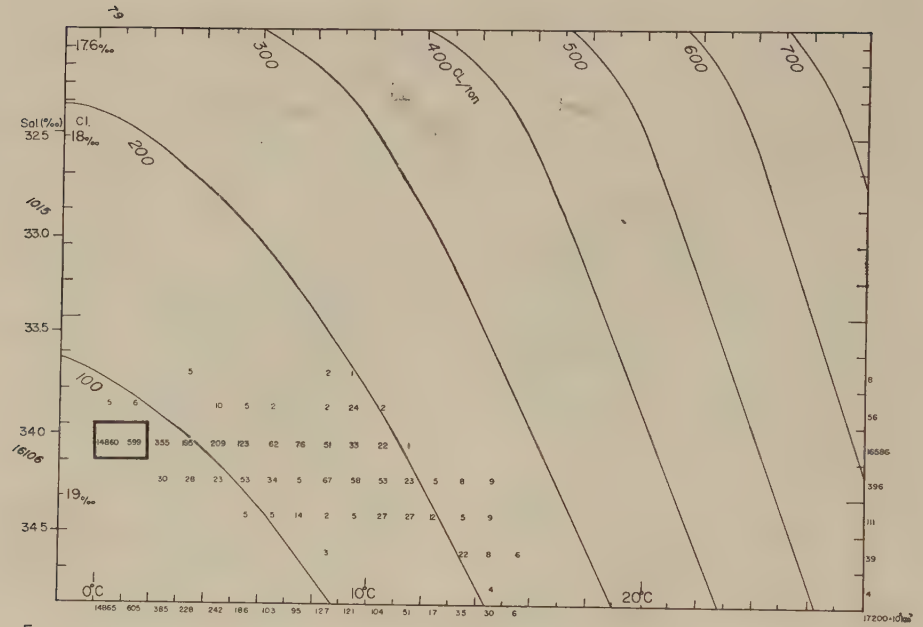
17.6‰
300
400 Cl/ton
500
600
700
Sal (‰) Cl.
32.5 18‰
200
33.0
33.5
100
34.0
19‰
34.5
0°C
10°C
20°C

Fig. 5. (a)

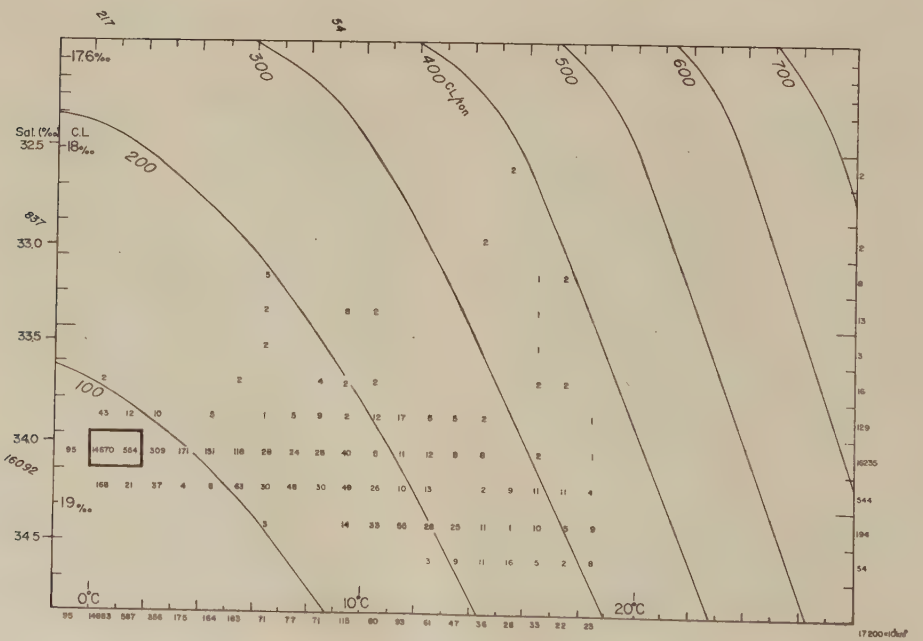
17.6‰
300
400 Cl/ton
500
600
700
Sal (‰) Cl.
32.5 18‰
200
33.0
33.5
100
34.0
19‰
34.5
0°C
10°C
20°C

(b)

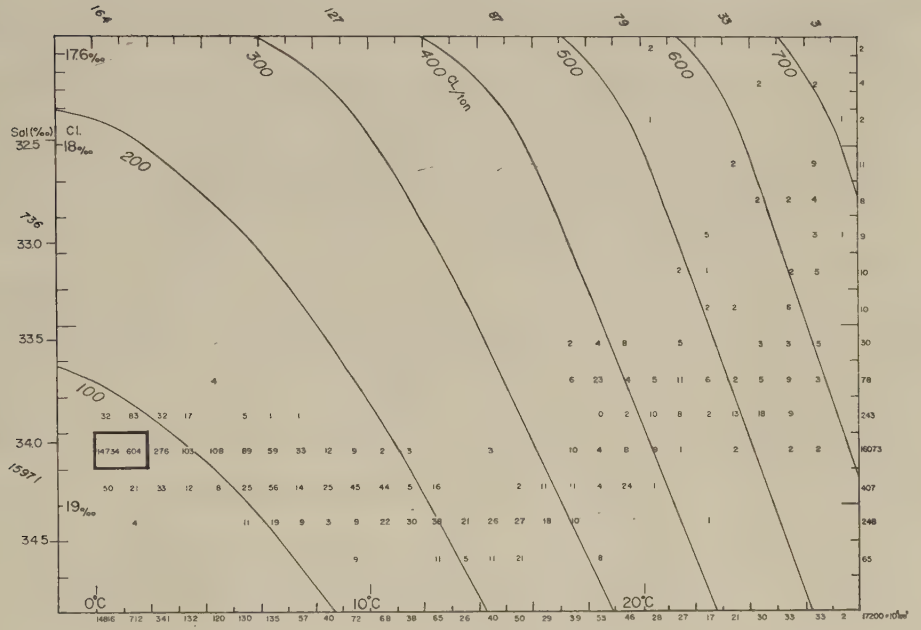
176‰
300
400 Cl/ton
500
600
700
Sal(‰)
Cl.
32.5
18‰
200
33.0
33.5
100
34.0
19‰
34.5
0°C
10°C
20°C

(c)

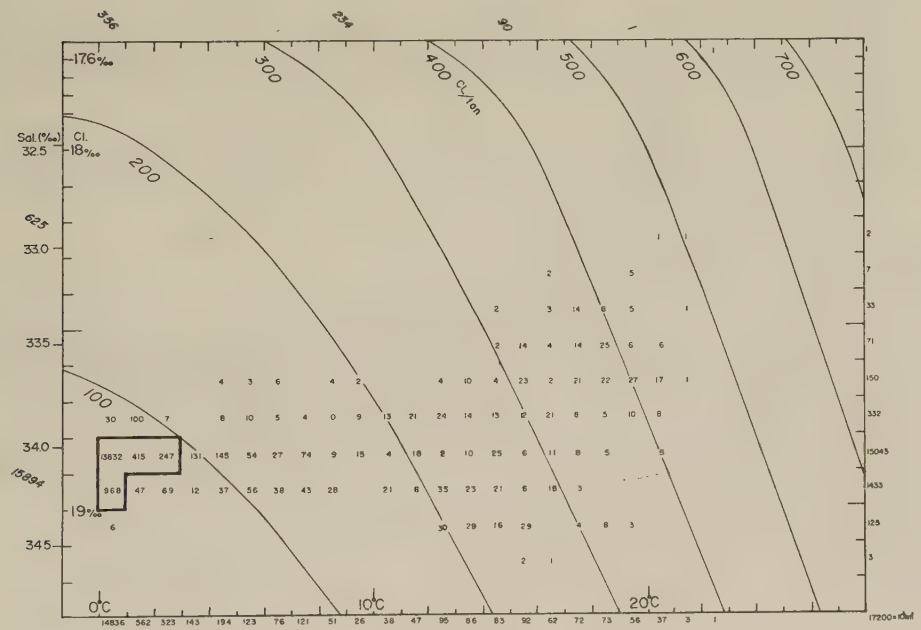
176‰
300
400 Cl/ton
500
600
700
Sal(‰)
Cl.
32.5
18‰
200
33.0
33.5
100
34.0
19‰
34.5
0°C
10°C
20°C

(d)

Fig. 1-a. Surface in winter. The minimum temperature area colder than 2°C appears along the Siberian coast and the low chlorinity water spreads over zonally between 39°N and 43°N.

Fig. 1-b. Surface in spring. In the area of the Tsushima Warm Current along the coast of Honshu water temperatures are about 6°C warmer than in winter.

Fig. 1-c. Surface in summer. Increase in the temperature is remarkable, while heavy precipitation in the rainy season results in decrease in the chlorinity in coastal areas. The zonal area with lower chlorinity in the other seasons disappears.

Fig. 1-d. Surface in autumn. The less saline zone lower than 18.6‰ appears again between 36°N and 40°N.

Fig. 2-a. 100 m layer in winter. The features of the temperature and chlorinity distribution are similar to those at the surface because of convection, especially in the northern part.

Fig. 2-b. 100 m layer in spring. The area colder than 4°C spreads farther southward than in winter, while the isohaline line of 19.0‰ to 39°N.

Fig. 2-c. 100 m layer in summer. The warm currents, the Tsushima Warm Current and the East Korea Current, are the most significantly recognized in distributions of warm and saline waters.

Fig. 2-d. 100 m layer in autumn. The area of waters warmer than 6°C and more saline than 18.9‰ is the largest all through a year.

Fig. 3-a. 400 m layer in winter. Water is fairly homogeneous because of convection. The effect of the warm currents can be hardly recognized in layers deeper than this depth.

Fig. 3-b. 400 m layer in spring. The distributions are more complicated than in winter.

Fig. 3-c. 400 m layer in summer. The area of water colder than 0.4°C is minimum in this season.

Fig. 3-d. 400 m layer in autumn. Perfectly isolated water masses more saline than 18.94‰ appear inshore the Siberian coast. They might originate from up-welling by westerly wind which blows strongly in this season, because the watermasses are associated with low temperature below 0.2°C. However, procedures of formation of these waters cannot be traced from these charts.

Fig. 4-a. 2,000 m layer in winter. Numbers of data in the layer are so small that instrumental errors cannot be eliminated by the grid average. The remarkable difference is not recognized in this layer.

Fig. 4-b. 2,000 m layer in spring.

Fig. 4-c. 2,000 m layer in summer.

Fig. 4-d. 2,000 m layer in autumn.

Fig. 5-a. The bivariate distribution of volume among potential temperatures and chlorinities for the entire Japan Sea in winter. Numbers on the diagram give the volume of water in $10^2 km^3$ for each class 1.0°C×0.1‰Cl. Sums at the bottom give the distribution by potential temperature alone, sums at the right by chlorinity alone. The boundary encloses classes comprising 90% of the entire Japan Sea. Potential specific volume anomaly is represented by the curves. Sloping numbers at the top and the left give the volume of water in $10^2 km^3$ for each band 100 cl/ton.

Fig. 5-b. The bivariate distribution in spring.

Fig. 5-c. The bivariate distribution in summer.

Fig. 5-d. The bivariate distribution in autumn.

The temperature and chlorinity charts were obtained for the above mentioned 8 depths for the four seasons. The reproduction of the charts is too voluminous to be shown here, but the copies of them are available from the authors. For example, the charts in 0, 100, 400 and 2,000 m depths are shown as Figs. 1-4 with brief description of characteristics of the distributions. In these figures, isotherms are shown by full lines and isohaline lines are shown by broken lines. In the figure some of contour lines are intentionally not shown to avoid complexity.

Based on these 32 charts, the bivariated distributions of volume among potential temperature and chlorinity for the entire Japan Sea for the four seasons were obtained as Fig. 5 on the coarser-scale diagram and as Fig. 7 on the finer-scale diagram. Totaling up the four diagrams for the four seasons, frequency distributions through a year are shown in Figs. 6 & 8. The entries in the diagrams are volumes in $10^2 km^3$. Thus, the total of the volumes in each class should be the volume of the entire Japan Sea, 1,720,000 km^3, in Fig. 5 and be four times of this amount in Fig. 6.

In the diagrams, various boundaries are entered each of which encloses classes

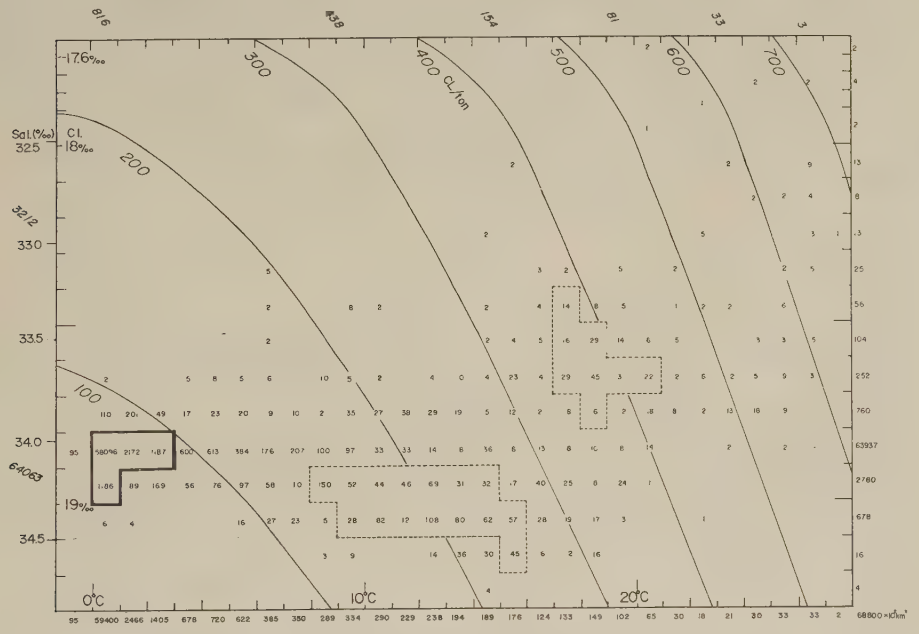

Fig. 6. The bivariate distribution of volume among potential temperatures and chlorinities for the entire Japan Sea all through a year. The volumes in each class are derived by summation of volumes in the four seasons in the same class. The total of these volumes should be four times of the volume of the entire Japan Sea.

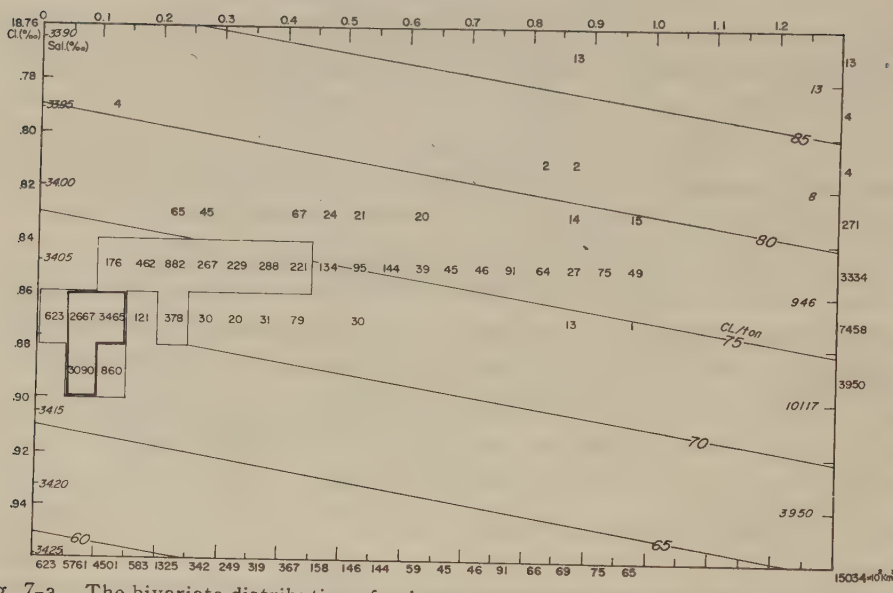

Fig. 7-a. The bivariate distribution of volume among potential temperatures and chlorinities for the water below 1°C in winter. Numbers on the diagram give the volume of water in 10^2km^3 for each class 0.05°C×0.02‰ Cl. Sums at the bottom give the distribution by potential temperature alone, sums at the right by chlorinity alone. The heavy boundary encloses classes comprising 60% of the volume of the entire Japan Sea and the light boundary encloses classes comprising 90%. Potential specific volume anomaly is represented by the curves. Sloping numbers inside the right frame give the volume of water in 10^2km^3 for each band 5 cl/ton.

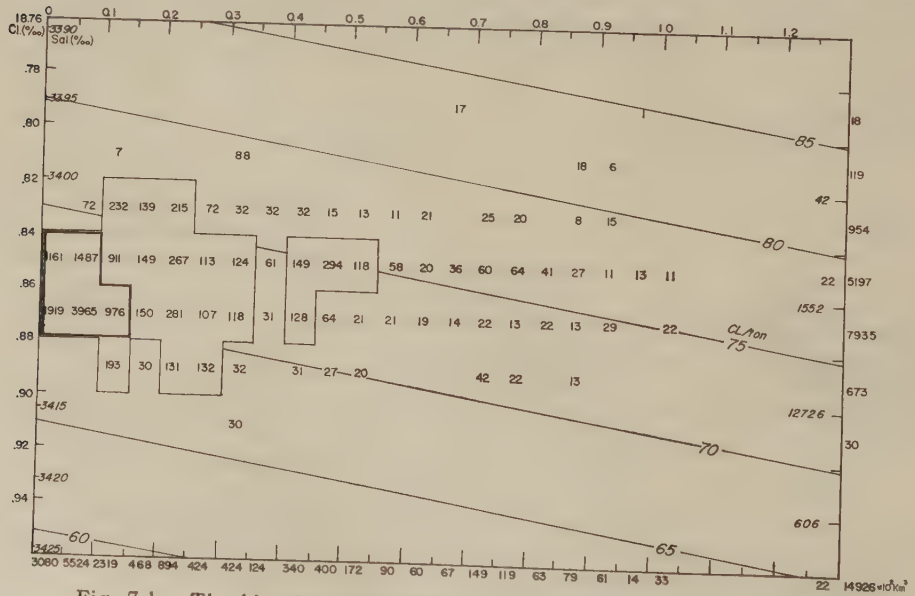

Fig. 7-b. The bivariate distribution for the water below 1°C in spring.

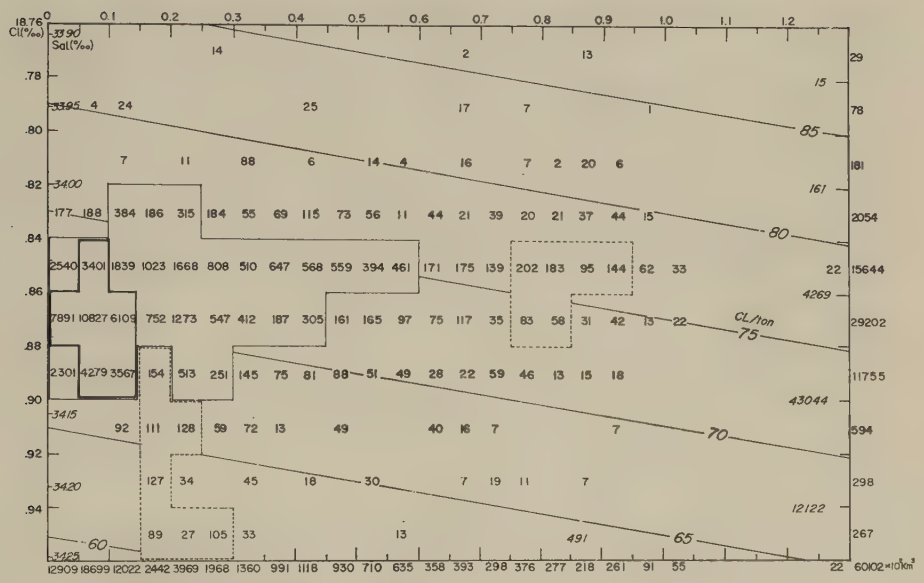

Fig. 7-c. The bivariate distribution for the water below 1°C in summer.

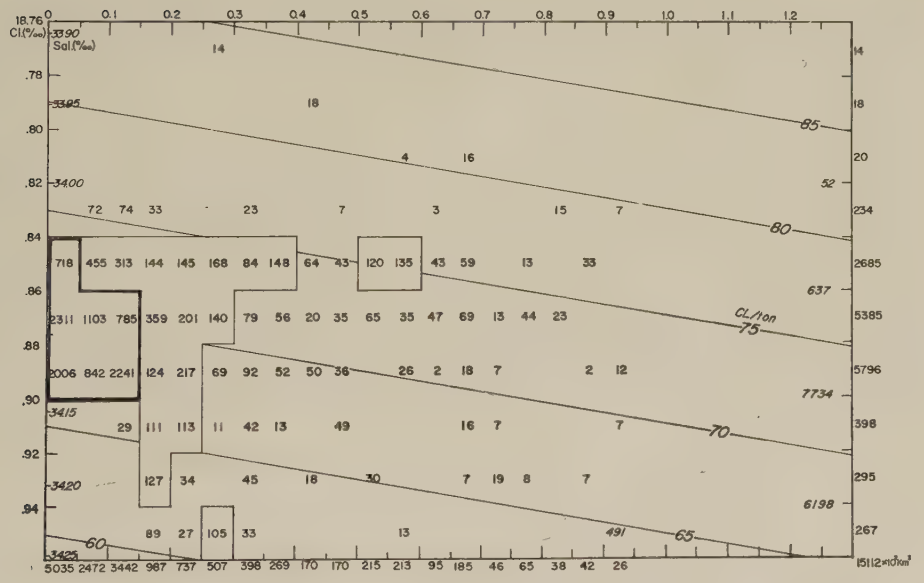

Fig. 7-d. The bivariate distribution for the water below 1°C in autumn.

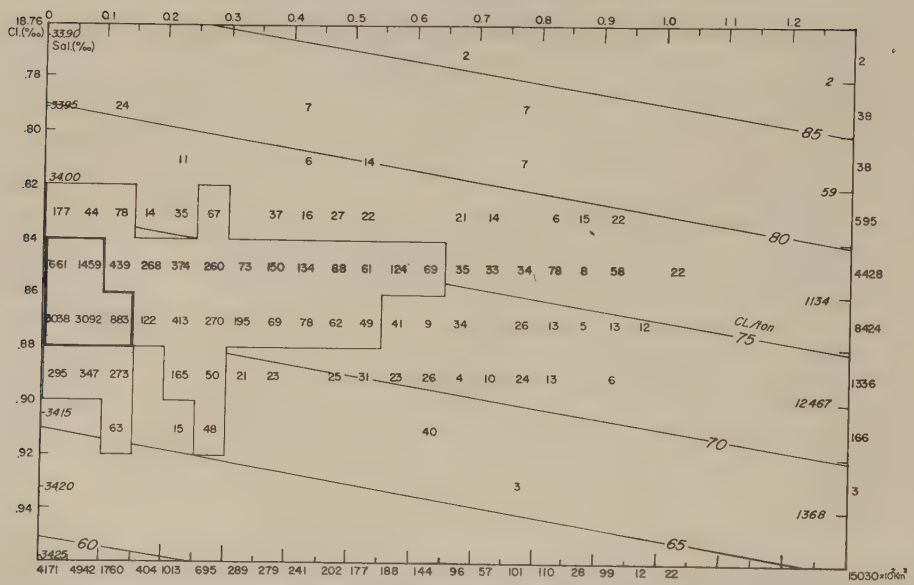

Fig. 8. The bivariate distribution of volume among potential temperatures and chlorinities for the water below 1°C in the Japan Sea all through a year. The volumes in each class are derived by summation of volumes in the four seasons in the same class. The total of these volumes should be four times of the volume of the entire Japan Sea.

whose combined volume just exceeds a stated proportion of the total volume of the Japan Sea. Potential specific volume anomaly is also represented in the diagrams.

3. Discussion

One interesting point emerges, and this is the concentration of T-Cl values around 0.5°C and 18.85‰Cl; 84 per-cent of the entire water mass has a characteristic between 0° and 1°C and between 18.80‰ and 18.90‰, only one of the coarser-scale class (Fig. 6). Ninety-per-cent boundary encloses only four clasess. The volume at the gigantic mode shows scarecely the seasonal variation. This water mass was designated as the Japan Sea Proper Water by UDA (1934) and corresponds with what has characteristics of the third mode of COCHRANE's distribution (1958).

The mode is so prominent that it is very hard to find out another modes which should correspond to the Tsushima Warm Current and the Japan Sea Intermediate Water. But, 15 classes between 8° and 17°C and 18.9‰ and 19.2‰Cl may consist the second mode corresponding to the Tsushima Warm Current which flows northward along the coast of Japan. The third mode might be recognized between

17° and 20°C and between 18.4‰ and 18.8‰Cl as the characteristics of the Surface Water in summer, which is affected by the rainy season.

The line connecting the third mode to the first mode through the second mode shows the average T-Cl relationship in the Japan Sea. The water mass between first and the second mode has the characteristics as the transient layer between them. Though it is scattered rather widely and is very small in amount, an another water mass with characteristics between 4° and 10°C and between 18.3‰ and 18.7‰ Cl is recognized at surface layer of the cold current along the Siberian coast in spring.

Comparing the four diagrams for the four seasons, the seasonal variation is prominent only in upper 200 meters water.

To discuss the water characteristics with the first mode, the finer scale diagrams were introduced for the water below 1°C temperature whose volume is 87‰ of the entire volume. Sixty-per-cent of the entire volume falls in 6 classes which are centered at 0.075°C and 18.87‰Cl. This corresponds with the water deeper than 800 m which was designated as the Japan Sea Deep Water by Uda (*loc cit*). The water between the 60% and 90% boundaries is a little warmer and less saline than the Deep Water and appears in the depths between 300 m and 800 m. In the midst of the water at the depth between 400 m and 600 m, the chlorinity shows the minimum and was designated as the Intermediate Water by Miyazaki (1953). A little remarkable concentration is recognized in the areas centered at 0.175°C, 18.93‰Cl and 0.775°C, 18.85‰Cl. The former shows the minimum value of the potential temperature specific volume anomaly and corresponds with water between 300 m and 800 m in seas north of 41°N in autumn, which has supposedly an important role upon the renewal of the Deep Water. The later appears in the central part of the cyclonic circulation of the Japan Sea.

The most remarkable features which are clarified in this paper is the extremely prominent homogeneity of the water characteristics in terms of temperature and chlorinity relationships. The mass exchange between the homogeneous Bottom Water and the Tsushima Warm Current Water and the process in formation of the homogeneous Bottom Water will be the next problems.

Acknowledgement: The authors wish to express their hearty thanks to Prof. Y. Miyake, Tokyo University of Education, Prof. T. Kiba, Kanazawa University, and Dr. S. Aoki, Director of the Observatory, for their constant interest and encouragement. Acknowledgement is also made to the financial support for this

investigation through a grant from the Ministry of Education as a part of the special program for the research of circulation and accumulation of radioactive substances in the Japan Sea.

References

COCHRANE, J. D. (1958): The frequency distribution of water characteristics in the Pacific Ocean. *Deep-Sea Res.*, **5**, 111–127.

FUKUOKA, J. (1962): Characteristics of hydrography of the Japan Sea. In comparison with hydrography of the North Pacific. *Jour. Oceanogr. Soc. Japan, 20th Anniversary Vol.*, 180–188.

FUKUOKA, J. (1965): Hydrography of the adjacent sea (1). The circulation in the Japan Sea. *Jour. Oceanogr. Soc. Japan*, **21**, 95–102.

MIYAZAKI M. (1953); On the water masses of the Japan Sea. *Bull. Hokkaido Regional Fis. Res. Lab.*, **#7**.

MONTGOMERY, R. B. (1958): Water characteristics of Atlantic Ocean and of world ocean. *Deep-Sea Res.*, **5**, 134–148.

SUDA K., K. HIDAKA, Y. MATSUDAIRA & T. TAKAHATA (1930): The results of the oceanographical observation on board R.M.S. Syunpu Maru in the southern part of the Japan Sea in summer of 1928 (part 1). *Jour. Oceanogr.*, **2**, 1–73.

SUDA, K. & K. HIDAKA (1932): The results of oceanographical observations on board Syunpu Maru in the principal part of the Japan Sea in summer of 1930. *Jour. Oceanogr.*, **4**, 1–174.

SVERDRUP H. U., M. W. JOHNSON & R. H. FLEMING (1942): The oceans, their physics, chemistry and general biology. Table 12, Prentice-Hall Inc., New York.

UDA, M. (1934): Result of simultaneous oceanographic investigation in the Japan Sea and its adjacent water during May and June, 1932. Jour. Imp. Fis. Exp. Station **5**. 186–235.

ZENKEWICH, N. L. (1961): Relief of the Japan Sea. *Basic characteristics of geology and oceanography in the Japan Sea*, Oceanogr. Institute, Academy of Sciences, U.S.S.R.

The Oceanographical Magazine
Vol. 19, No. 2, December 1967

Lowering of Heat Flow Probes in the Horizontal Attitude

By

Masashi YASUI and Toshio KISHII

Maizuru Marine Observatory

(Received December 18, 1967)

In measuring the temperature gradient in the sediment in the ocean bottom, the thermistor is now in common use as the sensing element to measure temperature difference. Thermistors commonly change characteristics with time; that is, the constant term in the formulae which represents characteristics between temperature and resistance has usually temporal variations. To eliminate the effect of the temporal variation, the heat flow probe is allowed to remain for a short time in the deep water just above the bottom, under the assumption that the deep water is almost isothermal. The record in the bottom water is regarded as the zero line for the temperature gradient.

In the water deeper than several thousands meters, the vertical temperature gradient is usually almost adiabatic and is of the order of 10^{-6}°C/cm (COCHRANE, 1959). It is quite negligible compared to the geothermal gradient in the bottom sediment which is at least of 10^{-4}°C/cm (VON HERZEN & LANGSETH, 1966). However, larger vertical temperature gradients are reported even in the deep water by several authors (e.g. BODVARSSON *et al.*, 1967). Moreover, it is quite plausible that it will be much greater in shallower seas.

In the shallower seas, thermal disturbances in the water are likely to extend down to the bottom and may be sufficiently great to make heat flow measurements unreliable. However, in the high latitudes, water is cooled down to almost the freezing point at the surface in winter so that it sinks and spreads over the bottom, while the warming process at the surface in summer cannot affect the bottom water temperature. In these areas, heat flow measurements can be made provided the vertical temperature gradient in the water is small enough to establish the zero point of the thermistor bridge.

This note describes a method of establishing the zero of thermistor bridge even in the presence of an appreciable vertical temperature gradient in the water

some 50 meters above the bottom where the instrument is suspended for about 5 min. in order to obtain a zero line from which to measure the vertical temperature gradients when it is lowered later into the bottom mud. If the temperature gradient probe is lowered in the horizontal instead of the vertical attitude, a

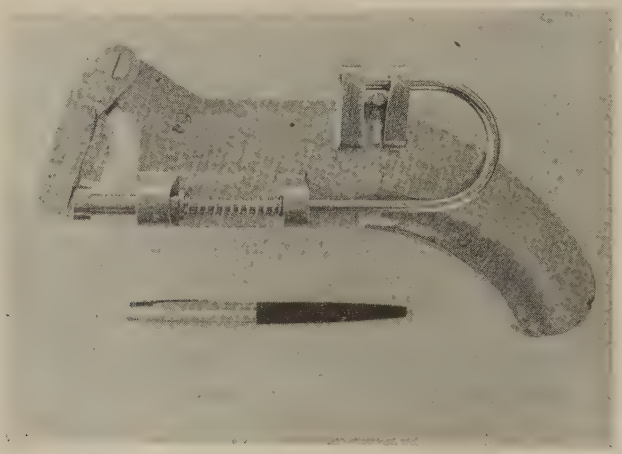

Fig. 1. An elbow release for heat flow probe.

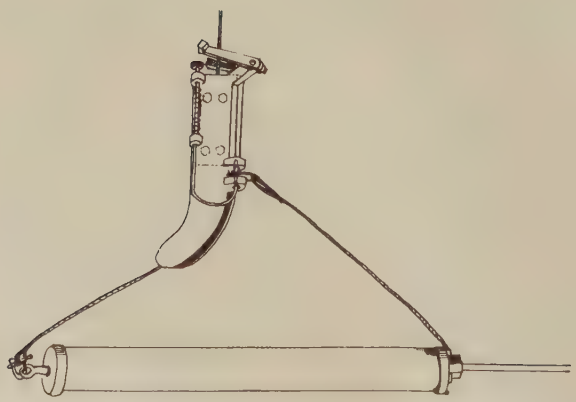

Fig. 2. Heat flow probe suspended in the horizontal attitude with the elbow.

Fig. 3. Heat flow probe tripped into the ordinary vertical attitude.

vertical temperature gradient will not be sensed. This is accomplished by the single mechanism shown on Fig. 1. The pressure case is suspended horizontally by a bridle at the end of the hydrographic cable, as shown on Fig. 2. The line nearest to the probe is hooked to a release which can be tripped by a messenger when it is desired to change the instrument from the horizontal to the customary vertical attitude it must have in order to penetrate into the sediment (Fig. 3). By waiting another 5 min. or so after the instrument is tripped into the vertical position, any vertical temperature gradient in the water can be detected and measured. If it is appreciable, the gradient measurement in the mud can be judged to be less reliable than when there is no observable temperature stratification. An example of procedure and records is shown in Table 1 and Fig. 4.

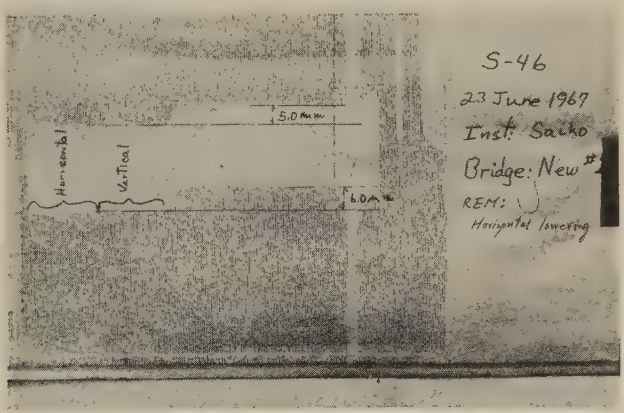

Fig. 4. An example of measurements with the elbow.

Table 1. An example of measurements utilizing the release.

Date: 23 June, 1967.
Station: Saiko-46.
Position: 44° 17′N, 144° 33′E.

Time	Event
02h34m	Launching
02 43	Stop above bottom
02 44	Estimated time of starting record
02 54	Throwing a messenger
02 58	Tripping to vertical
03 13	Start into the bottom
03 14	Bottom contact

Acknowledgement: Support for this was from the Japan Society for Promotion of Science as a part of the US-Japan Cooperative Science Program. Prof. Victor VACQUIER critically read the manuscript.

References

COCHRANE J. D. (1959): Note on the Adiabatic Temperature Gradient of Sea Water. Physical and Chemical Properties of Sea Water. 30-37, *National Academy of Sciences-National Research Council, Pub. #600*, Washington, D. C.

VON HERZEN R. P. & M. G. LANGSETH (1966): Present Status of Oceanic Heat-Flow Measurements. *phys. Chem. Earth*, **6**, 365-407, Pergamon Press, New York.

BODVARSSON G., J. W. BERG, JR., & R. S. MERSECAR (1967): Vertical Temperature Gradient and Eddy Diffusivity above the Ocean Floor in an Area West of the Coast of Oregon. *J. Geophys. Res.*, **72**, 2693-2694.

The Oceanographical Magazine
Vol. 19, No. 2, December 1967

Handy Charger for Oceanographic Instruments

By

Koichi NAGASAKA

Maizuru Marine Observatory

(Received December 18, 1967)

Nowadays electronics is in active use in the oceanographic instrumentation, such as sonar pingers, geothermograd-meters, deep-sea cameras, seismic profilers and radio buoys. Almost all sorts of batteries are used as power sources. Especially alkali-batteries, *e.g.* Ni-Cd batteries, Ni-Fe batteries and Ag-Zn batteries, are getting common for their excellence in characters. To charge there batteries, fairly a lot of chargers is necessary in laboratories. The current and voltage in charging are rather small, so that the more handy charger than ordinary one is preferable for these batteries.

The aim of this note is to present the handy charger which is very convenient to charge small alkali batteries driving small oceanographic instruments.

The ordinary charger consists of the transformer, the rectifier and some resistances. In the newly presented charger, the transformer, which is heavy in weight and fairly large in size, is replaced to the capacitance. The schematic diagram of this charger is shown as Fig. 1. In this circuit, the relationship between the input A. C. voltage $\sqrt{2}E_i \sin \omega t$ and current I_c through the capacitance C is given by the following equations under an assumption of the rectifier being ideal:

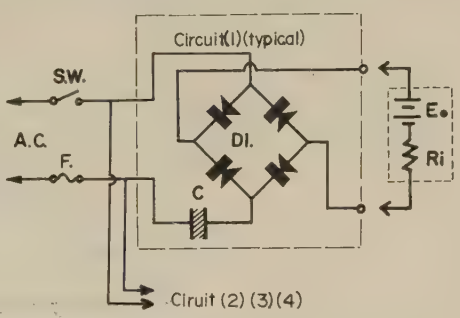

Fig. 1. Circuit diagram of the new handy type charger.
F: Fuse (1A), C: 6μF AC150WV (for AC100v. 60c/s. I_0=0.2A), Di: 1S152×4 (NEC)

$$R_i I_c + \frac{\int I_c dt}{C} = \sqrt{2} E_i \sin \omega t \qquad (E_0 \leqq \sqrt{2} E_i \sin \omega t),$$

$$I_c = 0 \qquad (E_0 > \sqrt{2} E_i \sin \omega t),$$

here, R_i is the internal resistance of a battery and E_0 is terminal voltage of a battery.

Differentiating the equations, the next solutions are obtained,

$$I_c=\begin{cases}\dfrac{\sqrt{2}\,E_i}{\sqrt{R_i^2+\left(\dfrac{1}{\omega C}\right)^2}}\sin\left(\omega t+\tan^{-1}\dfrac{1}{\omega CR_i}\right) & (E_0\leqq\sqrt{2}\,E_i\sin\omega t),\\ 0 & (E_0>\sqrt{2}\,E_i\sin\omega t).\end{cases}$$

As R_i is negligibly smaller than $1/\omega CR_i$ in ordinary batteries, the next relation is derived by averaging the charge current for one cycle;

$$I_0=\overline{|I_c|}\fallingdotseq\frac{2}{\pi}\omega C(\sqrt{2}\,E_i-E_0)$$

In the equation, change of E_0 is so small that I_0 can be regarded as constant for almost all sorts of batteries. This relation is very convenient to charge batteries. A nomograph to compute the capacitance is shown as Fig. 2.

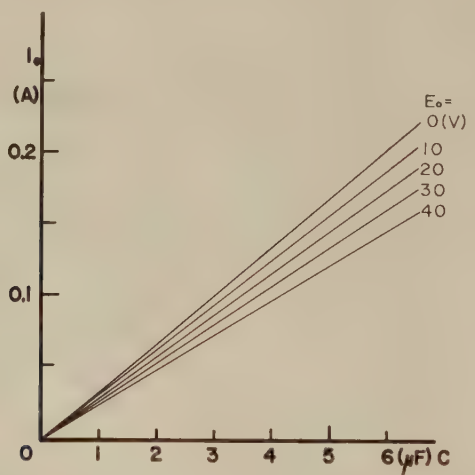

Fig. 2. The nomograph capacity C vs charge current I_0 for various terminal voltage of batteries E_0. Input is 100 V AC 60 c/s.

For an example, a charger for batteries composed with one element Ni-Cd battery, type YUASA F2000 (terminal voltages; 1.25 v, rated charge current; 200 mA) is taken into considerations. The charge current is actually 197 mA for 6 μF capacitance when the input is 60-cycle-100 v-A.C., while the charge current calculated with the nomograph ought to be 201 mA. The difference between the

actual and calculated currents is only 2% and is mainly due to error in the capacitance.

It must be remembered that this sort of the charger cannot be applied to the circuit in which terminals in one side of batteries are commonly connected each other as shown in Fig. 3, because phases of currents in circuits are not the same each other according to the differences of road of circuits.

The charger used in the Observatory and aboard R/V Seifu Maru in charging four sorts of batteries (1×, 4×, 8× and 20×YUASA F2000) is shown in Fig. 4.

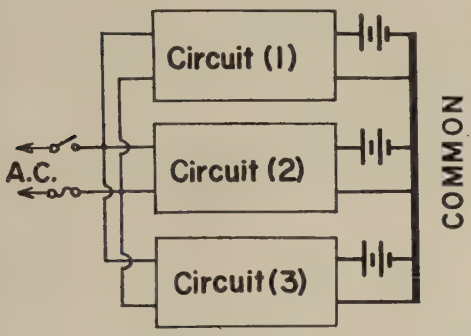

Fig. 3. An example of the wrong connection of batteries with chargers.

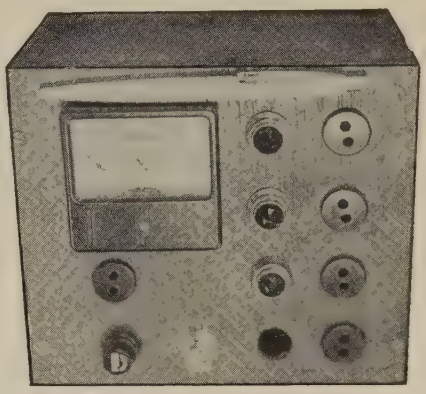

Fig. 4. The picture of the charger.

Acknowledgement: This work was financially supported by a grant from the Japan Society for Promotion of Science as a part of the U.S.-Japan Cooperative Science Program.

The Oceanographical Magazine
Vol. 19, No. 2, December 1967

On the Anomaly of the Sea Surface Temperature in the East China Sea (I)

By

Shigeo Moriyasu

Meteorological Research Institute

(Received December 18, 1967)

Abstract: Spectral analysis is made on the anomaly of ten-day mean sea surface temperature for 2° square in the East China Sea. Based on the results, the distinguished characters of the Kuroshio waters and of the coastal waters are deduced and the extent of two waters are estimated. Though the anomaly is transmitted by advection for the Kuroshio region and by diffusion for the coastal region, other factors' contribution to the transmission is also important for the scale considered here.

1. Introduction

The Nagasaki Marine Observatory has published "The Ten-day Marine Report of the East China Sea" since 1953. The report presents the distribution of the sea surface temperature for individual ten-day. Based on the report, some studies on the monthly mean sea surface temperature have been made. Kikuchi (1959) and Koizumi (1962) discussed the normal conditions and the seasonal variation. And Koizumi (1964) computed standard deviations and discussed their distribution as related with the oceanographic structure.

Robinson (1967) obtained harmonic parameters independently and found a close agreement between Koizumi's and Robinson's results. Therefore, their results show accurately how the monthly mean sea surface temperature for normal conditions changes with season. Standard deviations computed by Koizumi give indicators of variability of anomalies from the normal values, but there are no more detailed informations on the anomalies.

In this report, the anomalies are discussed. The scales of time and of area are important factors for such a treatment and ten days and 2° square are taken as the first step. It is aimed to show the variability of anomalies and their characteristics for individual area and to see the effect of scale on the anomalies as well.

2. *Data and method*

The sea surface temperature at about 140 points are presented for individual ten-day from 1953 to 1962 by the Nagasaki Marine Observatory (1964). The value is read on the sea surface temperature chart for individual ten-day and has some personal error. The chart is constructed on the basis of reports from various ships. Thus, the value is obtained through a kind of smoothing process. This will give some effects on the results shown in the following sections. The first year, 1953, is omitted from the period of statistics, because there are no data at many points.

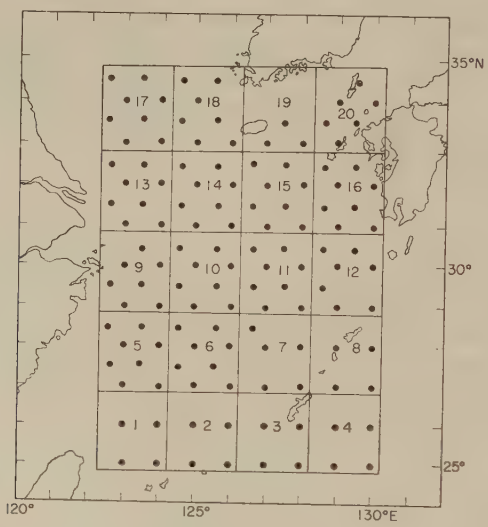

Fig. 1. Location of area and of points for which the ten-day mean sea surface temperature is given. Numerals indicate the area number.

Twenty 2° squares are taken (Fig. 1) and the arithmetic mean of the values at the points in the individual 2° square is taken the value for the square. The normal value is defined as the arithmetic mean of the value for the same ten-day from 1954 to 1962 and the anomaly the deviation from the normal value. Auto- and cross-spectra of the anomalies are computed by using the Tukey's method (Blackman and Tukey, 1958) and Hamming is used for smoothing. The number of samples (n) and the number of the greatest lag (m) are 324 and 36 for individual area, respectively. Then, the number of degrees of freedom is approximately given by

$$\nu=\frac{2n}{m}=18\,.$$

The time interval is 1/36 year and the frequency (f_r) is $\frac{1}{2\times(1/36)}\times\frac{r}{36}=\frac{r}{2}$ cpy (cycles per year), where r is from 0 to 36. For too low and too high frequencies, the results are not significant and the discussion is made for 1 cpy to 9 cpy. The spectral analysis is based on the assumption that the variables belong to a stationary, ergodic and Gaussian process. Areas 17 and 18 have no data for some ten-days and are omitted from the discussion.

3. *Autocorrelation and autospectrum*

Autocorrelation coefficients are computed for numbers of lags up to 36 (Fig. 2). The coefficient decreases rapidly with the number of lag and indicates no

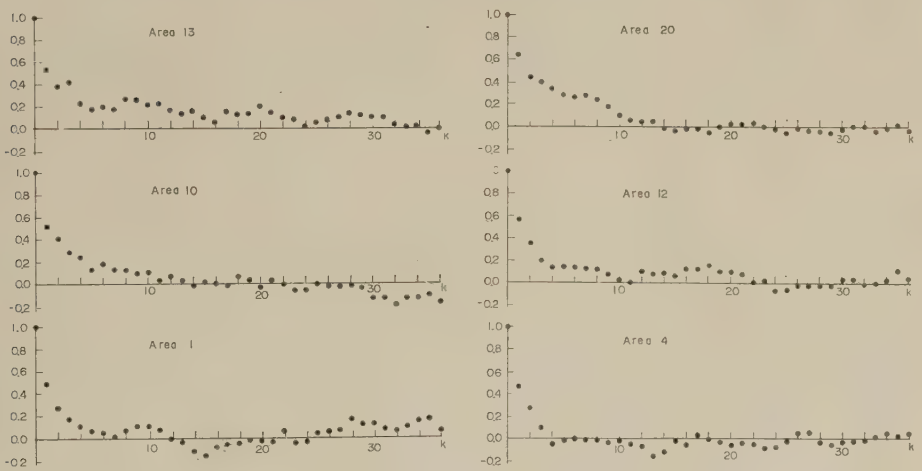

Fig. 2. Autocorrelation coefficient. k is number of lag.

definite periodicity. The decrease of the coefficients is less marked in the northern part, for example, for the number of lag, 3, it is more than 0.4 at Areas 13, 19 and 20 and less than 0.2 at Areas from 1 to 8 and 11. Roden (1962) obtains the average persistence using the standard deviation (σ) of the computed autocorrelation from the true one of an infinite record. It is given by

$$\sigma^2\leqq\frac{4}{T}\int_0^T\phi(t)^2dt\,.$$

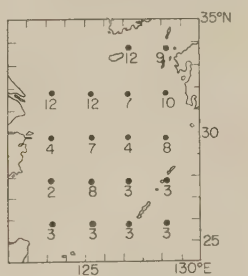

Fig. 3. Average persistence in ten-days.

Here, T is the record length. In the same way, the average persistence is obtained (Fig. 3). The persistence is between 2 and 12 ten-days and longer in the northern part. It is interesting that the anomaly is less persistent in the area where the Kuroshio flows.

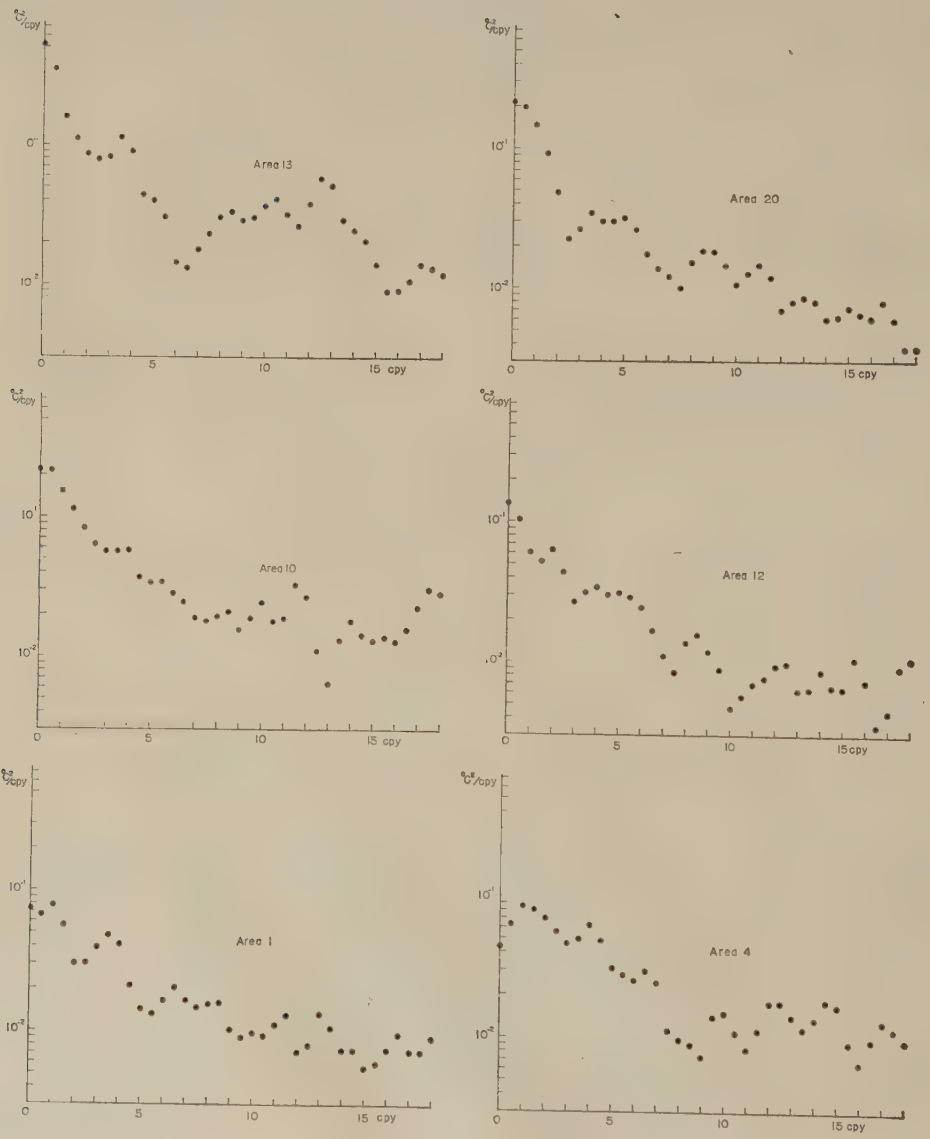

Fig. 4. Autospectrum.

The autospectrum is shown in Fig. 4. There are no marked peaks in the spectrum, that is, no definite periodicities. This is the same as derived from the autocorrelation. Most of the power is concentrated in the low frequency range for the northern part, while the feature is not so clear for the southern part. This supports the longer persistence for the northern part. For Areas 14, 15, 16, 19 and 20, 50% of the total power is contained between 0 cpy and 2 cpy. Though no peaks are found by chi-square test, the power density is a little larger around 3~4 cpy for many areas. It is unknown whether the large power density is physically significant or not. The total power (Fig. 5) is small in the area where the Kuroshio flows, while it is large in the northwestern part where the coastal waters predominate.

Thus, the distinguished features of the anomaly noted above are related with the waters which occupy the area. In other words, it is deduced from the features of the anomaly which waters predominate in the area.

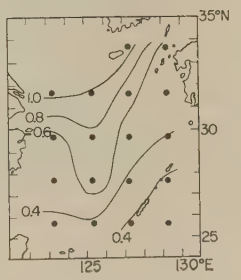

Fig. 5. Total power in $°C^2$.

4. Crosscorrelation and coherence

The crosscorrelation and the crossspectrum are computed between Area 1 and other areas (Case A) and between Area 13 and other areas (Case B). Area 1 is situated at the entrance of the East China Sea for the Kuroshio, while Area 13 is said to be markedly influenced by the coastal waters. Therefore, the results of two computations are expected to show how the Kuroshio waters or the coastal waters give the effects to other areas. Here, the coherence and the phase relation are discussed instead of the cospectrum and the quadraturespectrum.

The crosscorrelation coefficient decreases markedly with the number of lag. But, the distribution is closely related with the hydrographic conditions. For Case A, the coefficient is large in the area where the Kuroshio flows (Fig. 6). For Case B, the coefficient decreases with the increase in the distance from Area 13 (Fig. 7). These features are seen only for small numbers of lag and distinguished by the reference area.

The variation of coherence with frequency is not regular. The distribution of the coherence for individual frequncy is related with hydrographic conditions and shows the effects of the Kuroshio waters or the coastal waters. Roden (1962) uses the approximate 95% confidence limit of coherence, $2\nu^{-1/2}$. For the present case, its value is about 0.42 and it is defined that there is no correlation for the

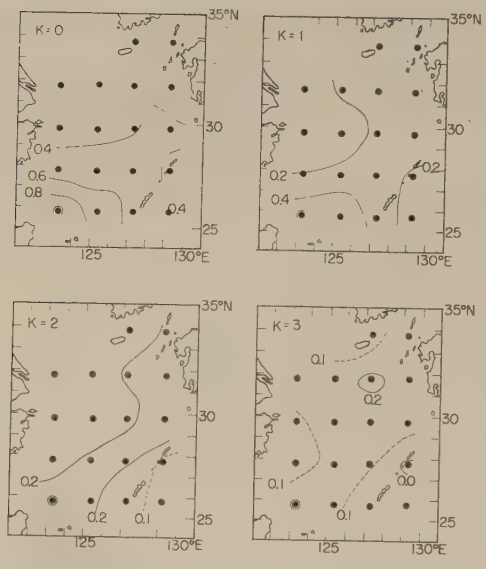

Fig. 6. Crosscorrelation coefficient for Case A (the reference area is Area 1). k is number of lag.

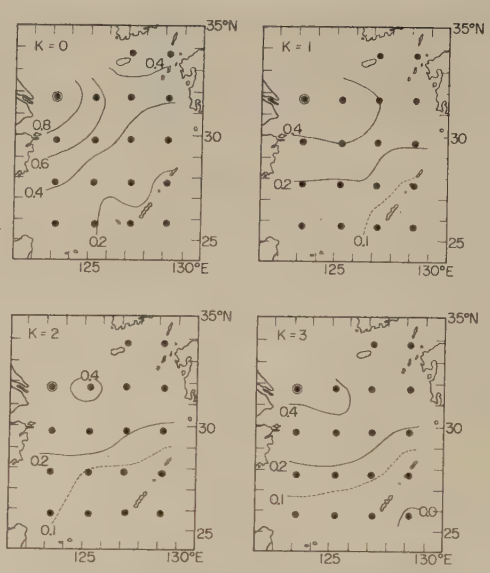

Fig. 7. Crosscorrelation coefficient for Case B (the reference area is Area 13). k is number of lag.

coherence less than 0.42. The area of no coherence increases with frequency, that is, the fluctuation of small scale is not transmitted to distant areas. This is the natural result to be expected. If the anomaly is produced at the reference area and is transmitted to other areas by advection or diffusion, the lag must increase with the distance from the reference area and the anomaly at the reference area must lead those at other areas at least. But, the computed phase does not show such distributions for many areas. This means that the assumption is not fulfilled in this case. Next, some descriptions should be made on Cases A and B.

The coherence for Case A is shown in Fig. 8. The Kuroshio flows through Area 1 into the East China Sea and runs northeastward. During the travel the Kuroshio waters are mixed with the coastal waters in the northwestern part and the character is modified. Therefore, the coherence is expected to be large near the axis of the Kuroshio and to decrease with the distance from Area 1. These features are clear for most frequencies. The area of no correlation, in general, is seen in the northern and the western parts and extends southwestward with the frequency, except for 3.5 cpy. The area of no correlation is seen west of Ryukyu Islands for high frequencies. This indicates that the fluctuation of small

scale at Area 1 does not reach the areas which are situated out of the course of the Kuroshio. The Tsushima Current is a branch of the Kuroshio and runs northward to the west of Kyushu. Accordingly, the anomaly in the area west of Kyushu is expected to be influenced by the anomaly in the southern part. But, the obtained results do not support the expectance for most frequencies. This is perhaps brought about by more effective factors other than advection, for example, the modification caused by mixing with the coastal waters during the long travel from Area 1. If the anomaly is transferred by advection,

$$\frac{\partial \theta}{\partial t}+u\frac{\partial \theta}{\partial x}=0.$$

θ is the anomaly, t is time, u is current speed (assumed constant) and x is the distance from the reference area. The solution is

$$\theta=\theta_0 e^{i2\pi f\left(t-\frac{x}{u}\right)}$$

with the boundary condition at the reference area ($x=0$)

$$\theta=\theta_0 e^{i2\pi ft}.$$

Here, f is frequency. Therefore, the phase lag is proportional to the distance from the reference area. The autospectrum of the anomaly is given by

$$S_x(f)=S_0(f)$$

where $S_0(f)$ is the spectrum for the reference area. Namely, the spectrum is independent of the distance from the reference area. Generally, the obtained distribution of phase is not reasonable if only the effect of advection is considered. But, there are some good examples for presenting the effect of advection. The phase for 2.0 cpy is taken. The phase lag increases northward along the course of the Kuroshio and of the Tsushima Current and the rate of the increases is larger in the Tsushima Current region than in the Kuroshio region. The current speed obtained by the method of least squares is about 50 cm/sec for Areas 1—7—12 and about 15 cm/sec for Areas 12—16—20. This estimation is made on the assumption that the phase lag is proportional to the distance from Area 1 or Area 12 and gives reasonable values of current speed for the Kuroshio and the Tsushima Current. The autospectra for these areas are not equal and this contradicts the expectance that the anomaly transferred by advection.

The coherence for Case B is shown in Fig. 9. They say that the coastal waters go southward along the coast of China and that they extend southeastward

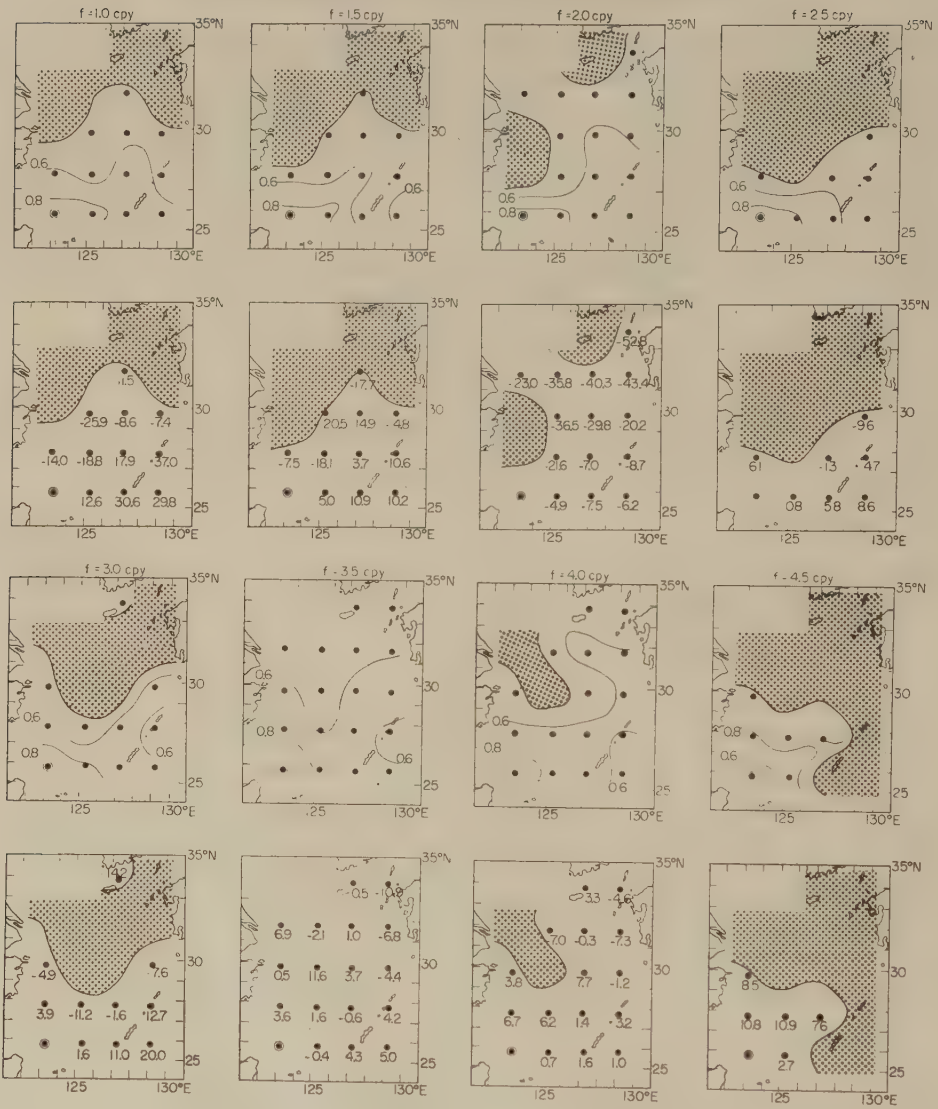

Fig. 8. Coherence (upper) and phase lead in days (lower) for Case A. Dotted part has no correlation.

by diffusion or advection. The distribution of coherence show the characteristic feature. The coherence decreases with the increase in the distance from Area 13 and almost independently of the direction from Area 13. Thus, the anomaly at Area 13 is transmitted in nearly the same way in all directions. The area of no correlation increases with the frequency and the increase is more marked than

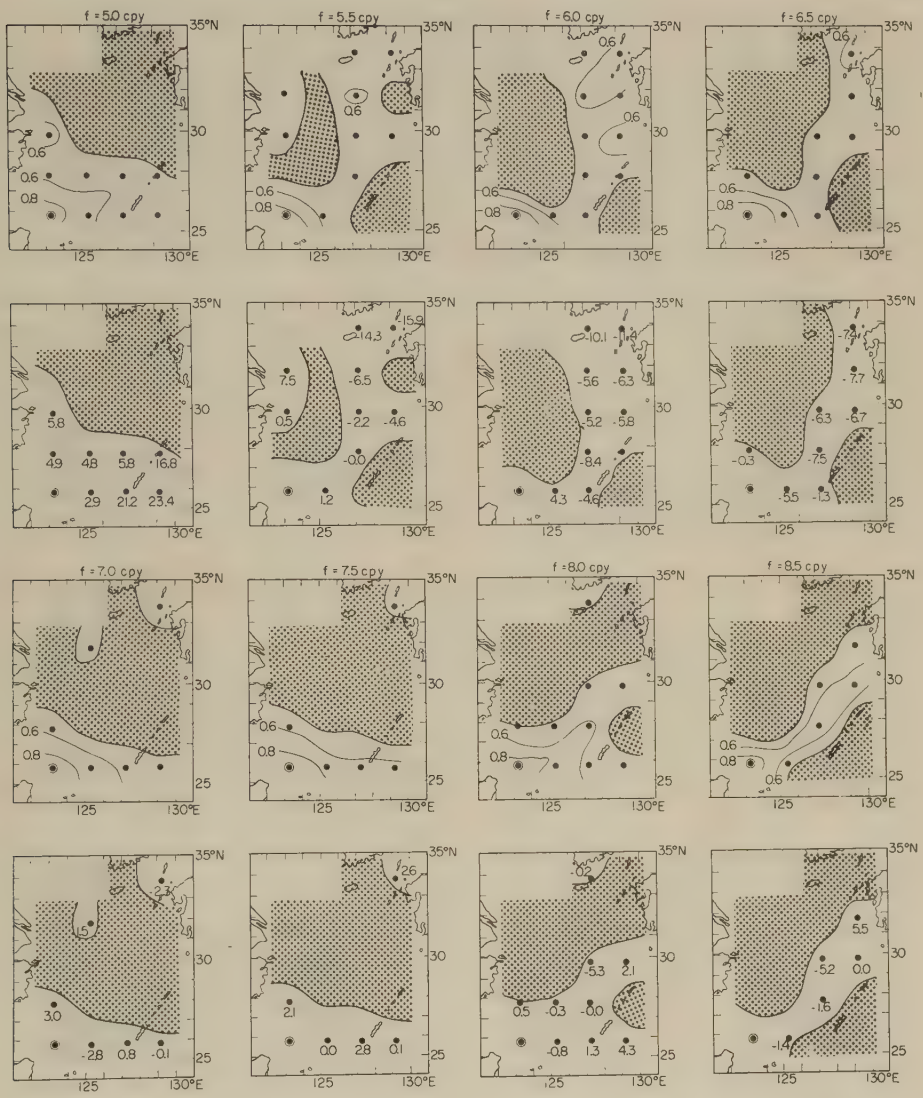

for Case A. The southeastern part, the Kuroshio region, has no correlation for almost all frequencies. The Tsushima Current region west of Kyushu has correlation for low frequencies and not for high frequencies. The distribution of phase does not support the feature noted above. If the anomaly is transmitted by diffusion,

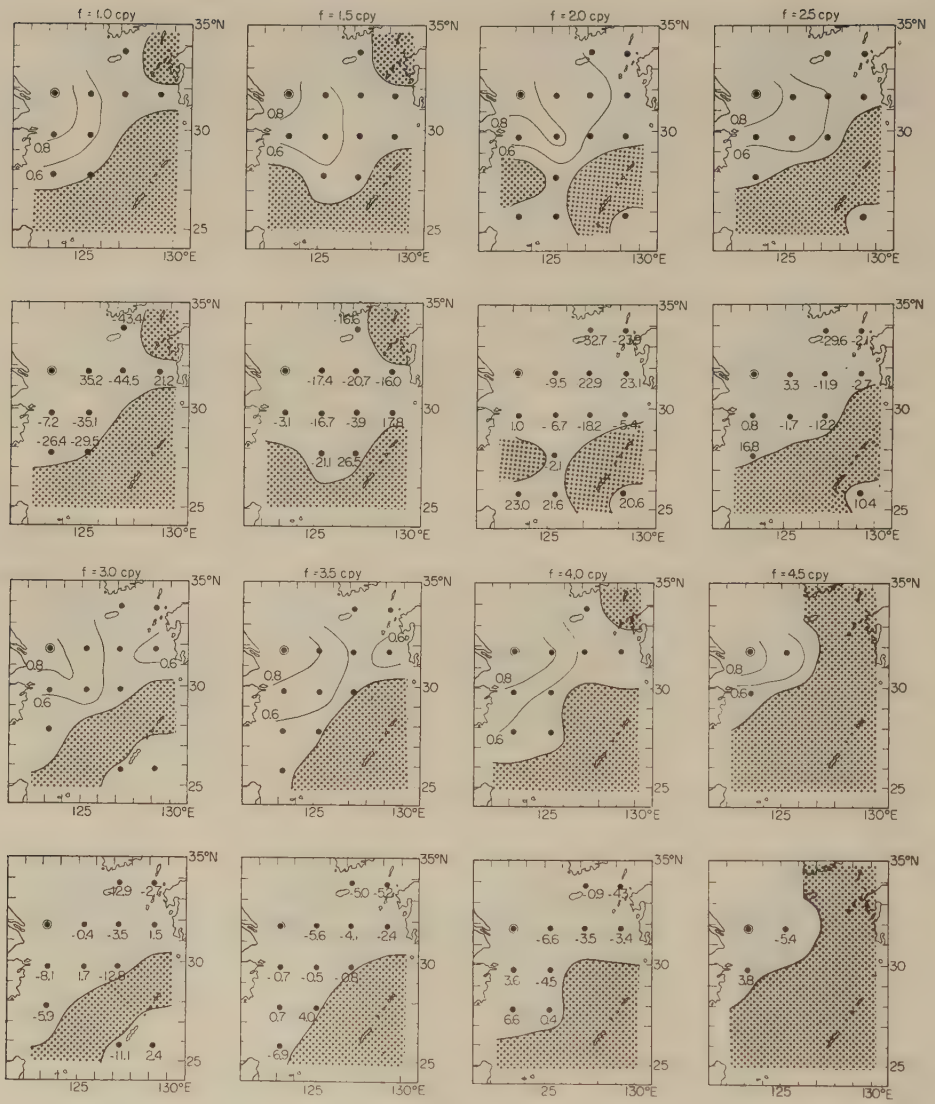

Fig. 9. Coherence (upper) and phase lead in days (lower) for Case B. Dotted part has no correlation.

$$\frac{\partial \theta}{\partial t} = K \frac{\partial^2 \theta}{\partial x^2} .$$

θ is the anomaly, t is time, K is diffusion coefficient (assumed constant) and x is the distance from the reference area. The solution is

$$\theta = \theta_0 e^{px + i(2\pi ft - px)}$$

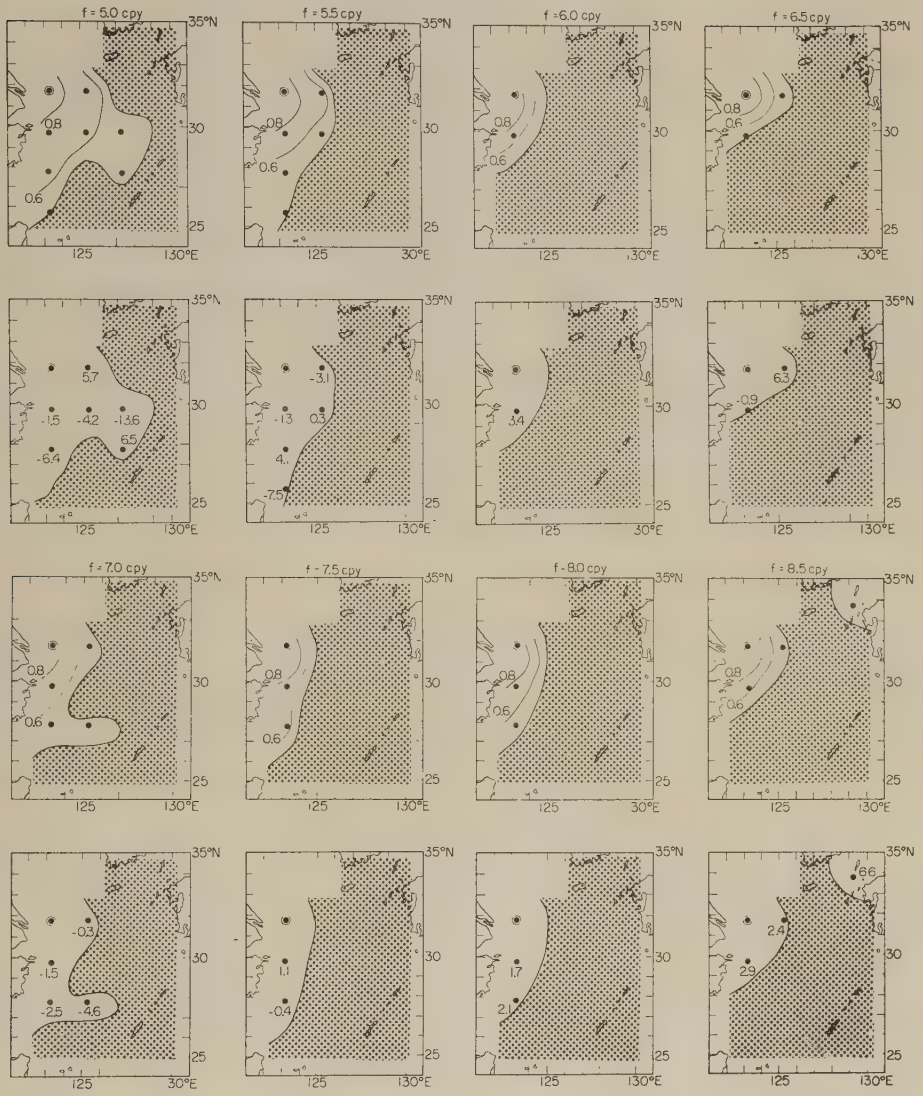

with the boundary condition at the reference area ($x=0$)

$$\theta=\theta_0 e^{i2\pi ft}.$$

Here, f is frequency and $p=\sqrt{\pi f/K}$. Therefore, the pase lag is proportional to the distance from the reference area. The autospectrum of the anomaly is given by

$$S_x(f)=e^{-2px}S_0(f),$$

where $S_0(f)$ is the autospectrum for the reference area. Therefore, the spectrum must decrease exponentially with the distance from the reference area. For 2.0 cpy, the relation of phase is nearly satisfied for Areas 13-14-15. From the increase of the phase, $K=5.4\times10^8$ c.g.s. is obtained by the method of least squares. For this frequency, the relation of phase is nearly satisfied and a reasonable value of diffusion coefficient is obtained, while the distribution of the spectrum gives too large diffusion coefficient the order of which is 10^{11} c.g.s. For other frequencies, the fitting to the assumption is not better.

As described above, the distribution of coherence has the distinguished features for two cases and they are expected to be derived from the oceanographic conditions, while the distribution of phase lag does not support the features. One of the reasons is that the anomalies for two reference areas give the combined effect to the anomaly for individual area.

5. *Partial coherence*

The anomaly may be considered to be influenced by the anomalies at two reference areas. For such a two-input linear system, it is useful to use partial coherence (Bendat and Piersol, 1966). Partial coherence indicates the effect of one of two inputs just like partial correlation coefficient.

For Case A, the effect of the anomaly at Area 1 is taken and that at Area 13 is removed. The distribution is shown in Fig. 10. Generally, the features described in the previous section are clearer and the area of no correlation is larger. The distribution of phase lag is not suitable to show the process of advection.

For Case B, the effect of the anomaly at Area 13 is taken and that at Area 1 is removed. The distribution is shown in Fig. 11. The concentric distribution of partial coherence is distinguished and the distribution of phase lag does not show the diffusion process.

Theoretically, the partial coherence is a better indicator presenting the effect of the reference area. But, no better deductions are obtained from the distribution of partial coherence and of phase lag. This means that the transmission of the anomaly is not made mainly by advection or diffusion. The anomaly is changed under the combined influence of advection, diffusion and external factors such as radiation, heat exchange between air and sea and so on. Furthermore, the scale of the area may be too large to discuss the phenomenon.

Now, it is possible to determine how far the effect of the reference area is transmitted. A trial is made based on the value of partial coherence. In Fig. 12, the area is divided into four groups:

A correlated with Area 1 and not with Area 13
B correlated with Area 13 and not with Area 1
C correlated with both Area 1 and Area 13
D correlated with neither Area 1 nor Area 13.

In the previous section, it is noted that the anomaly at the reference area is not transmitted to distant areas for high frequencies. This is very clear from Fig. 12. The area of Group D is hardly seen for the frequencies less than or equal to 4.0 cpy. The area of Group A is in the Kuroshio region. The area of Group B is in the northwestern part. The area of Group C is small for high frequencies and is found between the area of Group A and the area of Group B. These features are general ones and some irregularities are seen for individual frequency. Next, it is shown where each group is predominant on an average from 1.0 cpy (f_1) to 8.5 cpy (f_{16}). The number of each group for individual area is easily obtained and may be taken the index for the group. For Area 11, numbers of Groups A, B, C and D are 7, 3, 3 and 3, respectively, and these numbers are indexes for the groups. This representation gives too much weight to the fluctuation of smaller scale and a correction is necessary to see the average pattern. As $f=1/T$ (T is period),

$$\Delta T=-\frac{\Delta f}{f^2}$$

is obtained and the range of period (ΔT) corresponding to unit range of frequency (Δf) is in inverse proportion to f^2. Hence, it is reasonable to take the weight $1/f^2$. If the area belongs to a group for frequencies, f_i, f_j and f_k, the index for the group is given by

$$\left(\frac{1}{f_i^2}+\frac{1}{f_j^2}+\frac{1}{f_k^2}\right)\times\frac{100}{\sum_{n=1}^{16}(1/f_n^2)}$$

where $\sum_{n=1}^{16}(1/f_n^2)$ is equal to 2.351. The index is between 0 and 100. If the index for the group is 100, it means that the area belongs to the group for all frequencies. The index for individual group is shown in Fig. 13. Group A is predominant in the southeastern part and Group B is restricted in the northwestern part and its extension is very small. Group C is centered at Area 9 and Group D is in the northeastern part where the Tsushima Current flows. In

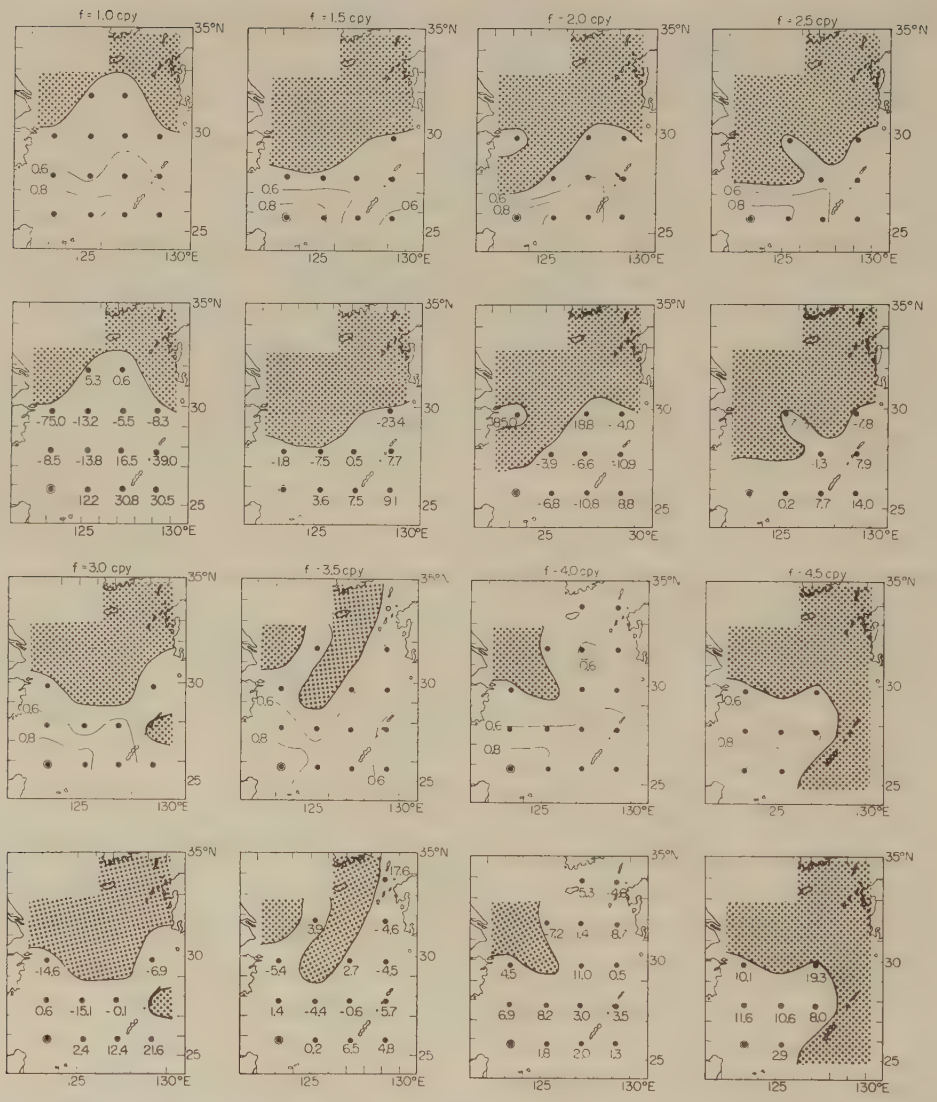

Fig. 10. Partial coherence (upper) and phase lead in days (lower) for Case A. Dotted part has no correlation.

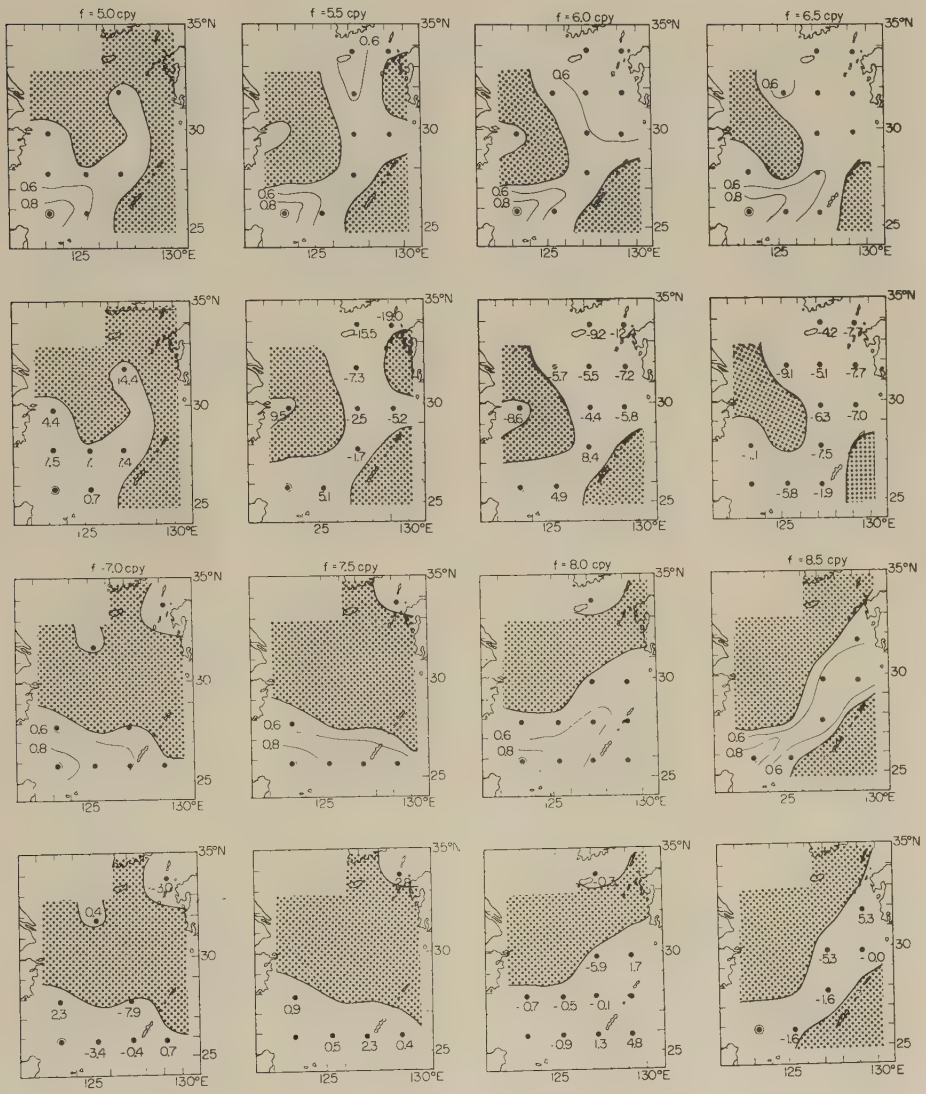
f = 5.0 cpy
f = 5.5 cpy
f = 6.0 cpy
f = 6.5 cpy
f = 7.0 cpy
f = 7.5 cpy
f = 8.0 cpy
f = 8.5 cpy
35°N
30
25
125
130°E

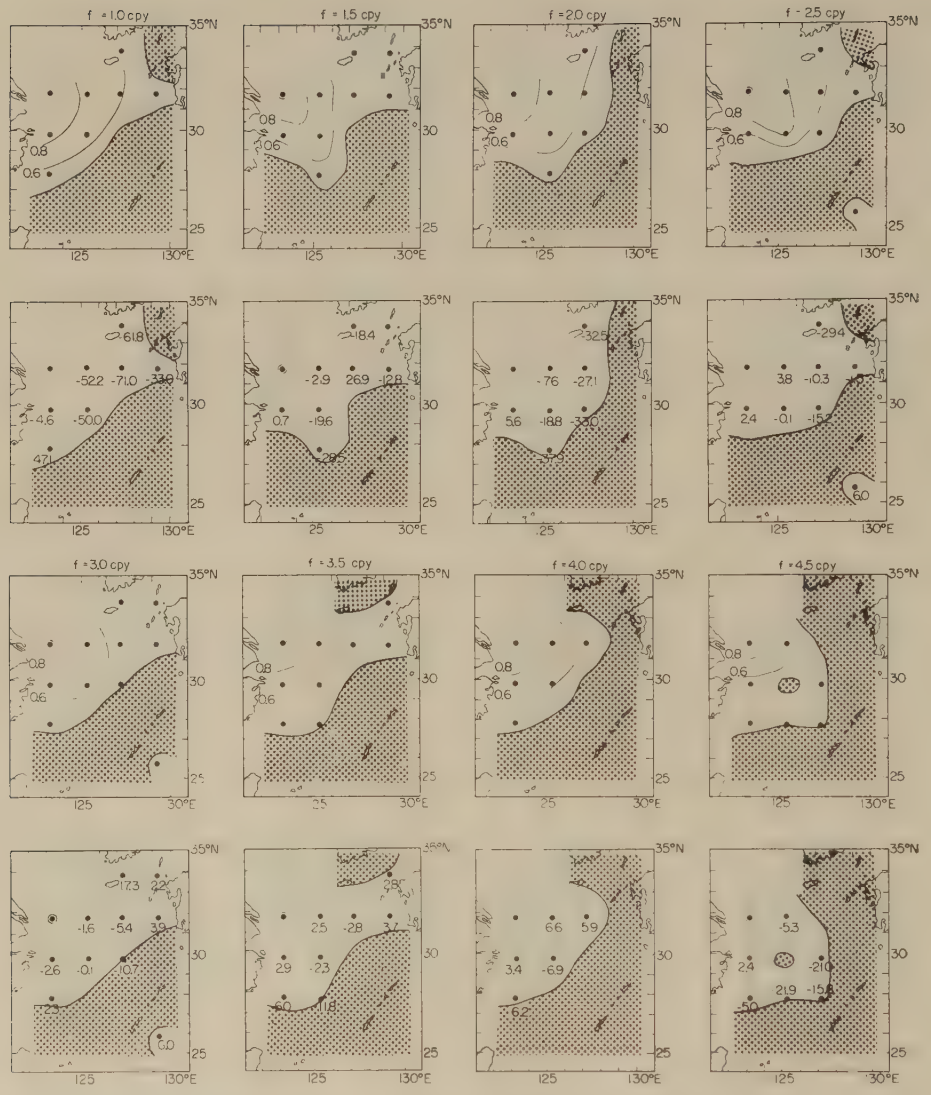

Fig. 11. Partial coherence (upper) and phase lead in days (lower) for Case B. Dotted part has no correlation.

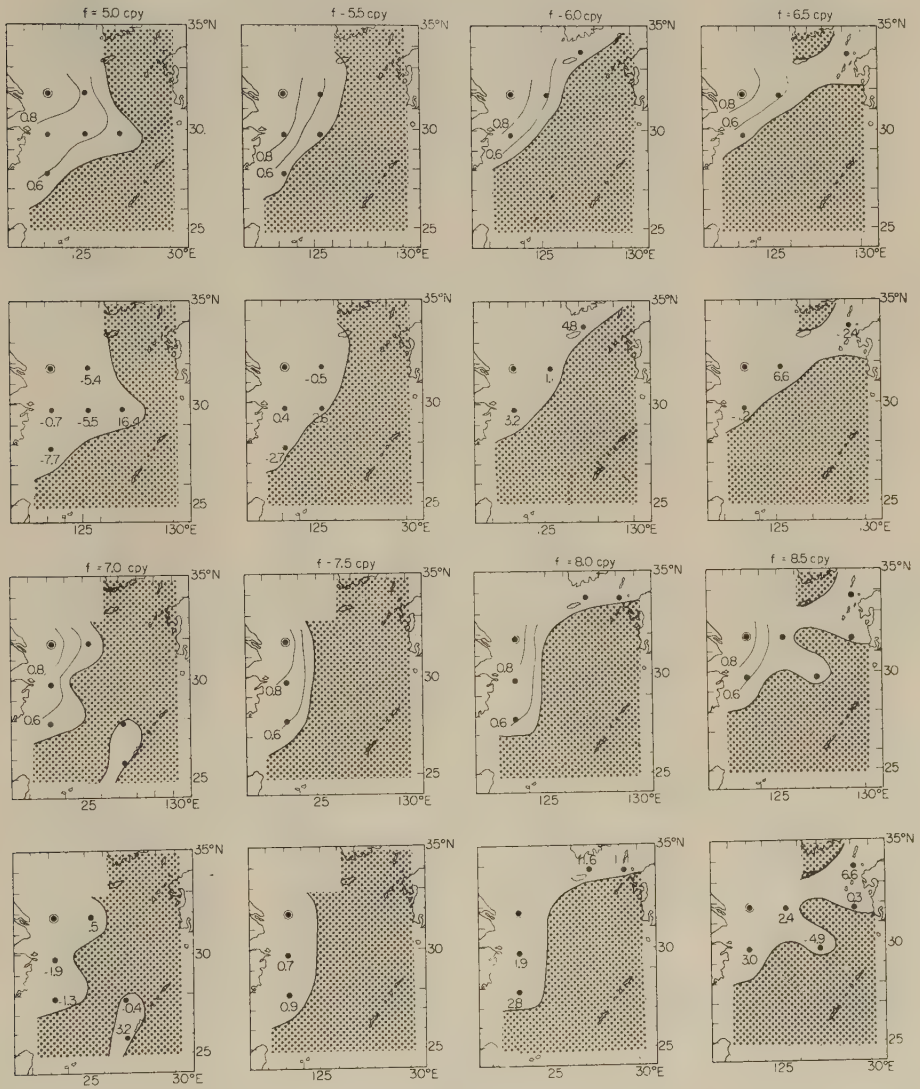
f = 5.0 cpy
f - 5.5 cpy
f - 6.0 cpy
f = 6.5 cpy
f = 7.0 cpy
f - 7.5 cpy
f = 8.0 cpy
f = 8.5 cpy
35°N
30
25
125
130°E

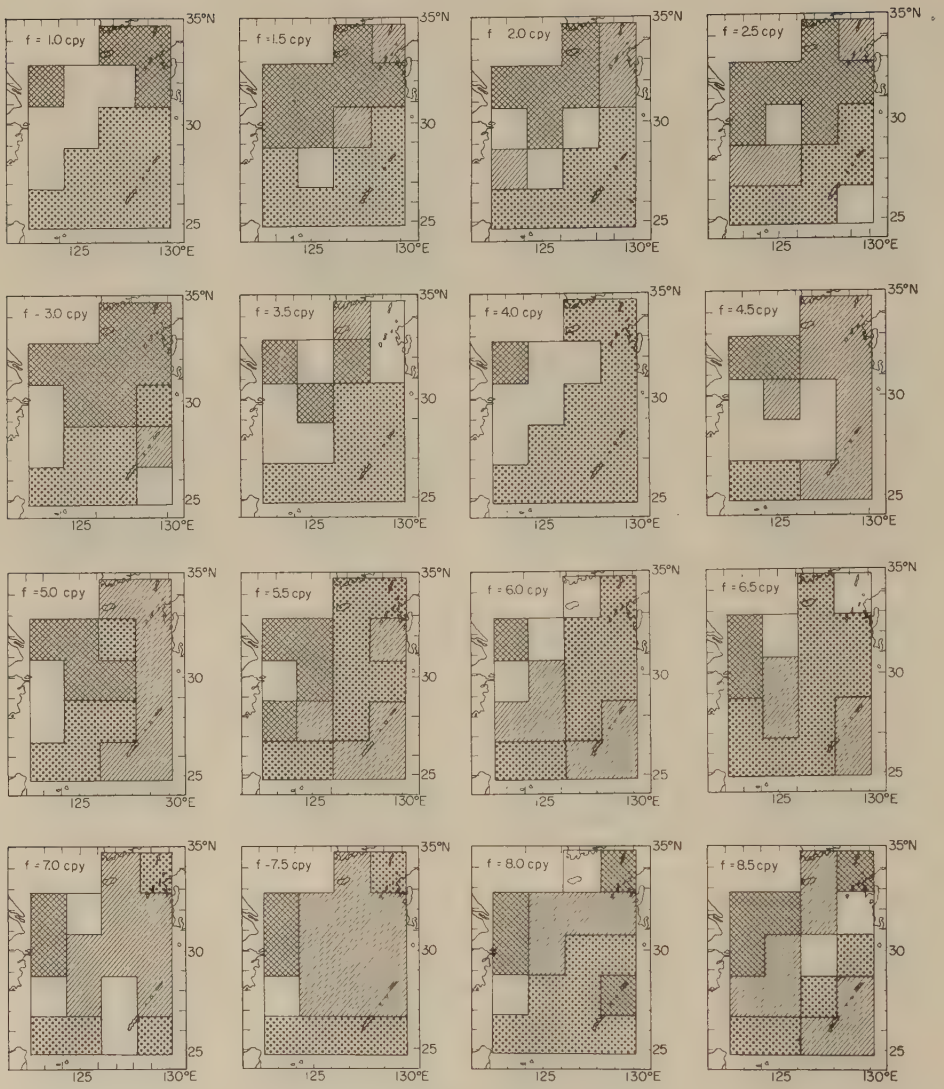

Fig. 12. The distribution of the group.
Group A : dotted
Group B : double-shaded
Group C : blank
Group D : single-shaded

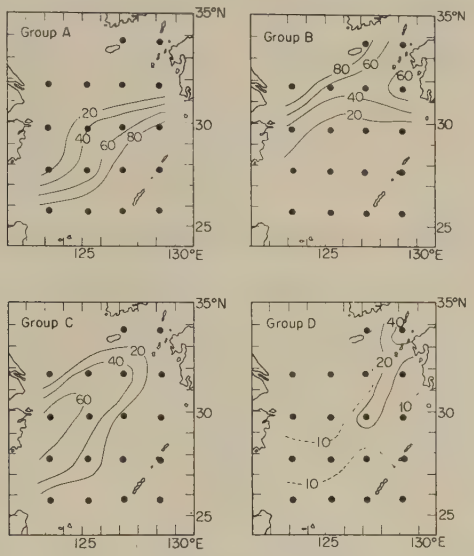

Fig. 13. The index for the group.

other words, the region influenced by the Kuroshio waters is larger than the region influenced by the coastal waters and there is a very small region of correlation with neither the Kuroshio nor the coastal waters in the northeastern part.

The distribution of the Kuroshio and the coastal waters has been determined by using various elements. The results are similar to the deduction shown above. Though this is natural, it is interesting that statistical features of the sea surface temperature are good indexes of both waters.

6. *Concluding remarks*

The spectral analysis of the anomaly of the sea surface temperature shows some characteristic features of the Kuroshio and of the coastal waters and their horizontal distribution. The extent of those waters is in good agreement with the results which have been derived by using other elements. The effect of the scale will be discussed in the following report.

Acknowledgement: The author wishes to express his gratitude to Dr. M. Miyazaki of Japan Meteorological Agency and to Dr. T. Teramoto and Dr. A. Maeda of Ocean Research Institute, University of Tokyo for their advices and to the

staffs of Oceanographical Laboratory of Meteorological Research Institute for discussions.

References

BENDAT, J. S. and A. G. PIERSOL (1966) : Measurement and analysis of random data. John Wiley and Sons, Inc.

BLACKMAN, R. B. and J. W. TUKEY (1958) : The measurement of power spectra. Dover Publ.

KIKUCHI, S. (1959) : Researches on the sea surface temperature of the East China Sea (1st report). *J. Met. Res.*, **11** (3), 169–183 (in Japanese).

KOIZUMI M. (1962) : Seasonal variation of surface temperature of the East China Sea. *J. Oceanogr. Soc. Japan*, 20th Anniversary Volume, 321–329.

KOIZUMI M. (1964) : On the standard deviation of the surface temperature of the East China Sea. *Studies on Oceanography*, 140–144 (in Japanese).

Nagasaki Marine Observatory (1964) : The 10-day mean sea surface temperature of the East China Sea and the Yellow Sea, 1953–1962. *Technical Report of J. M. A.*, No. **31** (in Japanese).

ROBINSON, M. K. (1967) : Comparison of M. Koizumi and M. K. Robinson computations of seasonal variation of mean sea surface temperatures in the East China Sea. *J. Oceanogr. Soc. Japan*, **23** (1), 29–38.

RODEN, G. I. (1962) : On sea-surface temperature, cloudiness and wind variations in the tropical Atlantic. *J. Atmos. Sci.*, **19** (1), 66–80.

The Oceanographical Magazine
Vol. 19, No. 2, December 1967

Geomagnetic Studies of the Japan Sea (1)
—Anomaly Pattern in the Japan Sea—

By

Masashi YASUI, Yuichi HASHIMOTO

Maizuru Marine Observatory

and

Seiya UYEDA

University of Tokyo

(Received December 25, 1967)

Abstract: Since 1964, a proton magnetometer has been towed behind R/V Seifu Maru in the Japan Sea. A total force isodynamic chart and an anomaly chart are presented. Elongated anomalies run along the directions of the longitudinal axis of the sea. The elongation is more clear in the northern half where the bottom is smooth than in the southwestern half where the topography is complicated.

1. Introduction

Measurements of the total force of the earth's magnetic field for studying geological details at sea have been intensively made after the World War II. Scripps Institution of Oceanography has made the epoch making detailed surveys in the seas west of the U. S. coast in co-operation with the U. S.-Coast and Geodetic Survey since 1955. MASON (1958) first reported the existence of the linear geomagnetic trends over the ocean. After that, many authors (e. g. VAQUIER *et al.*, 1961, VINE *et al.*, 1963 and PETER, 1966) have successively presented important papers about the features and possible origin of the anomaly patterns in the Northeast Pacific. In the Atlantic, magnetic surveys have been made mainly by the Lamont Geological Observatory (e. g. DRAKE *et al.*, 1963) and the British group (e.g. BULLARD *et al.*, 1962 and JONES *et al.*, 1966).

Since 1961, measurements in the seas east of Japan have been made mainly as a part of JEDS (Japanese Expedition of Deep Sea) Programme. Summarizing

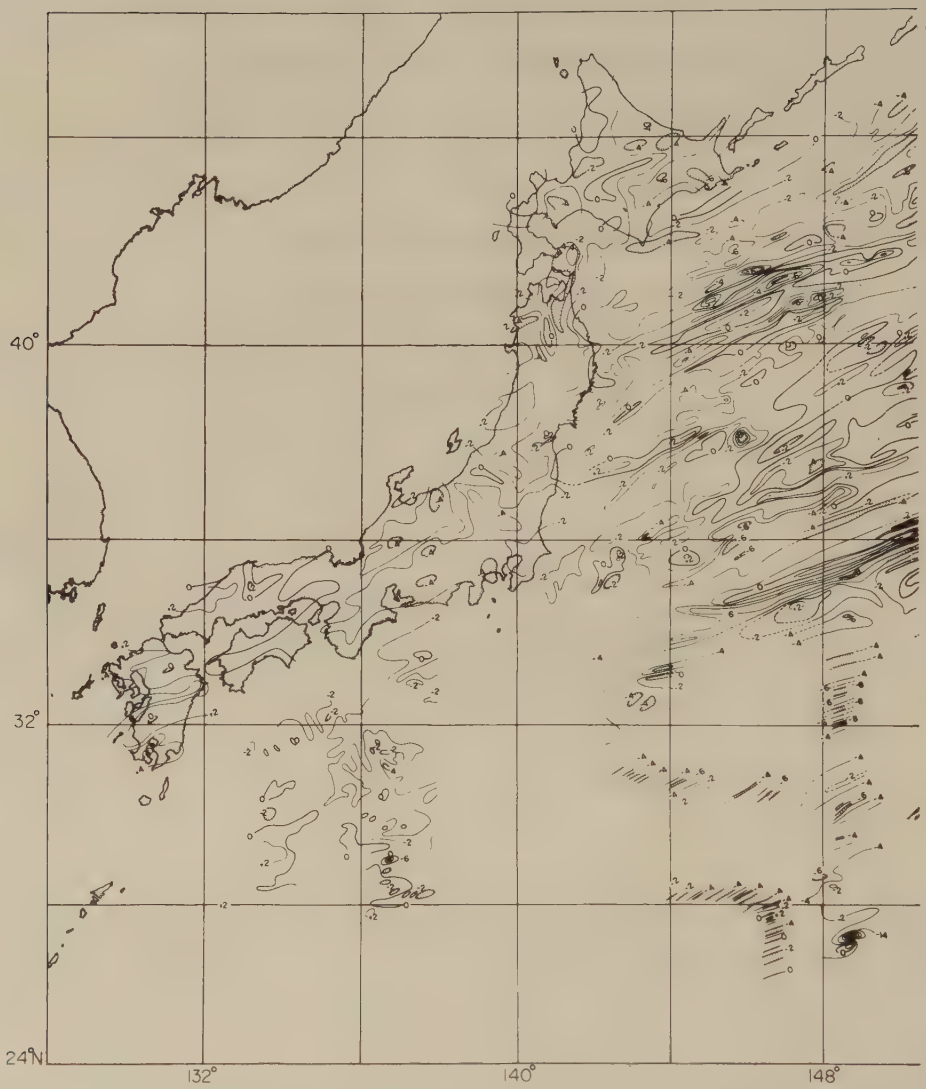

Fig. 1. Total magnetic force anomaly chart in the seas east of Japan (after UYEDA *et al.*, 1967).

the measurements, UYEDA *et al.* (1964 & 1967) reported that anomalous lineations in the geomagnetic field were also found in the seas east of Japan, though they were not as clear as those in the seas west of the U. S.-west coast. The anomaly trends run in the Northeast to Southwest direction almost parallel with the Kuril Islands and Trench and vanish offshore of the east coast of Honshu (Japan Main

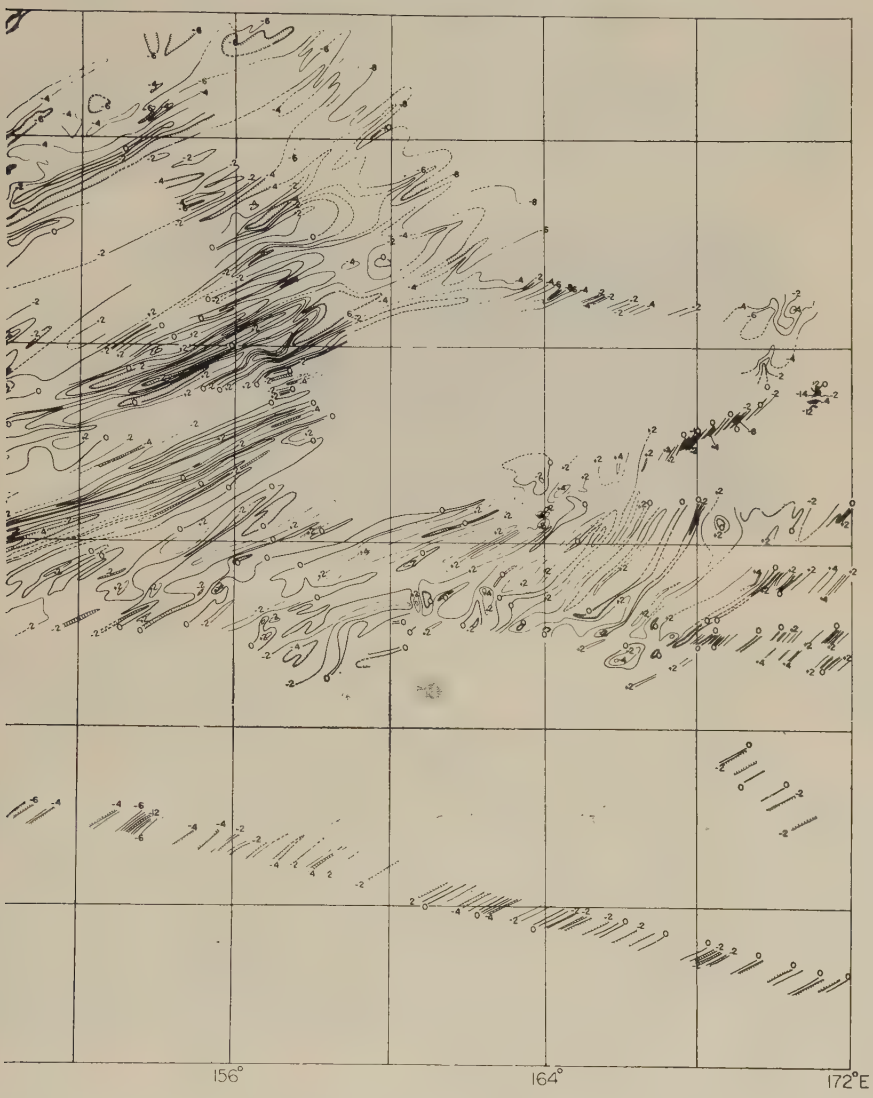

Island) as shown in Fig. 1 (UYEDA *et al.*, 1967). This results presented us the next problem of finding whether or not the linear trends exist in the marginal seas inside the island arcs. This paper aims to present the results of geomagnetic survey made aboard R/V Seifu Maru, Maizuru Marine Observatory, in 1964 through 1967 in the Japan Sea.

2. *Measurements*

The instrument equipped aboard R/V Seifu Maru is the same with what was described by UYEDA *et al.* (1964). A simplified block diagram of the magnetometer is shown in Fig. 2. The coils in the fish are connected to the tuned

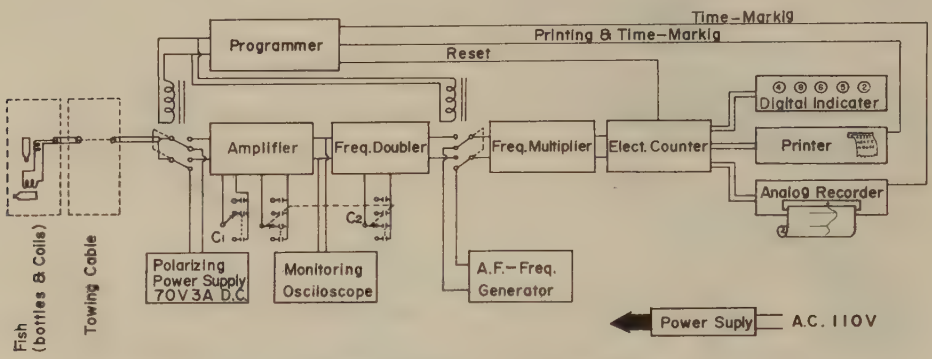

Fig. 2. Block diagram of the magnetometer.

amplifier immediately after having been polarized for 6 seconds with 70 volts 3 amperes D. C. The condensers C_1 and C_2 in the amplifiers are tuned for the maximum amplitude signal on an oscilloscope. Then the signal is doubled in frequency with a fullwave rectifier. The doubled frequency is multiplied by ten with an automatic frequency multiplier after being amplified again by a tuned amplifier. This frequency is counted by a counter, time base of which is chosen so as to make one count one or ten gammas depending on whether the automatic frequency multiplier is used or not. Thus, the time base is a little more than 1.17..... sec. The counting is started after the switching transient has disappeared (about 0.35 sec after shutting off the polarizing power). The automatic frequency multiplier is fed with signal from an oscillator, while the precession signal from the head coils are not counted.

The numbers stored in the counter, which correspond to the geomagnetic total force in unit of a gamma or 10 gammas are digitally displayed with nixi-tubes and printed by a printer. Reading of the last two decades of the measured force in 10 gammas unit is recorded on a strip chart recorder.

The measurement is repeated with interval of 12 sec or 1 minute, which is selected according to the conditions of the change in the field. The time mark is put on the chart of the printer and recorder every 10 minutes.

The fish consists of a paper-base bakelite cylinder housing 2 coils, axes of which are perpendicular to each other and to the towing cable (Fig. 3). The coil consists of a copper wire of 1.5 mm diameter wounded 857 turns around a plastic bottle which serves as a container for about 350 cc of distilled water. The resistance of each coil is about 2.8 ohms.

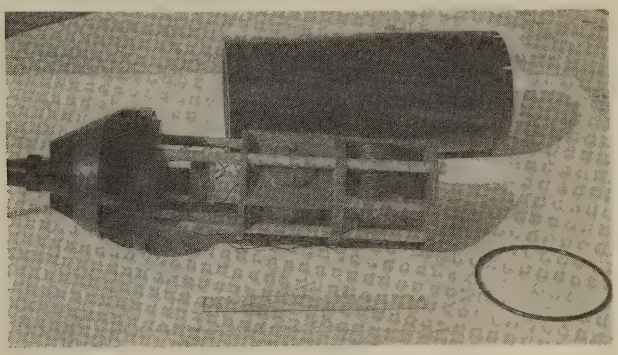

Fig. 3. Fish and coil assembly.

The disturbance of the geomagnetic field astern a steel ship was studied by BULLARD & MASON (1961). The total field at a distance x aft of a ship is approximately expressed as follows:

$$F_x = F + C_0 + C_1 \cos\theta + C_2 \cos 2\theta + C_3 \sin\theta + C_4 \sin 2\theta ,$$

where F ; magnitude of the applied field,

θ ; magnetic heading of a ship measured from North through East,

C_0, C_1, $\cdots C_4$; constants regarding to the distance from the ship.

In the case of R/V Seifu Maru, these relationships are summarized in Fig. 4. In the Figure, the distance astern the ship is given by the ratio to the length of the ship. Further, the constants C_0, C_1, $\cdots C_4$ are proportional to a function ϕ defined as the following, provided the magnetization of the ship can be represented by a pair of poles in the mid plane of the ship;

$$\phi = \frac{2r+1}{(r+\alpha)^2(r+1-\alpha)^2}$$

where r ; ratio of the distance astern to the over-all length of the ship,

α; constant describing the position of the dipole within the ship.

The linearity between the constants C_0, C_1, $\cdots C_4$ and ϕ seems to be the best, when α is chosen as 0.08 for R/V Seifu Maru. The relationships between them are summarized in Fig. 5. Thus, the disturbance at the distance of 150 m (three times the ship's length) astern R/V Seifu Maru is between 5.0 and -5.4 gammas

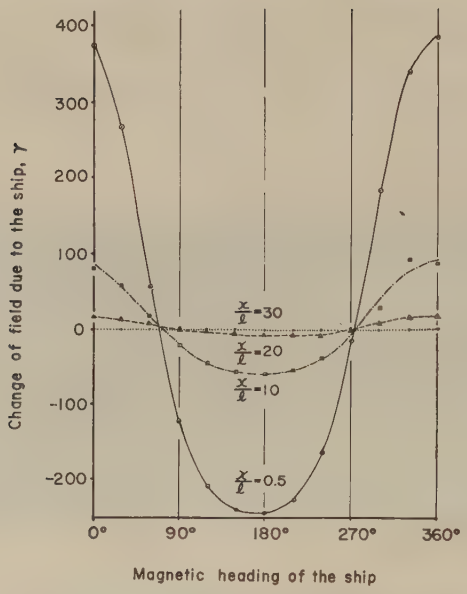

Fig. 4. Disturbance of the field by the ship as a function of course and distance astern.

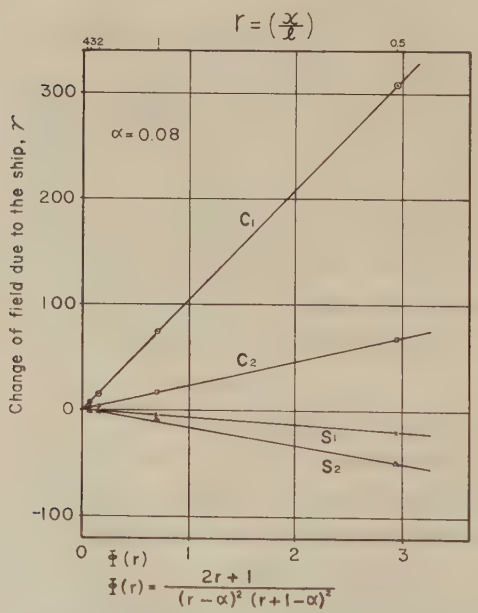

Fig. 5. Theoretical variation of disturbance of the field with distance astern.

Fig. 6. Total force isodynamic chart in the Japan Sea (in gamma).

46°N
138°E
136°E
44°N
52000
51500
142°E
51000
142°E
44°N
50000
140°E
49500
42°N
49000
48500
40°N
47500
38°N

which is almost negligible in the usual marine magnetic survey. In order to make the disturbance less than 1 gamma fishes should be towed at the distance of more than four times ship's length.

3. Results

Since July, 1964, the proton magnetometer has been in operation in almost all of the cruises of R/V Seifu Maru in the Japan Sea. The measurements have been made during the hydrographical surveys. Therefore, the distribution of measurements is not systematic. That is, ship's tracks are most densely spaced in the middle part of the sea, because the declared hydrographical lines for CSK Programme (Cooperative Studies of the Kuroshio and Adjacent Seas Programme) were situated there.

The ship's position was usually fixed at least once in an hour by Loran which was sometimes unreliable especially in the northern part of the sea. The celestial fix and radar fix on islands and coasts are also utilized for establishing tracks.

The total force of the geomagnetic field is tabulated every ten minutes together with the depth, ship's position, speed, course and so on. The values are plotted along the established track. Values of every remarkable maximum and minimum are also indicated.

The resuts are summarized in Fig. 6 as a total force isodynamic chart. In compiling the measured data, no temporal variation was taken into account. However, fairly good agreement within few tens of a gamma was recognized between values in different times, sometimes more than 2 years apart, at cross points. The total force distribution in the sea trends mainly in the northeast to southwest direction. The character is almost the same as those in the seas east of Honshu and in the Okhotsk Sea (Uyeda *et. al.*, 1964 & 1967; Yasui *et. al.*, 1967). However, the distribution is not smooth, especially in the middle part where the topographic configuration is complex as shown in Fig. 7 (Zenkevitch, 1961). But, any clear correspondence between features in anomaly and topography have not been observed.

To delineate the anomaly field in the sea, the general or regional trend has to be subtracted from the observed distribution. In the present work, U. S.-Hydrographic Office Chart No. 1703 for the epoch 1965 is adopted as the general trend. In the procedure, anomalies along the ship's tracks are calculated by subtracting the chart value from values observed every ten minutes. Then 200

Fig. 7. Bathymetric chart of the Japan Sea (after ZENKEVITCH, 1961).

Fig. 8. Total magnetic anomaly chart (contoured every 100 gammas).

48°N
140°E
46°N
138°E
44°N
136°E
134°E
48°N
142°E
142°E
44°N
140°E
42°N
40°N
+200
+100
0
-100
-200
-300
-400
-500

gammas are added to every anomaly value to make them even around zero in the entire Japan Sea. The anomaly contours thus obtained are shown in Fig. 8. In the Figure, a geomagnetic depression is prominent in the northern part, while in the southwestern part the field is slightly high as a whole. As series down to term and order 12 were taken into account in the spherical harmonic analysis of contouring the Chart No. 1703, the chart seems to be inadequate to serve as the regional field for the entire Japan Sea. This tendency was more obvious in the more northern seas such as the Okhotsk Sea where more than 500 gammas is necessary to let anomalies be even around zero (YASUI *et al.*, *loc cit*). It means that the regional trend should be established selfconsistently from the observed data as proposed by BULLARD *et al.* (1962). Such works shall be left for the future study.

4. Discussion

The Japan Sea is roughly separated into two parts according to the topographic features; that is, the northern half with fairly smooth bottoms and the southwestern half with a complicated topography (Fig. 7). This topographic contrast is reflected in the magnetic anomaly. In the smooth-bottom region, regional directional trend in the elongations of the anomalies is prominent. In the southwestern part the trend is shorter in the areal continuation than that in the northern part, though no direct correspondence between magnetic anomalies and topographic features is obvious. Elongation of the anomaly trends enclosed by contoured lines might be much longer in the northern part, if the regional gradient were perfectly eliminated.

In the southwestern part the elongated anomalies are arranged almost in the northeast to southwest direction, whereas in the northern part they are roughly parallel to the meridian. It should be noted that the direction of the anomaly trends in the northernmost area (north of about 43°N) is obviously not the same as those of the anomaly trends in the Okhotsk Sea (YASUI *et al.*, *loc cit*) and in the seas east of Honshu (UYEDA *et al.*, *loc cit*), while fairly good coincidence of the direction can be recognized among anomaly trends in the other part of the Japan Sea, the Okhotsk Sea and the seas east of Honshu.

It seems that directional trend in the Japan Sea was arched together with the Japan Archipelago by tectonic deformation. And it also seems that the directional anomaly trend was broken into fragmental anomalies in the western part by the tectonic deformation. On the other hand, it seems to be reasonable

to consider that the anomaly pattern is separated into two parts at the discontinuity located roughly at 42°N through 43°N. In this case, it might be further considered that the origin of anomaly trends in the northernmost part of the Japan Sea (Tatal Plateau) would be different from those in the other part of the Sea and those in the adjacent seas.

Acknowledgement: The authors wish to express their hearty thanks to Prof. T. RIKITAKE, University of Tokyo, for his constant interest and encouragement. They are also grateful to the staff of the Oceanographical Section, Maizuru Marine Observatory, and Captain H. YASUDA and the crew of R/V Seifu Maru for their kind assistance aboard the ship. This work was partially supported by the grant from the Japan Society for Promotion of Science as a part of the U. S.-Japan Cooperative Science Program,and also partially supported by the grant from the Ministry of Education as a part of the programme of geological and geophysical studies of the Japan Sea.

References

BULLARD, E. C. & R. G. MASON (1961): The magnetic field astern of a ship. *Deep-Sea Res.*, **8**, 20–27.

BULLARD, E. C., M. N. HILL & R. G. MASON (1962): Chart of the total force of the earth's magnetic field for the North-Eastern Atlantic Ocean. *Geomagnetica*, 185–191, Servico Meteorol. National., Lisbon.

DRAKE, C. L., J. HEIRTZLER & J. HIRSHMAN (1963): Magnetic anomalies off Eastern North America. *Jour. Geophys. Res.*, **68**, 5259–5275.

JONES, E. J. W., A. S. LAUGHTON, M. N. HILL & D. DAVIES (1966): A geophysical study of part of the western boundary of the Madeira-Cape Verde abyssal plain. *Deep-Sea Res.*, **13**, 889–907.

MASON, R. G. (1958): A magnetic survey off the west coast of the United States between Latitudes 32° and 36°N, Longitudes 121° and 128°W. *Geophys. Jour. Roy. Ast. Soc.* **1**, 320–329.

PETER, G. (1966): Magnetic anomalies and fracture pattern in the northern Pacific Ocean. *Jour. Geophys. Res.*, **71**, 5365–5374.

UYEDA, S., T. SATO, M. YASUI, T. WATANABE, K. KAWADA & Y. HAGIWARA (1964): Report on geomagnetic survey in the northwestern Pacific during JEDS–VI, JEDS–VII and JEDS–VIII cruises. *Bull. Earthquake Res. Inst.*, **44**, 179–213.

UYEDA, S., Y. TOMODA, T. YABU and S. UTASHIRO (1964): Improvement of sea going proton magnetometer, *Bull. Earthquake Res. Inst.*, **42**, 383–395.

UYEDA, S., V. VACQUIER, M. YASUI, J. SCLATER, T. SATO, J. LAWSON, T. WATANABE, E. SILVER, Y. FUKAO, K. SUDO & M. NISHIKAWA (1967): Results of geomagnetic survey during the cruise of R/V Argo in the western Pacific 1966 and the compilation of magnetic charts of the same area. *Bull. Earthquake Res. Inst.*, **45** (3), 799–814.

VACQUIER, V., A. D. RAFF & R. E. WARREN (1961): Horizontal displacement in the ocean

floor of the northeastern Pacific Ocean. *Geol. Soc. Amer., Bull.*, **72**, 1251–1258.

VINE, F. J. & D. H. MATHEWS (1963): Magnetic anomalies over oceanic ridges. *Nature*, No. **4897**, 947–949.

YASUI, M., Y. HASHIMOTO & S. UYEDA (1967): Geomagnetic and bathymetric study of the Okhotsk Sea (1), *Oceanogr. Mag.*, **19**, 73–85.

ZENKEVITCH, N. L. (1961): Relief of the Japan Sea. *Basic characteristics of geology and oceanography of the Japan Sea*, 5–22, Acad. Sci., U. S. S. R.

気象庁

欧文海洋報告

第 19 巻

THE OCEANOGRAPHICAL MAGAZINE

Vol. 19

Published by the Japan Meteorological Agency

1967

CONTENTS

J. Masuzawa: Ryofu-Maru's survey for CSK in January to March 1967 1
M. Miyazaki: A method of Fourier analysis of tides based on the hourly data of 355 days 7
M. Miyazaki, S. Kuronuma and I. Inoue: Tidal constants along the coast of Japan 13

Report of the Hecateus Expedition-I in the Okhotsk Sea, 1966

1. S. Aoki: Preface 57
2. T. Yasuoka: Hydrography in the Okhotsk Sea-(1) 61
3. M. Yasui, Y. Hashimoto and S. Uyeda: Geomagnetic and bathymetric study of the Okhotsk Sea-(1) 73
4. M. Yasui, T. Kishii and K. Sudo: Terrestrial heat flow in the Okhotsk Sea-(1) 87

J. Masuzawa: An oceanographic section from Japan to New Guinea at 137°E in January 1967 95
T. Ueno: Numerical experiments of the wind-driven circulation in the Pacific Ocean 119
H. Akamatsu and T. Sawara: Cruise report of CSK survey by JMA in 1966 156
M. Miyazaki, S. Kuronuma, T. Inoue and K. Madokoro: Tidal constants along the coast of Japan (Part II) 163
H. Yoshimura: The gross β-radioactivity of fallout collected at the southern weather station located in 29°N and 135°E 169
K. Hishida: The Ito marine observation tower 173
M. Yasui, T. Yasuoka, K. Tanioka and O. Shiota: Oceanographic studies of the Japan Sea(1)—Water characteristics 177
M. Yasui and T. Kishii: Lowering of heat flow probes in the horizontal attitude 193
K. Nagasaka: Handy charger for oceanographic instrument 197
S. Moriyasu: On the anomaly of the sea surface temperature in the East China Sea(I) 201
M. Yasui, Y. Hashimoto and S. Uyeda: Geomagnetic studies of the Japan Sea(1)-Anomaly pattern of the Japan Sea 221

昭和43年3月25日印刷
昭和43年3月30日発行

編集兼発行人　気象庁
東京都千代田区大手町一ノ七

印刷者　花崎実
東京都中央区月島4丁目6-3号

印刷者　大東印刷工芸株式会社
東京都中央区月島4丁目6-3号